CrossMark

Efficiently Searching for Close-in Companions Around Young M Dwarfs Using a Multiyear PSF Library

Aniket Sanghi[1,9] , Jerry W. Xuan[1] , Jason J. Wang[1,2] , Dimitri Mawet[1] , Brendan P. Bowler[3] , Henry Ngo[4] , Marta L. Bryan[5] , Garreth Ruane[6] , Olivier Absil[7] , and Elsa Huby[8]

[1] Cahill Center for Astronomy and Astrophysics, California Institute of Technology, 1200 E. California Boulevard, MC 249-17, Pasadena, CA 91125, USA; asanghi@caltech.edu

[2] Center for Interdisciplinary Exploration and Research in Astrophysics (CIERA) and Department of Physics and Astronomy, Northwestern University, Evanston, IL 60208, USA

[3] The University of Texas at Austin, Department of Astronomy, 2515 Speedway, C1400, Austin, TX 78712, USA

[4] NRC Herzberg Astronomy and Astrophysics, 5071 W Saanich Road, Victoria, BC V9E 2E7, Canada

[5] David A. Dunlap Institute Department of Astronomy & Astrophysics, University of Toronto, 50 St George Street, Toronto, ON M5S 3H4, Canada

[6] Jet Propulsion Laboratory, California Institute of Technology, 4800 Oak Grove Drive, Pasadena, CA 91109, USA

[7] Université de Liège, STAR Institute, Allée du Six Août 19c, B-4000 Liège, Belgium

[8] LESIA, Observatoire de Paris, Université PSL, CNRS, Sorbonne Université, Université Paris Cité, 5 place Jules Janssen, 92195 Meudon, France

Abstract

We present Super-RDI, a unique framework for the application of reference star differential imaging (RDI) to Keck/NIRC2 high-contrast imaging observations with the vortex coronagraph. Super-RDI combines frame selection and signal-to-noise ratio (S/N) optimization techniques with a large multiyear reference point-spread function (PSF) library to achieve optimal PSF subtraction at small angular separations. We compile an ∼7000 frame reference PSF library based on a set of 288 new Keck/NIRC2 L' sequences of 237 unique targets acquired between 2015 and 2019 as part of two planet-search programs designed for RDI, one focusing on nearby young M dwarfs and the other targeting members of the Taurus star-forming region. For our data set, synthetic companion injection-recovery tests reveal that frame selection with the mean-squared error metric combined with Karhunen–Loève Image-Processing-based PSF subtraction using 1000–3000 frames and $\lesssim$500 principal components yields the highest average S/N for injected synthetic companions. We uniformly reduce targets in the young M-star survey with both Super-RDI and angular differential imaging (ADI). For the typical parallactic angle rotation of our data set (∼10°), Super-RDI performs better than a widely used implementation of ADI-based PSF subtraction at separations $\lesssim 0.''4$ ($\approx 5\ \lambda/D$), gaining an average of 0.25 mag in contrast at $0.''25$ and 0.4 mag in contrast at $0.''15$. This represents a performance improvement in separation space over RDI with single-night reference star observations (∼100 frame PSF libraries) applied to a similar Keck/NIRC2 data set in previous work. We recover two known brown dwarf companions and provide detection limits for 155 targets in the young M-star survey. Our results demonstrate that increasing the PSF library size with careful selection of reference frames can improve the performance of RDI with the Keck/NIRC2 vortex coronagraph in L'.

Materials only available in the online version of record: machine-readable table

1. Introduction

The past two decades have witnessed tremendous evolution in efforts to directly detect and characterize exoplanetary systems. Pioneering work has paired instruments such as high-order adaptive optics (AO) systems and small inner-working angle coronagraphs with innovative observing and post-processing strategies to eliminate contaminating starlight and achieve high-contrast ratios (e.g., O. Guyon et al. 2006; B. R. Oppenheimer & S. Hinkley 2009; A.-M. Lagrange et al. 2010; C. Marois et al. 2010; O. Absil & D. Mawet 2010; D. Mawet et al. 2012; B. Macintosh et al. 2015; B. P. Bowler 2016; T. Currie et al. 2023a). The results revealed a previously unseen population of giant planets ($\gtrsim 1\ M_{\rm Jup}$) at wide orbital separations ($\gtrsim 10$ au). Uncovering giant exoplanets at large separations has challenged theories of planet formation and evolution, leading to the exploration of different mechanisms such as core accretion, dynamical scattering, disk instability, and cloud fragmentation, all of which act over different orbital distance regimes (e.g., A. P. Boss 1997; C. Helling et al. 2014; G. Chabrier et al. 2014; R. Helled et al. 2014; K. Kratter & G. Lodato 2016). A primary challenge in investigating these has been the modest sample of directly imaged planets available for precise characterization studies.

Large demographic surveys such as the Gemini Deep Planet Survey (D. Lafrenière et al. 2007a), Strategic Exploration of Exoplanets and Disks with Subaru (M. Tamura 2009, 2016), the Gemini NICI Planet-finding Campaign (M. C. Liu et al. 2010), the International Deep Planet Search (A. Vigan et al. 2012), Planets Around Low Mass Stars (B. P. Bowler et al. 2015a), LBTI Exozodi Exoplanet Common Hunt (A. J. Skemer et al. 2014; J. M. Stone et al. 2018), the Gemini Planet Imager

Exoplanet Survey (B. Macintosh et al. 2018), and the SPHERE Infrared Exoplanets Survey (S. Desidera et al. 2021) have established the rarity of giant planets at wide separations, with occurrence rates as low as a few percent (e.g., B. P. Bowler 2016; E. L. Nielsen et al. 2019; A. Vigan et al. 2021). In contrast, radial velocity (RV) surveys uncover a peak in the giant planet occurrence rate distribution at 2–8 au (R. B. Fernandes et al. 2019; B. J. Fulton et al. 2021). Thus, imaging typical giant planets in the 1–10 au range beyond the water ice line but within the region where protoplanetary disk surface densities quickly fall off can eventually provide a large enough sample to carry out population-level orbital and atmospheric characterization studies. This requires sensitivity gains to be made with both instrumentation and post-processing strategies. In particular, in this study we focus on optimizing L' observations with the Keck/NIRC2 vortex coronagraph.

The Keck/NIRC2 vortex coronagraph (D. Mawet et al. 2005; G. Foo et al. 2005) is an instrument mode that enables infrared high-contrast imaging in the L' and M_s bands ($\lambda = 3.4$–$4.8\ \mu m$) at small angular separations from the star (~ 100 mas). For the nearest young stars, this capability provides unique opportunities for the detection of $\lesssim 10$ au self-luminous giant planets when combined with the right observing strategy (e.g., AF Lep b; K. Franson et al. 2023b). Observations with the Keck/NIRC2 vortex coronagraph have primarily employed the angular differential imaging (ADI; M. C. Liu 2004; C. Marois et al. 2006) strategy. Ground-based ADI observations are conducted with the telescope de-rotator turned off (for Cassegrain focus) or with the field rotator set to track the telescope pupil. As the field of view rotates under sidereal motion, astrophysical signals (e.g., companions and disk features) revolve in the image frame while the point-spread function (PSF) of the host star remains stationary on the detector. Subtracting image frames obtained at different parallactic angles (P.A.s) removes the host starlight without significant subtraction of the planet signal. While ADI has proved to be a powerful observational strategy for directly imaging exoplanets, it possesses certain inherent limitations. Most prominently, observations of close-in companions suffer from self-subtraction of the planet signal. This effect can be reduced by observing the target with sufficient P.A. rotation and employing a rotation gap criterion in post-processing (generally excluding reference frames with $\lesssim 1\ \lambda/D$ field rotation in relation to a given science frame). Such observations are difficult to schedule for a large survey and offer limited sky coverage (see Figure 1 in G. Ruane et al. 2019).

Reference star differential imaging (RDI; B. A. Smith & R. J. Terrile 1984; A. M. Lagrange et al. 2009; D. Lafreniere et al. 2009) is one of the primary observing strategies that enable direct imaging of point sources and disks at small angular separations without the limitations posed by ADI. This approach uses reference stars distinct from the science target to build a model of the target star's PSF for primary-star subtraction. RDI performs best when the reference frames exhibit minimal deviations from the ideal PSF. Space-based applications of RDI (e.g., G. Schneider et al. 2014; R. Soummer et al. 2014; É. Choquet et al. 2016; J. H. Debes et al. 2019; S. Walker et al. 2021; A. Sanghi et al. 2022; A. L. Carter et al. 2023; A. Z. Greenbaum et al. 2023) benefit from more stable conditions since they are not hindered by turbulence from Earth's atmosphere. For ground-based observations, one way previous work has addressed the issue of varying observing conditions is by imaging designated reference stars directly before and after the science observations to ensure maximum PSF correlation (e.g., G. Ruane et al. 2017). When designated reference stars are unavailable, W. J. Xuan et al. (2018) found that restricting the PSF library to all reference frames imaged on the same night as the science target improved sensitivity to point sources at small angular separations ($\lesssim 0\rlap{.}''25$) with respect to ADI. G. Ruane et al. (2019) improved on this strategy by introducing image similarity metric-based pre-frame selection techniques, which increased detection significance by a factor of ~ 3. Imaging binary stars (T. J. Rodigas et al. 2015; L. A. Pearce et al. 2022) or observing the reference star near simultaneously as the science target (Z. Wahhaj et al. 2021) are alternative ways of improving RDI's performance in ground-based applications. The various approaches have been tested with observations across a range of wavelengths and it may be the case that the optimal strategy is wavelength dependent.

The impact of PSF variations can be mitigated by using a diversity of reference frames to accurately create a model of the target star's PSF. Several studies have used archival PSF observations across multiple nights to compile reference libraries (e.g., K. M. Morzinski et al. 2012; B. L. Gerard & C. Marois 2016; R. Ligi et al. 2018; G. Duchêne et al. 2020). Common selection techniques involve excluding close binaries, matching the spectral filter or observing mode between the science and reference star observations, and choosing reference frames with high correlation coefficients with the science data sets. However, most of these studies implemented these techniques for the analysis of a single science target and did not experiment with changing the size of the reference library or using multiple pre-frame selection techniques (primarily because the science focus was different). Such analyses are now important for the complete characterization of RDI's strengths and weaknesses with ground-based instruments. Recently, C. Xie et al. (2022) used all available archival VLT SPHERE/IRDIS $H23$ data (1000+ targets) observed over a period of 5 yr to compile an $\sim 7 \times 10^4$ frame reference library (after the removal of poor reference stars). They analyzed the average performance of RDI across 32 representative targets in their sample as a function of seeing condition and P.A. rotation. For observations obtained under the median seeing condition of their reference library, P.A. rotations of $\approx 30°$, and frame selection with the mean-squared error (MSE) metric, they found that RDI outperformed ADI at separations $\lesssim 0\rlap{.}''4$. For worse seeing conditions or larger P.A. rotations, ADI performed at a level comparable to or better than RDI. C. Xie et al. (2022) experimented with different reference library sizes (up to 10^4 frames) and found that increasing the reference library size to 3000–5000 frames improved RDI's sensitivity level, after which it plateaued. These results motivate investigations into the performance of RDI using large reference libraries with more ground-based high-contrast imaging instruments. Specifically, Keck/NIRC2 vortex coronagraphic observations are well suited to such a study given the large number of observations available in the archive.[10]

In this work, we present the Super-RDI framework, which is designed to improve the performance of the RDI strategy when working with large reference libraries. We develop and apply this framework in the context of Keck/NIRC2 high-contrast L' imaging observations with the vortex coronagraph obtained as

---

[10] https://koa.ipac.caltech.edu

part of two high-contrast imaging surveys, the young M-star survey—which focused on young nearby M dwarfs—and the Taurus survey—which targeted predominantly low-mass members of the Taurus star-forming region.[11] Note that the Taurus survey targets only contribute to our reference library for PSF subtraction of the young M-star survey targets. PSF subtraction results of the Taurus survey targets will be presented in M. L. Bryan et al. (2024, in preparation). This paper is organized as follows. Section 2 describes the design of the young M-star survey from the perspective of target selection and observing strategy. Section 3 details our observations and summarizes the properties of the sample used in our analysis. Section 4 introduces the Super-RDI framework and the steps involved in its implementation. Section 5 outlines the ADI reduction of targets in the young M-star survey sample. Section 6 discusses the sensitivity achieved by Super-RDI and compares its performance to a widely used implementation of ADI-based PSF subtraction in the context of the young M-star survey sample. Section 7 describes point-source detections in the Super-RDI processed data set. Finally, we summarize our conclusions in Section 8. Appendix A provides information about the outcomes of parameter optimization with ADI for our survey data set. Appendix B provides optimal contrasts at select separations for targets in the young M-star survey.

2. Young M-star Survey Design

2.1. Target Selection

Targets in this survey comprise young- and intermediate-age ($\approx$20–200 Myr) nearby M dwarfs within $\approx$100 pc. Precise age-dating of active M dwarfs that are not members of well-recognized young moving groups or star-forming regions can be challenging, so we defer a detailed discussion of ages to a future study. Instead, except for systems with confirmed or candidate companions, the focus of this work is on the RDI processing of these observations and the generation of contrast curves rather than the corresponding mass limits (which require host star ages). Below, we discuss details of the sample selection.

The goal of the young M-star survey was to directly build upon the first generation of direct imaging surveys that probed the outskirts (10–100 au) of young M dwarf systems. In particular, the Planets Around Low-Mass Stars (PALMS) survey carried out deep observations of 122 young M dwarfs with Keck/NIRC2 and Subaru/HiCIAO in the H and K_s bands (B. P. Bowler et al. 2015a). Several widely separated brown dwarf companions were discovered; however, observations from this program made use of Lyot coronagraphs so sensitivity was greatly diminished at closer inner-working angles. Other first-generation high-contrast imaging surveys focusing on young M dwarfs were typically smaller in size (e.g., S. Daemgen et al. 2007; P. Delorme et al. 2012; J. Lannier et al. 2016) or were sensitive to substellar companions at even wider separations (e.g., P. R. Allen & I. N. Reid 2008; M.-E. Naud et al. 2017).

An expanded phase of the PALMS survey was carried out with shorter integration times of a few minutes per target to efficiently search for substellar companions around several hundred newly identified young M dwarfs (B. P. Bowler et al. 2024, in preparation). These targets were selected in the pre-Gaia era

and represent a compilation of new confirmed and candidate low-mass members of young moving groups drawn from a wide range of sources, including published studies—in particular C. A. O. Torres et al. (2008), J. E. Schlieder et al. (2012), E. L. Shkolnik et al. (2012), L. Malo et al. (2013, 2014), A. L. Kraus et al. (2014), J. Gagné et al. (2015), P. Elliott et al. (2016)—and a large ongoing search for new young K- and M-type members of moving groups, some of which are presented in B. P. Bowler et al. (2019). As part of this effort, the companions 2MASS J01225093-2439505 B (B. P. Bowler et al. 2013), 2MASS J02155892-0929121 C (B. P. Bowler et al. 2015b), and 2MASS J22362452+4751425 b (B. P. Bowler et al. 2017) were discovered, which span the brown dwarf to high-mass planetary regimes. Many close binaries with separations ranging from the Keck diffraction limit (about 50 mas in the K band) to several arcseconds were also found in this expanded PALMS AO imaging survey. Among the apparently single stars, those that were the closest, youngest, and most securely linked to known young moving groups were selected for deeper imaging to probe smaller separations at the L' band with the newly installed NIRC2 vortex coronagraph. These are the observations we present in this study.

2.2. Observing Strategy

To efficiently survey a sample of $\approx$150–200 science targets in a time-effective manner, several important factors had to be considered when selecting an optimal observing strategy. The two primary strategies available to the survey were ADI and RDI. For ADI, P.A. rotation accumulated across an observation sequence is the key driver of achievable contrast. For RDI, the similarity between the reference and science frames across variable observing conditions is the primary factor that determines achievable contrast. For this particular survey, we noted the following:

1. Since one of the science goals of the survey was to better understand the demographics of giant planets and brown dwarfs around M dwarfs, an observational setup that remained approximately consistent between targets was preferred.
2. A significant number of targets in our sample overlapped in R.A. (Figure 1), implying that for a fixed number of observing nights, not all targets could be observed at the time of transit (when the P.A. rotation is maximum).
3. To accrue sufficient P.A. rotation (generally $\gtrsim$30°) for ADI, targets would have to be observed for $\sim$1–2 hr (e.g., G. Ruane et al. 2017). Assuming 1 hr (resp. 2 hr) observing blocks, the cost for $\sim$200 targets, including overheads, amounts to an $\sim$200 (resp. $\sim$ 400) hr spread over more than 100 individual nights, if all targets are to be observed during transit (Figure 1).

Thus, to balance efficiency and performance, we chose to primarily design the survey to leverage RDI. Since the targets in the survey are similar in spectral type, science targets observed on the same night could serve as reference stars for each other (the approach explored in W. J. Xuan et al. 2018) or the entire set of observations after survey completion could be used as a PSF library for RDI (the approach explored in this work). While we still conducted observations in vertical angle (ADI) mode to ensure PSF consistency, we did not accrue significant P.A. rotation for the majority of targets in our sample (Figure 1) and thus do not expect ADI to perform at a comparable level for our survey.
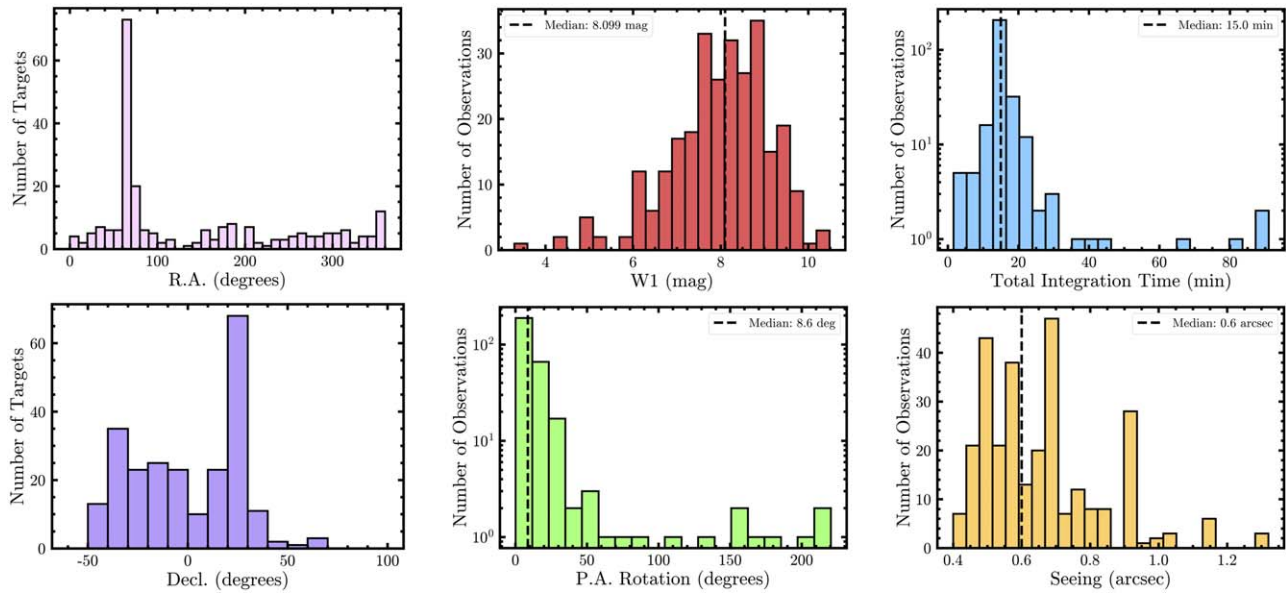

Figure 1. Histograms summarizing distributions for key properties of targets in the sample (R.A. and decl.) and individual observations (*W1* mag, total integration time, P.A. rotation, and seeing). The median values for the observations are as follows: 8.099 mag *W1*, 15 minutes of total integration time, $8°\!.6$ P.A. rotation, and $0''\!.6$ seeing.

3. Observations

This work's sample consists of a set of 288 sequences of 237 unique targets observed from 2015 December 26 to 2019 January 9. The sample is comprised of targets that have been observed independently as part of two survey programs with Keck/NIRC2: the young M-star survey (195 observations of 157 unique targets) and the Taurus survey (93 observations of 80 unique targets). Both sets of observations were taken with the vector vortex coronagraph, installed in the Keck/NIRC2 camera (E. Serabyn et al. 2017), using the QACITS automatic, real-time coronagraphic PSF centering algorithm (E. Huby et al. 2015, 2017). Typically, the centering accuracy provided by QACITS is 2.4 mas rms (E. Huby et al. 2017), or 0.025 λ/D rms in the L' band. In comparison, the pixel scale of the NIRC2 vortex coronagraph is 9.971 mas per pixel (M. Service et al. 2016). The full data set contains images taken in the L' (central wavelength of 3.776 μm) bandpass. For our sample, the median and mean on-source integration times (number of science frames × coadds × exposure time per coadd) are 15.0 minutes and 16.5 minutes, respectively. The median and mean seeing conditions were $0''\!.6$ and $0''\!.7$. Seeing is obtained from Maunakea Weather Center's[12] DIMM Seeing Monitor (mean value) or the CFHT WX Tower Seeing Monitors (mean value) if the former is unavailable. Seeing conditions were not available for a total of 27 targets observed across four nights: 2015 December 26, 2015 December 27, 2017 December 24, and 2018 October 21. Important properties of the sample are presented individually for each target in Table 1 and as distributions in Figure 1.

The general observing sequence for targets in our full sample is summarized below. We acquire one image of the star without the coronagraph to characterize the unocculted PSF, two sky frames of a blank field $10''$ away from the target, and then $\approx$18–40 science frames with the star centered on the vortex, representing an individual frame integration time of $\approx$0.5–1.0 s. Longer observations or those undertaken in rapidly

changing conditions require the full sequence to be repeated every 10–30 minutes. This allows for sampling of potential variations in the unocculted PSF and sky background. All observations were taken with the telescope's field rotator set to track the telescope pupil in order to exploit the natural rotation of the sky for ADI. For our data set, the median and mean P.A. rotations are $8°\!.6$ and $16°\!.4$, respectively. The range of P.A. rotations is $0°\!.1$–$220°\!.3$.

The raw data set is uniformly reprocessed using a pipeline that automatically downloads, sorts, and processes data (W. J. Xuan et al. 2018). This pipeline is based on functions available as part of the Vortex Image Processing (VIP) software package (C. A. Gomez Gonzalez et al. 2017; V. Christiaens et al. 2023) as well as custom programs. Here, the key points from W. J. Xuan et al. (2018) are summarized below. (1) The science and sky background frames are flat field corrected using the median of 5–10 blank sky images acquired with the vortex mask removed near the end of the same or a close in time night. (2) The pipeline is used to replace the value of bad, hot, and dead pixels in the science, sky, dark, and flat field frames with the median of the neighboring pixels in a 5×5 pixel box. However, we avoid bad pixel correction in a circular region of diameter equal to the full width at half-maximum (FWHM) centered on the star. (3) A principal component analysis (PCA)-based algorithm subtracts the sky from the science frames (the central 1 FWHM is masked). The sky-subtracted images are registered to the target star's location and derotated to align north up and east left. We provide the preprocessed coronagraphic frames, corresponding P.A.s, and unocculted stellar PSF frame for all targets in the young M-star survey on Zenodo[13] for public access.

4. The Super-RDI Framework

In this section, we develop a multistep framework called Super-RDI for the systematic use of a large PSF library to

---

Table 1
Keck/NIRC2 L' Vortex Coronagraphic Observations

Name	$\alpha_{2000.0}$ (hh:mm:ss.ssss)	$\delta_{2000.0}$ ($\pm$ dd:mm:ss.sss)	UT Date	$N \times$ coadds $\times t_{\exp}$ (s)	ΔP.A. (°)	Seeing (arcsec)	$W1$ (mag)	R (mag)	R References
Young M-star Survey Targets									
2MASS J00243202-2522528	00:24:32.0175	−25:22:52.952	2016-07-18	18 × 45 × 1.0	7.2	0.52 ± 0.13	8.800 ± 0.024	13.221 ± 0.130	(1)
2MASS J00275023-3233060	00:27:50.2331	−32:33:06.306	2016-11-05	20 × 45 × 1.0	7.0	0.82 ± 0.22	7.782 ± 0.028	11.790 ± 0.030	(2)
2MASS J00275023-3233060	00:27:50.2331	−32:33:06.306	2016-09-11	20 × 45 × 1.0	6.9	0.56 ± 0.18	7.782 ± 0.028	11.790 ± 0.030	(2)
GJ 2006B	00:27:50.3535	−32:33:24.130	2016-09-12	14 × 45 × 1.0	4.8	0.65 ± 0.22	7.931 ± 0.025	12.040 ± 0.020	(2)
[SLS2012] PYC J00390+1330	00:39:03.4171	+13:30:16.848	2018-07-30	23 × 45 × 1.0	52.6	0.54 ± 0.21	9.843 ± 0.023	⋯	⋯
2MASS J00551501+3015156	00:55:15.0287	+30:15:15.567	2016-09-23	27 × 45 × 1.0	35.4	0.4	9.105 ± 0.023	12.390	(3)
2MASS J00551501+3015156	00:55:15.0287	+30:15:15.567	2016-09-11	20 × 45 × 1.0	26.1	0.56 ± 0.18	9.105 ± 0.023	12.390	(3)
2MASS J01123504+1703557	01:12:35.0523	+17:03:55.571	2016-10-17	20 × 45 × 1.0	24.6	0.93 ± 0.24	9.256 ± 0.022	13.780 ± 0.090	(1)
2MASS J01220441-3337036	01:22:04.4344	−33:37:03.584	2015-12-27	26 × 60 × 0.5	10.8	⋯	7.274 ± 0.034	10.147 ± 0.001	(4)
2MASS J01225093-2439505	01:22:50.9356	−24:39:50.690	2016-10-17	20 × 45 × 1.0	7.9	0.93 ± 0.24	9.022 ± 0.023	13.890 ± 0.070	(1)
2MASS J01225093-2439505	01:22:50.9356	−24:39:50.690	2018-07-30	7 × 45 × 1.0	2.5	0.54 ± 0.21	9.022 ± 0.023	13.890 ± 0.070	(1)
2MASS J01351393-0712517	01:35:13.9246	−07:12:51.457	2016-09-12	20 × 45 × 1.0	12.0	0.65 ± 0.22	7.969 ± 0.025	13.053 ± 0.090	(1)
2MASS J01354915-0753470	01:35:49.1731	−07:53:47.318	2017-09-09	20 × 45 × 1.0	11.3	0.47 ± 0.13	9.686 ± 0.023	13.540 ± 0.120	(1)
2MASS J01365516-0647379	01:36:55.1765	−06:47:38.002	2016-11-05	20 × 45 × 1.0	11.7	0.82 ± 0.22	8.703 ± 0.022	13.710 ± 0.090	(1)
2MASS J01365516-0647379	01:36:55.1765	−06:47:38.002	2016-09-11	20 × 45 × 1.0	12.0	0.56 ± 0.18	8.703 ± 0.022	13.710 ± 0.090	(1)
2MASS J02001277-0840516	02:00:12.7785	−08:40:51.914	2015-12-27	27 × 60 × 0.5	20.2	⋯	7.771 ± 0.028	12.026 ± 0.050	(1)
[SLS2012] PYC J02017+0117N	02:01:46.7688	+01:17:16.092	2016-09-12	20 × 45 × 1.0	17.3	0.65 ± 0.22	7.975 ± 0.022	12.750 ± 0.080	(1)
[SLS2012] PYC J02017+0117S	02:01:46.9222	+01:17:05.933	2016-09-23	20 × 45 × 1.0	17.6	0.4	8.141 ± 0.025	12.650 ± 0.060	(1)
[SLS2012] PYC J02017+0117S	02:01:46.9222	+01:17:05.933	2016-09-11	24 × 45 × 1.0	22.3	0.56 ± 0.18	8.141 ± 0.025	12.650 ± 0.060	(1)
2MASS J02070176-4406380	02:07:01.7619	−44:06:37.989	2016-11-05	20 × 45 × 1.0	6.2	0.82 ± 0.22	8.246 ± 0.023	12.980 ± 0.100	(1)
2MASS J02070786-1810077	02:07:07.8751	−18:10:07.832	2017-01-15	21 × 45 × 1.0	10.5	0.65 ± 0.13	9.595 ± 0.023	⋯	⋯
2MASS J02175601+1225266	02:17:56.0207	+12:25:26.421	2016-11-05	20 × 45 × 1.0	31.2	0.82 ± 0.22	8.966 ± 0.023	13.728 ± 0.130	(1)
2MASS J02304623-4343493	02:30:46.2425	−43:43:49.529	2016-09-12	20 × 45 × 1.0	6.2	0.65 ± 0.22	8.186 ± 0.023	11.590 ± 0.030	(1)
2MASS J02505959-3409050	02:50:59.6195	−34:09:05.111	2017-09-09	20 × 45 × 1.0	6.6	0.47 ± 0.13	9.464 ± 0.023	⋯	⋯
2MASS J02590322-4232450	02:59:03.2450	−42:32:44.967	2017-01-15	20 × 45 × 1.0	6.4	0.65 ± 0.13	10.243 ± 0.023	14.950 ± 0.160	(1)
2MASS J03025156-1911496	03:02:51.5636	−19:11:49.697	2016-11-11	20 × 45 × 1.0	8.6	0.59 ± 0.14	9.486 ± 0.023	⋯	⋯
2MASS J03093877-3014352	03:09:38.7832	−30:14:35.138	2015-12-26	30 × 50 × 0.5	8.7	⋯	10.486 ± 0.023	⋯	⋯
HIP 14807	03:11:12.3210	+22:25:22.571	2017-11-06	20 × 45 × 1.0	14.6	0.68 ± 0.15	7.568 ± 0.027	⋯	⋯
HIP 14807	03:11:12.3210	+22:25:22.571	2016-11-11	20 × 45 × 1.0	7.3	0.59 ± 0.14	7.568 ± 0.027	⋯	⋯
HIP 14807	03:11:12.3210	+22:25:22.571	2016-09-11	26 × 45 × 1.0	54.9	0.56 ± 0.18	7.568 ± 0.027	⋯	⋯
2MASS J03190864-3507002	03:19:08.6661	−35:07:00.303	2016-11-23	20 × 60 × 0.8	7.2	0.69 ± 0.14	7.556 ± 0.030	⋯	⋯
2MASS J03214689-0640242	03:21:46.9232	−06:40:24.214	2016-09-12	20 × 45 × 1.0	12.3	0.65 ± 0.22	6.761 ± 0.049	10.981 ± 0.030	(1)
2MASS J03282609-0537361	03:28:26.0984	−05:37:36.331	2017-01-15	20 × 45 × 1.0	12.3	0.65 ± 0.13	9.290 ± 0.022	⋯	⋯
HD 21845B	03:33:14.0499	+46:15:18.978	2015-12-27	30 × 60 × 0.5	16.1	⋯	⋯	10.500	(5)
TYC 1252-798-1	03:46:14.8253	+17:09:10.017	2016-09-12	20 × 45 × 1.0	89.2	0.65 ± 0.22	8.157 ± 0.024	10.877 ± 0.029	(6)
HIP 17695	03:47:23.3412	−01:58:19.947	2017-01-15	20 × 45 × 1.0	13.1	0.65 ± 0.13	6.812 ± 0.062	10.452	(7)
WISE J035223.52-282619.6	03:52:23.4823	−28:26:19.585	2017-09-09	20 × 45 × 1.0	7.1	0.47 ± 0.13	8.882 ± 0.023	⋯	⋯
2MASS J04000395-2902280	04:00:03.9593	−29:02:27.863	2015-12-26	30 × 50 × 0.5	8.9	⋯	7.784 ± 0.025[a]	10.350 ± 0.620	(1)
2MASS J04021648-1521297	04:02:16.4849	−15:21:29.807	2015-12-26	30 × 50 × 0.5	10.9	⋯	7.539 ± 0.028	⋯	⋯
2MASS J04093930-2648489	04:09:39.3066	−26:48:49.090	2017-11-06	20 × 45 × 1.0	7.4	0.68 ± 0.15	8.460 ± 0.023	⋯	⋯
2MASS J04141730-0906544	04:14:17.3079	−09:06:54.605	2017-09-09	6 × 45 × 1.0	4.3	0.47 ± 0.13	8.596 ± 0.023	13.612 ± 0.100	(1)
G7-34	04:17:18.5336	+08:49:22.015	2016-11-11	20 × 45 × 1.0	17.1	0.59 ± 0.14	8.005 ± 0.022	12.500 ± 0.010	(2)
2MASS J04244260-0647313	04:24:42.6192	−06:47:31.373	2016-09-12	20 × 45 × 1.0	14.1	0.65 ± 0.22	8.499 ± 0.024	13.641 ± 0.090	(1)
2MASS J04353618-2527347	04:35:36.1920	−25:27:34.587	2017-11-06	20 × 45 × 1.0	7.4	0.68 ± 0.15	7.256 ± 0.037	12.080 ± 0.030	(1)
2MASS J04353618-2527347	04:35:36.1920	−25:27:34.587	2017-01-15	20 × 45 × 1.0	7.7	0.65 ± 0.13	7.256 ± 0.037	12.080 ± 0.030	(1)
[WKS96] 42	04:37:26.8711	+18:51:26.718	2016-11-11	20 × 45 × 1.0	1.2	0.59 ± 0.14	8.691 ± 0.045	11.580 ± 0.060	(1)

Sanghi et al.

Table 1
(Continued)

Name	$\alpha_{2000.0}$ (hh:mm:ss.ssss)	$\delta_{2000.0}$ ($\pm$ dd:mm:ss.sss)	UT Date	$N \times$ coadds $\times t_{exp}$ (s)	ΔP.A. (°)	Seeing (arcsec)	$W1$ (mag)	R (mag)	R References
2MASS J04435686+3723033	04:43:56.8689	+37:23:03.362	2015-12-26	30 × 50 × 0.5	20.1	⋯	8.675 ± 0.023	12.932 ± 0.090	(1)
2MASS J04522441-1649219	04:52:24.4148	−16:49:21.926	2016-01-25	27 × 60 × 0.5	10.6	0.85	6.776 ± 0.071	11.237 ± 0.020	(1)
V1005 Ori	04:59:34.8342	+01:47:00.669	2016-11-11	20 × 90 × 0.5	10.1	0.59 ± 0.14	6.210 ± 0.095	9.603 ± 0.030	(1)
[SLS2012] PYC J05019+0108	05:01:56.6595	+01:08:42.901	2017-11-06	20 × 45 × 1.0	15.4	0.68 ± 0.15	7.506 ± 0.032	12.564 ± 0.070	(1)
[SLS2012] PYC J05019+0108	05:01:56.6595	+01:08:42.901	2017-01-15	20 × 45 × 1.0	15.5	0.65 ± 0.13	7.506 ± 0.032	12.564 ± 0.070	(1)
2MASS J05195695-1124440	05:19:56.9566	−11:24:44.147	2015-12-26	32 × 35 × 0.75	22.9	⋯	9.394 ± 0.022	13.790 ± 0.090	(1)
2MASS J05234246+0651581	05:23:42.4636	+06:51:58.295	2016-11-11	20 × 45 × 1.0	6.0	0.59 ± 0.14	8.998 ± 0.023	⋯	⋯
2MASS J05241317-2104427	05:24:13.1792	−21:04:42.919	2017-01-15	20 × 45 × 1.0	8.0	0.65 ± 0.13	9.226 ± 0.024	⋯	⋯
WISE J053100.27+231218.3	05:31:00.2794	+23:12:18.338	2016-11-23	20 × 45 × 1.0	1.9	0.69 ± 0.14	9.530 ± 0.023[a]	⋯	⋯
2MASS J05335981-0221325	05:33:59.8219	−02:21:32.384	2016-11-11	20 × 45 × 1.0	5.5	0.59 ± 0.14	7.535 ± 0.031	12.040 ± 0.060	(1)
2MASS J05395494-1307598	05:39:54.9495	−13:07:59.832	2016-11-11	20 × 45 × 1.0	4.7	0.59 ± 0.14	9.613 ± 0.023	⋯	⋯
2MASS J05432676-3025129	05:43:26.7627	−30:25:13.005	2017-11-06	23 × 45 × 1.0	8.0	0.68 ± 0.15	9.462 ± 0.023	⋯	⋯
2MASS J06012186-1937547	06:01:21.8668	−19:37:54.755	2017-11-06	22 × 45 × 1.0	8.5	0.68 ± 0.15	10.297 ± 0.022	⋯	⋯
2MASS J06022455-1634494	06:02:24.5661	−16:34:49.408	2017-11-06	20 × 45 × 1.0	7.0	0.68 ± 0.15	8.099 ± 0.023	11.556 ± 0.030	(1)
2MASS J06022455-1634494	06:02:24.5661	−16:34:49.408	2016-11-11	13 × 45 × 1.0	3.1	0.59 ± 0.14	8.099 ± 0.023	11.556 ± 0.030	(1)
2MASS J06022455-1634494	06:02:24.5661	−16:34:49.408	2017-01-15	20 × 45 × 1.0	8.8	0.65 ± 0.13	8.099 ± 0.023	11.556 ± 0.030	(1)
2MASS J06135773-2723550	06:13:57.7460	−27:23:55.153	2017-01-15	20 × 45 × 1.0	7.0	0.65 ± 0.13	8.878 ± 0.023	⋯	⋯
2MASS J06373215-2823125	06:37:32.1556	−28:23:12.544	2016-01-25	30 × 60 × 0.5	9.6	0.85	8.640 ± 0.023	⋯	⋯
2MASS J06380031-4056011	06:38:00.3126	−40:56:01.050	2015-12-26	11 × 40 × 0.75	2.8	⋯	9.412 ± 0.023	⋯	⋯
2MASS J06511418-4037510	06:51:14.1784	−40:37:50.918	2015-12-27	27 × 60 × 0.5	7.7	⋯	7.211 ± 0.037	⋯	⋯
2MASS J07140101-1945332	07:14:01.0124	−19:45:33.169	2016-03-25	40 × 20 × 1.0	10.8	0.7	9.844 ± 0.023	⋯	⋯
2MASS J07285117-3015527	07:28:51.1711	−30:15:52.826	2016-11-24	15 × 45 × 1.0	7.1	0.60 ± 0.15	7.844 ± 0.025	13.510 ± 0.080	(1)
2MASS J07285117-3015527	07:28:51.1711	−30:15:52.826	2017-11-06	30 × 45 × 1.0	10.6	0.68 ± 0.15	7.844 ± 0.025	13.510 ± 0.080	(1)
2MASS J07310129+4600266	07:31:01.2936	+46:00:26.423	2015-12-26	25 × 40 × 0.75	12.5	⋯	8.978 ± 0.026	13.838 ± 0.080	(1)
2MASS J07504838-2931126	07:50:48.3822	−29:31:12.541	2015-12-26	25 × 40 × 0.75	7.2	⋯	8.815 ± 0.022	⋯	⋯
2MASS J09123564-1517033	09:12:35.6342	−15:17:03.551	2017-01-14	20 × 45 × 1.0	8.0	0.95 ± 0.40	8.142 ± 0.024	11.740 ± 0.070	(1)
2MASS J09123564-1517033	09:12:35.6342	−15:17:03.551	2015-12-26	25 × 40 × 0.75	9.4	⋯	8.142 ± 0.024	11.740 ± 0.070	(1)
2MASS J09353126-2802552	09:35:31.2689	−28:02:55.366	2017-01-14	20 × 45 × 1.0	6.9	0.95 ± 0.40	7.623 ± 0.029	⋯	⋯
2MASS J09353126-2802552	09:35:31.2689	−28:02:55.366	2015-12-26	25 × 40 × 0.75	7.4	⋯	7.623 ± 0.029	⋯	⋯
2MASS J09445422-1220544	09:44:54.1925	−12:20:54.376	2017-01-14	20 × 45 × 1.0	9.7	0.95 ± 0.40	7.359 ± 0.034	13.467 ± 0.100	(1)
2MASS J09445422-1220544	09:44:54.1925	−12:20:54.376	2015-12-27	43 × 60 × 0.5	22.5	⋯	7.359 ± 0.034	13.467 ± 0.100	(1)
2MASS J10120908-3124451	10:12:09.0907	−31:24:45.284	2016-11-23	26 × 90 × 0.5	10.5	0.69 ± 0.14	7.758 ± 0.027	13.070 ± 0.070	(1)
2MASS J10121768-0344441	10:12:17.6682	−03:44:44.392	2017-01-14	20 × 45 × 1.0	12.6	0.95 ± 0.40	4.838 ± 0.226	8.258	(7)
2MASS J10121768-0344441	10:12:17.6682	−03:44:44.392	2016-11-22	20 × 90 × 0.5	7.6	0.5	4.838 ± 0.226	8.258	(7)
2MASS J10182870-3150029	10:18:28.6987	−31:50:02.830	2015-12-26	28 × 40 × 0.75	23.8	⋯	7.824 ± 0.024	11.382 ± 0.220	(1)
2MASS J10252092-4241539	10:25:20.9179	−42:41:53.952	2016-03-25	40 × 20 × 1.0	10.5	0.7	8.502 ± 0.023	12.296 ± 0.040	(1)
2MASS J10260210-4105537	10:26:02.1058	−41:05:53.861	2017-01-14	20 × 45 × 1.0	6.4	0.95 ± 0.40	8.150 ± 0.022	⋯	⋯
2MASS J10260210-4105537	10:26:02.1058	−41:05:53.861	2016-11-22	20 × 60 × 0.8	6.4	0.5	8.150 ± 0.022	⋯	⋯
BD+01 2447	10:28:55.5512	+00:50:27.598	2015-12-27	50 × 60 × 0.5	28.3	⋯	5.180 ± 0.193	8.617 ± 0.003	(8)
2MASS J10423011-3340162	10:42:30.1018	−33:40:16.229	2016-03-25	40 × 20 × 1.0	13.1	0.7	6.793 ± 0.037	⋯	⋯
TWA 1	11:01:51.9053	−34:42:17.033	2016-01-25	30 × 60 × 0.5	8.6	0.85	7.009 ± 0.052	10.626 ± 0.050	(1)
2MASS J11110358-3134591	11:11:03.5752	−31:34:59.148	2017-05-10	20 × 45 × 1.0	7.0	0.4	9.352 ± 0.023	⋯	⋯
2MASS J11200609-1029468	11:20:06.1045	−10:29:46.727	2016-05-27	20 × 45 × 1.0	11.4	0.7	⋯	10.887 ± 0.040	(1)
2MASS J11210549-3845163	11:21:05.4814	−38:45:16.522	2017-01-14	20 × 45 × 1.0	6.4	0.95 ± 0.40	8.052 ± 0.023	12.340 ± 0.110	(1)
TWA 8B	11:32:41.1733	−26:52:09.107	2016-03-25	40 × 20 × 1.0	11.4	0.7	8.928 ± 0.079	13.680 ± 0.020	(2)
TWA 8A	11:32:41.2658	−26:51:55.961	2016-03-25	40 × 20 × 1.0	9.0	0.7	7.275 ± 0.039	11.140 ± 0.040	(2)
TWA 33	11:39:33.8249	−30:40:00.365	2017-01-15	30 × 45 × 1.0	11.1	0.65 ± 0.13	8.817 ± 0.023	14.850 ± 0.120	(1)

Table 1
(Continued)

Name	$\alpha_{2000.0}$ (hh:mm:ss.ssss)	$\delta_{2000.0}$ ($\pm$ dd:mm:ss.sss)	UT Date	$N \times$ coadds $\times t_{exp}$ (s)	ΔP.A. (°)	Seeing (arcsec)	$W1$ (mag)	R (mag)	R References
2MASS J11431742+1123126	11:43:17.4434	+11:23:12.530	2017-05-10	20 × 45 × 1.0	10.1	0.4	9.128 ± 0.024	⋯	⋯
TWA 9A	11:48:24.2227	−37:28:49.114	2017-01-14	20 × 45 × 1.0	6.5	0.95 ± 0.40	7.667 ± 0.036	10.920 ± 0.030	(1)
2MASS J12000160-1731308	12:00:01.5885	−17:31:30.864	2017-01-15	30 × 45 × 1.0	13.2	0.65 ± 0.13	8.376 ± 0.023	13.498 ± 0.080	(1)
2MASS J12120849+1248050	12:12:08.5000	+12:48:04.908	2016-06-09	20 × 45 × 1.0	14.2	0.46 ± 0.15	8.838 ± 0.023	11.916 ± 0.070	(1)
2MASS J12151838-0237283	12:15:18.3908	−02:37:28.259	2016-05-27	20 × 45 × 1.0	14.5	0.7	7.698 ± 0.027	11.142 ± 0.040	(1)
2MASS J12153072-3948426	12:15:30.7203	−39:48:42.606	2016-04-13	30 × 30 × 1.0	7.9	1.00 ± 0.26	7.209 ± 0.035	10.919 ± 0.030	(1)
2MASS J12350424-4136385	12:35:04.2560	−41:36:38.616	2016-04-13	30 × 30 × 1.0	7.8	1.00 ± 0.26	8.095 ± 0.023	⋯	⋯
TWA 11C	12:35:48.9396	−39:50:24.567	2017-01-14	35 × 45 × 1.0	14.7	0.95 ± 0.40	8.807 ± 0.023	14.070 ± 0.030	(1)
TWA 11B	12:36:00.5491	−39:52:15.693	2017-05-11	28 × 45 × 1.0	9.6	0.58 ± 0.15	7.677 ± 0.060	⋯	⋯
2MASS J12374082+3450555	12:37:40.8120	+34:50:55.468	2016-01-25	30 × 60 × 0.5	26.7	0.85	8.419 ± 0.023	11.617 ± 0.030	(1)
2MASS J13213722-4421518	13:21:37.2192	−44:21:51.861	2017-01-14	25 × 45 × 1.0	8.0	0.95 ± 0.40	8.745 ± 0.023	⋯	⋯
2MASS J13283294-3654233	13:28:32.9408	−36:54:23.364	2016-03-25	50 × 20 × 1.0	10.6	0.7	⋯	13.644 ± 0.090	(1)
2MASS J13342523+6956273	13:34:25.2090	+69:56:27.264	2016-01-25	30 × 60 × 0.5	9.1	0.85	8.587 ± 0.023	12.924 ± 0.040	(1)
2MASS J13343188-4209305	13:34:31.8880	−42:09:30.690	2016-06-09	20 × 45 × 1.0	6.2	0.46 ± 0.15	7.938 ± 0.024	10.420 ± 0.020	(1)
2MASS J13382562-2516466	13:38:25.6052	−25:16:46.760	2016-05-27	20 × 45 × 1.0	7.9	0.7	7.647 ± 0.030	12.353 ± 0.060	(1)
2MASS J13412668-4341522	13:41:26.6777	−43:41:52.350	2017-05-10	20 × 45 × 1.0	6.2	0.4	9.707 ± 0.023	⋯	⋯
2MASS J13412668-4341522	13:41:26.6777	−43:41:52.350	2017-01-15	23 × 45 × 1.0	7.2	0.65 ± 0.13	9.707 ± 0.023	⋯	⋯
2MASS J13591045-1950034	13:59:10.4109	−19:50:03.655	2016-06-09	30 × 45 × 1.0	12.5	0.46 ± 0.15	7.224 ± 0.034	11.600 ± 0.020	(2)
2MASS J14190331+6451463	14:19:03.2957	+64:51:46.327	2016-03-25	30 × 30 × 1.0	9.4	0.7	9.413 ± 0.023	⋯	⋯
2MASS J14190331+6451463	14:19:03.2957	+64:51:46.327	2017-06-13	26 × 45 × 1.0	10.4	0.56 ± 0.18	9.413 ± 0.023	⋯	⋯
2MASS J14252913-4113323	14:25:29.1206	−41:13:32.338	2017-05-11	20 × 45 × 1.0	6.1	0.58 ± 0.15	7.539 ± 0.026	11.480 ± 0.170	(2)
2MASS J15093920-1332119	15:09:39.1994	−13:32:12.031	2016-03-25	40 × 30 × 1.0	16.2	0.7	8.750 ± 0.023	14.076 ± 0.080	(1)
2MASS J15202415-3037317	15:20:24.1532	−30:37:31.697	2016-05-26	20 × 45 × 1.0	7.0	0.5	7.842 ± 0.025	11.049 ± 0.050	(1)
2MASS J15443518+0423075	15:44:35.1863	+04:23:07.764	2016-03-25	30 × 30 × 1.0	22.7	0.7	8.794 ± 0.024	12.190	(9)
2MASS J15594951-3628279	15:59:49.5108	−36:28:27.904	2016-03-25	26 × 30 × 1.0	6.6	0.7	7.972 ± 0.023	10.320	(10)
2MASS J16082845-0607345	16:08:28.4634	−06:07:34.501	2016-05-27	20 × 45 × 1.0	11.8	0.7	8.657 ± 0.023	13.627 ± 0.180	(1)
2MASS J16265441+1457502	16:26:54.4016	+14:57:50.162	2016-05-26	20 × 45 × 1.0	14.0	0.5	8.749 ± 0.023	13.730 ± 0.100	(1)
HIP 81084	16:33:41.6097	−09:33:11.935	2016-03-25	30 × 30 × 1.0	12.9	0.7	7.460 ± 0.033	10.840 ± 0.100	(1)
2MASS J16430128-1754274	16:43:01.2949	−17:54:27.513	2016-04-13	30 × 40 × 0.75	11.8	1.00 ± 0.26	8.444 ± 0.022	12.176 ± 0.040	(1)
2MASS J17111769+1245408	17:11:17.6929	+12:45:40.862	2016-05-27	20 × 45 × 1.0	9.5	0.7	9.379 ± 0.022	⋯	⋯
2MASS J17115853-2530585	17:11:58.5381	−25:30:58.527	2016-06-09	30 × 45 × 1.0	11.8	0.46 ± 0.15	8.869 ± 0.023	⋯	⋯
2MASS J17150219-3333398	17:15:02.1989	−33:33:40.167	2016-05-27	20 × 45 × 1.0	6.9	0.7	6.886 ± 0.050	10.463 ± 0.020	(1)
2MASS J17261525-0311308	17:26:15.2562	−03:11:30.958	2016-05-26	20 × 45 × 1.0	13.6	0.5	9.307 ± 0.023	⋯	⋯
2MASS J17300060-1840132	17:30:00.5972	−18:40:13.378	2016-07-18	20 × 45 × 1.0	6.1	0.52 ± 0.13	8.856 ± 0.023	⋯	⋯
2MASS J17520173-2357571	17:52:01.7355	−23:57:57.219	2016-07-18	20 × 45 × 1.0	7.0	0.52 ± 0.13	8.295 ± 0.024	12.275 ± 0.080	(1)
2MASS J17520294+5636278	17:52:02.9438	+56:36:27.928	2016-03-25	10 × 30 × 1.0	3.3	0.7	8.208 ± 0.023	13.062 ± 0.080	(1)
2MASS J17520294+5636278	17:52:02.9438	+56:36:27.928	2016-04-13	30 × 30 × 1.0	11.4	1.00 ± 0.26	8.208 ± 0.023	13.062 ± 0.080	(1)
2MASS J17580616-2222238	17:58:06.1545	−22:22:23.953	2016-07-18	20 × 45 × 1.0	7.7	0.52 ± 0.13	8.707 ± 0.024	12.736 ± 0.090	(1)
2MASS J18030566-0337318	18:03:05.6594	−03:37:31.863	2016-07-18	20 × 45 × 1.0	13.1	0.52 ± 0.13	9.124 ± 0.023	⋯	⋯
2MASS J18030566-0337318	18:03:05.6594	−03:37:31.863	2017-06-13	20 × 45 × 1.0	13.2	0.56 ± 0.18	9.124 ± 0.023	⋯	⋯
2MASS J18083702-0426259	18:08:37.0218	−04:26:26.003	2016-05-26	20 × 45 × 1.0	13.5	0.5	4.839 ± 0.179	⋯	⋯
2MASS J18141047-3247344	18:14:10.4818	−32:47:34.516	2016-04-13	20 × 30 × 1.0	5.6	1.00 ± 0.26	7.140 ± 0.049	⋯	⋯
2MASS J18142207-3246100	18:14:22.0736	−32:46:10.132	2016-07-18	20 × 45 × 1.0	6.8	0.52 ± 0.13	8.479 ± 0.023	12.316 ± 0.070	(1)
2MASS J18495543-0134087	18:49:55.4416	−01:34:08.797	2016-07-18	20 × 45 × 1.0	14.4	0.52 ± 0.13	8.707 ± 0.023	13.136 ± 0.100	(1)
2MASS J18495543-0134087	18:49:55.4416	−01:34:08.797	2017-06-13	20 × 45 × 1.0	13.5	0.56 ± 0.18	8.707 ± 0.023	13.136 ± 0.100	(1)
2MASS J18504448-3147472	18:50:44.4830	−31:47:47.382	2016-05-26	20 × 45 × 1.0	7.2	0.5	7.401 ± 0.034	10.745 ± 0.020	(1)
2MASS J18504448-3147472	18:50:44.4830	−31:47:47.382	2018-07-30	20 × 45 × 1.0	6.6	0.54 ± 0.21	7.401 ± 0.034	10.745 ± 0.020	(1)

Table 1
(Continued)

8

Name	$\alpha_{2000.0}$ (hh:mm:ss.ssss)	$\delta_{2000.0}$ ($\pm$ dd:mm:ss.sss)	UT Date	$N \times$ coadds $\times t_{exp}$ (s)	ΔP.A. (°)	Seeing (arcsec)	$W1$ (mag)	R (mag)	R References
2MASS J18553176-1622495	18:55:31.7608	−16:22:49.929	2017-07-04	20 × 45 × 1.0	8.3	1.13 ± 0.45	7.983 ± 0.025	12.230 ± 0.010	(1)
2MASS J18580415-2953045	18:58:04.1528	−29:53:04.669	2017-05-10	20 × 45 × 1.0	7.2	0.4	7.862 ± 0.028	11.395 ± 0.020	(1)
2MASS J18580415-2953045	18:58:04.1528	−29:53:04.669	2017-06-13	20 × 45 × 1.0	6.9	0.56 ± 0.18	7.862 ± 0.028	11.395 ± 0.020	(1)
2MASS J19243494-3442392	19:24:34.9534	−34:42:39.365	2016-05-26	20 × 45 × 1.0	6.9	0.5	8.618 ± 0.022	⋯	⋯
2MASS J19312434-2134226	19:31:24.3439	−21:34:22.777	2016-05-27	20 × 45 × 1.0	8.5	0.7	7.706 ± 0.029	11.430	(11)
2MASS J19312434-2134226	19:31:24.3439	−21:34:22.777	2018-07-30	20 × 45 × 1.0	8.0	0.54 ± 0.21	7.706 ± 0.029	11.430	(11)
2MASS J19420065-2104051	19:42:00.6517	−21:04:05.368	2016-05-27	20 × 45 × 1.0	8.6	0.7	⋯	12.806 ± 0.060	(1)
2MASS J19435432-0546363	19:43:54.3404	−05:46:36.351	2016-07-18	20 × 45 × 1.0	12.7	0.52 ± 0.13	8.706 ± 0.023	13.877 ± 0.110	(1)
2MASS J19560438-3207376	19:56:04.3718	−32:07:37.672	2016-05-27	20 × 45 × 1.0	7.1	0.7	7.711 ± 0.043	11.196 ± 0.040	(1)
2MASS J20013718-3313139	20:01:37.1727	−33:13:14.010	2017-05-10	20 × 45 × 1.0	7.0	0.4	8.163 ± 0.023	11.920 ± 0.040	(1)
2MASS J20043077-2342018	20:04:30.7865	−23:42:02.263	2016-07-18	40 × 45 × 1.0	22.9	0.52 ± 0.13	⋯	12.680 ± 0.080	(1)
2MASS J20043077-2342018	20:04:30.7865	−23:42:02.263	2018-07-30	20 × 45 × 1.0	7.5	0.54 ± 0.21	⋯	12.680 ± 0.080	(1)
2MASS J20043077-2342018	20:04:30.7865	−23:42:02.263	2017-06-13	20 × 45 × 1.0	7.7	0.56 ± 0.18	⋯	12.680 ± 0.080	(1)
V* V5663 Sgr	20:05:56.4141	−32:16:59.189	2017-05-11	20 × 45 × 1.0	6.9	0.58 ± 0.15	7.808 ± 0.029	⋯	⋯
V* V5663 Sgr	20:05:56.4141	−32:16:59.189	2017-06-13	20 × 45 × 1.0	6.6	0.56 ± 0.18	7.808 ± 0.029	⋯	⋯
2MASS J20333759-2556521	20:33:37.5959	−25:56:52.115	2017-05-11	11 × 45 × 1.0	3.9	0.58 ± 0.15	8.675 ± 0.022	13.440 ± 0.020	(2)
2MASS J20395460+0620118	20:39:54.6018	+06:20:11.867	2018-07-30	20 × 45 × 1.0	21.7	0.54 ± 0.21	7.000 ± 0.046	10.044 ± 0.016	(6)
2MASS J20395460+0620118	20:39:54.6018	+06:20:11.867	2016-06-15	30 × 25 × 1.0	21.5	0.6	7.000 ± 0.046	10.044 ± 0.016	(6)
AU Mic	20:45:09.5324	−31:20:27.237	2016-10-18	20 × 225 × 0.2	10.1	1.05 ± 0.26	4.449 ± 0.277	9.078 ± 0.060	(1)
2MASS J20465795-0259320	20:46:57.9790	−02:59:32.082	2016-05-27	20 × 45 × 1.0	14.8	0.7	8.239 ± 0.023	11.522 ± 0.040	(1)
2MASS J21073678-1304581	21:07:36.7905	−13:04:58.191	2016-10-18	20 × 45 × 1.0	9.9	1.05 ± 0.26	7.677 ± 0.030	12.349 ± 0.070	(1)
2MASS J21100535-1919573	21:10:05.3573	−19:19:57.611	2016-08-08	20 × 45 × 1.0	7.7	0.5	7.023 ± 0.048	11.381 ± 0.100	(1)
2MASS J21100535-1919573	21:10:05.3573	−19:19:57.611	2017-06-13	20 × 45 × 1.0	8.4	0.56 ± 0.18	7.023 ± 0.048	11.381 ± 0.100	(1)
2MASS J21130526-1729126	21:13:05.2764	−17:29:12.691	2016-07-18	20 × 45 × 1.0	8.7	0.52 ± 0.13	7.391 ± 0.034	⋯	⋯
[SLS2012] PYC J21148+1254	21:14:49.0988	+12:54:00.129	2017-06-13	20 × 45 × 1.0	19.6	0.56 ± 0.18	8.951 ± 0.022	13.942 ± 0.120	(1)
LO Peg	21:31:01.7140	+23:20:07.374	2016-06-15	37 × 45 × 1.0	47.6	0.6	6.338 ± 0.087	8.600	(12)
2MASS J21334415-3453372	21:33:44.1498	−34:53:37.263	2017-07-04	20 × 45 × 1.0	6.5	1.13 ± 0.45	9.280 ± 0.023	13.427 ± 0.110	(1)
2MASS J22021626-4210329	22:02:16.2563	−42:10:33.294	2018-07-30	40 × 45 × 1.0	21.6	0.54 ± 0.21	7.894 ± 0.024	⋯	⋯
2MASS J22021626-4210329	22:02:16.2563	−42:10:33.294	2017-06-13	20 × 45 × 1.0	5.7	0.56 ± 0.18	7.894 ± 0.024	⋯	⋯
PM J22088+1144	22:08:50.3373	+11:44:13.224	2017-07-04	20 × 45 × 1.0	4.4	1.13 ± 0.45	8.882 ± 0.024	14.389 ± 0.120	(1)
2MASS J22174316-1546452	22:17:43.1646	−15:46:45.279	2017-07-04	20 × 45 × 1.0	9.0	1.13 ± 0.45	9.803 ± 0.023	14.974 ± 0.040	(1)
2MASS J22274882-0113527	22:27:48.8387	−01:13:52.756	2016-11-22	20 × 45 × 1.0	15.3	0.5	8.430 ± 0.023	13.211 ± 0.100	(1)
2MASS J22274882-0113527	22:27:48.8387	−01:13:52.756	2016-10-18	6 × 45 × 1.0	3.5	1.05 ± 0.26	8.430 ± 0.023	13.211 ± 0.100	(1)
WW PsA	22:44:57.9628	−33:15:01.744	2017-07-04	20 × 45 × 1.0	6.7	1.13 ± 0.45	⋯	10.916	(7)
TX PsA	22:45:00.0641	−33:15:26.091	2016-11-23	21 × 45 × 1.0	8.5	0.69 ± 0.14	⋯	12.095	(13)
TX PsA	22:45:00.0641	−33:15:26.091	2018-07-30	30 × 45 × 1.0	11.5	0.54 ± 0.21	⋯	12.095	(13)
HIP 114066	23:06:04.8465	+63:55:34.356	2016-11-23	20 × 60 × 0.8	8.6	0.69 ± 0.14	6.939 ± 0.056	10.370 ± 0.020	(1)
HIP 114066	23:06:04.8465	+63:55:34.356	2016-09-11	25 × 45 × 1.0	27.7	0.56 ± 0.18	6.939 ± 0.056	10.370 ± 0.020	(1)
2MASS J23093711-0225551	23:09:37.1304	−02:25:55.243	2016-11-22	20 × 45 × 1.0	14.1	0.5	7.679 ± 0.030	9.850	(12)
2MASS J23282251+0028395	23:28:22.5051	+00:28:39.544	2016-10-17	20 × 45 × 1.0	15.1	0.93 ± 0.24	8.379 ± 0.023	12.919 ± 0.080	(1)
2MASS J23301341-2023271	23:30:13.4374	−20:23:27.458	2017-07-04	18 × 45 × 1.0	7.7	1.13 ± 0.45	6.230 ± 0.076	10.835 ± 0.020	(1)
2MASS J23314492-0244395	23:31:44.9255	−02:44:39.537	2017-07-05	20 × 45 × 1.0	13.0	0.77 ± 0.18	8.491 ± 0.022	13.300	(12)
2MASS J23320018-3917368	23:32:00.1839	−39:17:37.172	2016-11-22	21 × 45 × 1.0	8.6	0.5	7.879 ± 0.027	12.663 ± 0.050	(1)
2MASS J23323085-1215513	23:32:30.8611	−12:15:51.462	2017-07-05	20 × 45 × 1.0	9.9	0.77 ± 0.18	6.505 ± 0.075	10.320 ± 0.040	(1)
2MASS J23323085-1215513	23:32:30.8611	−12:15:51.462	2018-07-30	30 × 45 × 1.0	16.9	0.54 ± 0.21	6.505 ± 0.075	10.320 ± 0.040	(1)
2MASS J23331860+2714219	23:33:18.6540	+27:14:22.048	2016-07-18	20 × 45 × 1.0	29.3	0.52 ± 0.13	8.381 ± 0.022	12.976 ± 0.080	(1)
2MASS J23433386-1928024	23:43:33.8766	−19:28:02.426	2016-11-23	20 × 60 × 0.8	9.4	0.69 ± 0.14	8.315 ± 0.023	⋯	⋯

Table 1
(Continued)

Name	$\alpha_{2000.0}$ (hh:mm:ss.ssss)	$\delta_{2000.0}$ ($\pm$ dd:mm:ss.sss)	UT Date	$N \times$ coadds $\times t_{exp}$ (s)	ΔP.A. (°)	Seeing (arcsec)	$W1$ (mag)	R (mag)	R References
2MASS J23433386-1928024	23:43:33.8766	−19:28:02.426	2017-09-09	$20 \times 45 \times 1.0$	8.5	0.47 ± 0.13	8.315 ± 0.023	⋯	⋯
2MASS J23433386-1928024	23:43:33.8766	−19:28:02.426	2016-09-11	$20 \times 45 \times 1.0$	10.1	0.56 ± 0.18	8.315 ± 0.023	⋯	⋯
2MASS J23500639+2659519	23:50:06.4057	+26:59:51.953	2017-09-09	$20 \times 45 \times 1.0$	27.2	0.47 ± 0.13	9.149 ± 0.023	13.300	(12)
2MASS J23512227+2344207	23:51:22.2966	+23:44:20.580	2016-11-05	$20 \times 45 \times 1.0$	68.4	0.82 ± 0.22	8.675 ± 0.023	13.895 ± 0.130	(1)
2MASS J23513366+3127229	23:51:33.6738	+31:27:23.022	2017-09-09	$20 \times 45 \times 1.0$	13.5	0.47 ± 0.13	8.849 ± 0.022	13.105 ± 0.060	(1)
2MASS J23513366+3127229	23:51:33.6738	+31:27:23.022	2018-07-30	$10 \times 45 \times 1.0$	11.4	0.54 ± 0.21	8.849 ± 0.022	13.105 ± 0.060	(1)
2MASS J23514340+3127045	23:51:43.4147	+31:27:04.378	2017-09-09	$20 \times 45 \times 1.0$	8.1	0.47 ± 0.13	9.379 ± 0.023	14.030 ± 0.060	(1)
GJ 4379	23:57:19.3590	−12:58:40.731	2016-09-12	$20 \times 45 \times 1.0$	10.5	0.65 ± 0.22	8.071 ± 0.023	12.731 ± 0.090	(1)
Taurus Survey Targets[b]									
V* UX Tau	04:30:03.9962	+18:13:49.435	2016-10-16	$116 \times 40 \times 0.5$	199.5	1.32 ± 0.26	6.846 ± 0.084	9.830	(14)
2MASS J04090973+2901306	04:09:09.7467	+29:01:30.302	2016-10-17	$20 \times 45 \times 1.0$	6.3	0.93 ± 0.24	8.118 ± 0.022	10.240	(3)
2MASS J04032494+1724261	04:03:24.9515	+17:24:26.050	2016-10-17	$20 \times 45 \times 1.0$	1.7	0.93 ± 0.24	8.715 ± 0.023	11.220	(9)
2MASS J05071206+2437163	05:07:12.0680	+24:37:16.368	2016-10-17	$20 \times 45 \times 1.0$	13.6	0.93 ± 0.24	9.226 ± 0.023	⋯	⋯
V1195 Tau A	04:06:51.3510	+25:41:28.269	2016-10-17	$20 \times 45 \times 1.0$	8.0	0.93 ± 0.24	7.516 ± 0.027	11.370 ± 0.080	(1)
V1195 Tau B	04:06:51.3336	25:41:29.040	2016-10-17	$20 \times 45 \times 1.0$	18.2	0.93 ± 0.24	⋯	⋯	⋯
2MASS J05030659+2523197	05:03:06.5988	+25:23:19.606	2016-10-17	$20 \times 45 \times 1.0$	6.1	0.93 ± 0.24	8.191 ± 0.023	13.480 ± 0.200	(1)
2MASS J04191583+2906269	04:19:15.8339	+29:06:26.926	2016-11-10	$20 \times 90 \times 0.5$	3.6	0.45 ± 0.13	7.113 ± 0.051	11.890 ± 0.050	(1)
2MASS J04215563+2755060	04:21:55.6347	+27:55:06.184	2016-11-10	$20 \times 90 \times 0.5$	2.9	0.45 ± 0.13	7.076 ± 0.047	⋯	⋯
2MASS J04474859+2925112	04:47:48.5954	+29:25:11.191	2016-11-10	$19 \times 90 \times 0.5$	2.9	0.45 ± 0.13	7.350 ± 0.029	12.370 ± 0.130	(1)
V* V1069 Tau	04:18:51.7036	+17:23:16.582	2016-11-10	$21 \times 90 \times 0.5$	0.3	0.45 ± 0.13	9.158 ± 0.022	12.220 ± 0.070	(1)
2MASS J04162810+2807358	04:16:28.1067	+28:07:35.731	2016-11-10	$20 \times 60 \times 0.8$	33.0	0.45 ± 0.13	8.246 ± 0.023	11.825	(15)
2MASS J04184703+2820073	04:18:47.0291	+28:20:07.493	2016-11-10	$20 \times 90 \times 0.5$	6.7	0.45 ± 0.13	7.130 ± 0.033	11.210	(3)
2MASS J04194127+2749484	04:19:41.2688	+27:49:48.151	2016-11-10	$20 \times 90 \times 0.5$	13.3	0.45 ± 0.13	8.149 ± 0.023	11.140	(3)
V1070 Tau B	⋯	⋯	2016-11-10	$17 \times 90 \times 0.5$	32.1	0.45 ± 0.13	⋯	⋯	⋯
2MASS J04141700+2810578	04:14:17.0042	+28:10:57.766	2016-11-22	$20 \times 45 \times 1.0$	2.5	0.5	5.798 ± 0.134	12.860	(9)
2MASS J04215563+2755060	04:21:55.6347	+27:55:06.184	2016-11-22	$20 \times 60 \times 0.8$	30.7	0.5	7.076 ± 0.047	⋯	⋯
2MASS J04270469+2606163	04:27:04.6921	+26:06:16.060	2016-11-22	$20 \times 90 \times 0.5$	36.6	0.5	6.183 ± 0.078	12.280	(9)
2MASS J04333906+2520382	04:33:39.0767	+25:20:38.101	2016-11-22	$20 \times 60 \times 0.8$	14.3	0.5	6.938 ± 0.047	11.850	(16)
2MASS J04333405+2421170	04:33:34.0609	+24:21:17.068	2016-11-22	$20 \times 60 \times 0.8$	4.8	0.5	7.087 ± 0.106	12.150	(16)
2MASS J04333456+2421058	04:33:34.5630	+24:21:05.855	2016-11-22	$20 \times 60 \times 0.8$	2.5	0.5	6.568 ± 0.138	12.020 ± 0.140	(1)
2MASS J04354733+2250216	04:35:47.3357	+22:50:21.686	2016-11-22	$20 \times 60 \times 0.8$	1.9	0.5	6.633 ± 0.071	11.180	(3)
2MASS J04245708+2711565	04:24:57.0824	+27:11:56.539	2016-11-22	$20 \times 60 \times 0.8$	4.0	0.5	7.711 ± 0.028	12.460	(9)
2MASS J04320926+1757227	04:32:09.2839	+17:57:22.693	2016-11-22	$20 \times 60 \times 0.8$	0.2	0.5	8.749 ± 0.023	⋯	⋯
V* V1115 Tau	04:36:19.1015	+25:42:59.001	2016-11-22	$20 \times 60 \times 0.8$	2.3	0.5	8.469 ± 0.023	10.810	(3)
HD 31648	04:58:46.2655	+29:50:36.987	2016-11-22	$20 \times 150 \times 0.3$	4.1	0.5	4.868 ± 0.184	7.760	(17)
2MASS J04321583+1801387	04:32:15.8393	+18:01:38.750	2016-11-22	$20 \times 60 \times 0.8$	0.5	0.5	8.060 ± 0.024	⋯	⋯
2MASS J04331003+2433433	04:33:10.0300	+24:33:43.255	2016-11-22	$20 \times 60 \times 0.8$	8.0	0.5	8.412 ± 0.023	11.300	(3)
2MASS J04335200+2250301	04:33:52.0143	+22:50:30.094	2016-11-23	$20 \times 60 \times 0.8$	8.8	0.69 ± 0.14	6.756 ± 0.068	⋯	⋯
2MASS J04144786+2648110	04:14:47.8615	+26:48:11.014	2016-11-23	$20 \times 45 \times 1.0$	2.5	0.69 ± 0.14	8.519 ± 0.024	⋯	⋯
2MASS J04382858+2610494	04:38:28.5880	+26:10:49.467	2016-11-23	$20 \times 60 \times 0.8$	4.1	0.69 ± 0.14	6.341 ± 0.097	13.010	(9)
2MASS J04465305+1700001	04:46:53.0575	+17:00:00.136	2016-11-23	$20 \times 60 \times 0.8$	0.5	0.69 ± 0.14	7.085 ± 0.040	13.210	(6)
2MASS J04144730+2646264	04:14:47.3033	+26:46:26.414	2016-11-23	$2 \times 60 \times 0.8$	1.2	0.69 ± 0.14	8.404 ± 0.023	⋯	⋯
CoKu HP Tau G2	04:35:54.1535	+22:54:13.427	2016-11-23	$20 \times 60 \times 0.8$	12.4	0.69 ± 0.14	7.118 ± 0.046	10.14	(3)
2MASS J04355277+2254231	04:35:52.7819	+22:54:23.156	2016-11-23	$20 \times 60 \times 0.8$	71.6	0.69 ± 0.14	6.018 ± 0.057	⋯	⋯
2MASS J04295156+2606448	04:29:51.5569	+26:06:44.859	2016-11-23	$20 \times 60 \times 0.8$	2.7	0.69 ± 0.14	7.270 ± 0.037	12.280	(16)
2MASS J04331907+2246342	04:33:19.0778	+22:46:34.130	2016-11-23	$20 \times 60 \times 0.8$	2.1	0.69 ± 0.14	6.297 ± 0.079	⋯	⋯
HD 282630	04:55:36.9695	+30:17:55.101	2016-11-23	$21 \times 60 \times 0.8$	18.5	0.69 ± 0.14	8.059 ± 0.023	10.550	(3)

Table 1
(Continued)

Name	$\alpha_{2000.0}$ (hh:mm:ss.ssss)	$\delta_{2000.0}$ ($\pm$ dd:mm:ss.sss)	UT Date	$N \times$ coadds $\times t_{\exp}$ (s)	ΔP.A. (°)	Seeing (arcsec)	$W1$ (mag)	R (mag)	R References
V* V1095 Tau	04:13:14.1551	+28:19:10.668	2016-11-23	$20 \times 60 \times 0.8$	2.7	0.69 ± 0.14	8.582 ± 0.024	13.620 ± 0.100	(1)
2MASS J04345542+2428531	04:34:55.4201	+24:28:53.033	2016-11-24	$20 \times 60 \times 0.8$	5.8	0.60 ± 0.15	7.447 ± 0.036	12.030	(18)
2MASS J04554582+3033043	04:55:45.8458	+30:33:04.292	2016-11-24	$20 \times 90 \times 0.5$	4.5	0.60 ± 0.15	3.289 ± 0.450	6.960 ± 0.050	(19)
2MASS J04173372+2820468	04:17:33.7284	+28:20:46.812	2016-11-24	$20 \times 60 \times 0.8$	3.4	0.60 ± 0.15	7.791 ± 0.029	12.590	(9)
2MASS J04352737+2414589	04:35:27.3776	+24:14:58.910	2016-11-24	$20 \times 60 \times 0.8$	19.8	0.60 ± 0.15	7.657 ± 0.029	11.790	(9)
2MASS J04470620+1658428	04:47:06.2151	+16:58:42.813	2016-11-24	$29 \times 45 \times 1.0$	2.1	0.60 ± 0.15	5.834 ± 0.113	12.190 ± 0.410	(6)
2MASS J04551098+3021595	04:55:10.9815	+30:21:59.373	2016-11-24	$20 \times 60 \times 0.8$	7.8	0.60 ± 0.15	8.304 ± 0.022	11.798 ± 0.050	(1)
2MASS J04455129+1555496	04:45:51.2948	+15:55:49.632	2016-11-24	$20 \times 60 \times 0.8$	0.3	0.60 ± 0.15	7.138 ± 0.036	⋯	⋯
V* V1320 Tau	04:31:14.4389	+27:10:17.920	2016-11-24	$20 \times 60 \times 0.8$	17.1	0.60 ± 0.15	8.741 ± 0.023	11.750	(3)
WK81 1	04:19:26.2675	+28:26:14.259	2016-11-24	$20 \times 60 \times 0.8$	32.8	0.60 ± 0.15	8.270 ± 0.021	12.240	(15)
V* UX Tau	04:30:03.9962	+18:13:49.435	2017-02-11	$50 \times 30 \times 0.8$	156.3	1.3	6.846 ± 0.084	9.830	(14)
2MASS J04245708+2711565	04:24:57.0824	+27:11:56.539	2017-10-03	$130 \times 60 \times 0.7$	211.6	0.51 ± 0.13	7.711 ± 0.028	12.460	(9)
V* UX Tau	04:30:03.9962	+18:13:49.435	2017-10-04	$128 \times 60 \times 0.7$	164.2	0.60 ± 0.18	6.846 ± 0.084	9.830	(14)
[HJS91] 507	04:29:20.7035	+26:33:40.446	2017-11-09	$23 \times 45 \times 1.0$	5.6	0.74 ± 0.24	8.646 ± 0.023	⋯	⋯
2MASS J04304425+2601244	04:30:44.2433	+26:01:24.653	2017-11-09	$20 \times 45 \times 1.0$	7.7	0.74 ± 0.24	6.120 ± 0.104	12.080 ± 0.480	(1)
2MASS J04334871+1810099	04:33:48.7336	+18:10:09.973	2017-11-09	$23 \times 45 \times 1.0$	109.1	0.74 ± 0.24	9.457 ± 0.024	⋯	⋯
2MASS J04141358+2812492	04:14:13.5841	+28:12:49.168	2017-11-09	$23 \times 45 \times 1.0$	17.0	0.74 ± 0.24	8.004 ± 0.022	13.640	(9)
2MASS J04141458+2827580	04:14:14.5945	+28:27:58.067	2017-11-09	$23 \times 45 \times 1.0$	3.3	0.74 ± 0.24	7.544 ± 0.032	13.680	(9)
2MASS J04144730+2646264	04:14:47.3033	+26:46:26.414	2017-11-09	$23 \times 45 \times 1.0$	2.9	0.74 ± 0.24	8.404 ± 0.023	⋯	⋯
2MASS J04233919+2456141	04:23:39.1888	+24:56:14.250	2017-11-09	$23 \times 45 \times 1.0$	4.9	0.74 ± 0.24	7.646 ± 0.026	14.700 ± 0.110	(1)
2MASS J04430309+2520187	04:43:03.0761	+25:20:18.706	2017-11-09	$23 \times 45 \times 1.0$	2.5	0.74 ± 0.24	8.973 ± 0.022	⋯	⋯
2MASS J04035084+2610531	04:03:50.8384	+26:10:53.016	2017-11-09	$23 \times 45 \times 1.0$	2.6	0.74 ± 0.24	9.403 ± 0.023	⋯	⋯
2MASS J04352020+2232146	04:35:20.2104	+22:32:14.561	2017-11-09	$23 \times 45 \times 1.0$	6.1	0.74 ± 0.24	8.909 ± 0.024	⋯	⋯
2MASS J04220313+2825389	04:22:03.1470	+28:25:39.096	2017-11-09	$23 \times 45 \times 1.0$	4.8	0.74 ± 0.24	8.271 ± 0.022	⋯	⋯
2MASS J05074953+3024050	05:07:49.5662	+30:24:05.177	2017-11-09	$20 \times 45 \times 1.0$	3.1	0.74 ± 0.24	6.246 ± 0.093	9.950	(9)
2MASS J04181078+2519574	04:18:10.7829	+25:19:57.380	2017-11-09	$23 \times 45 \times 1.0$	2.9	0.74 ± 0.24	8.321 ± 0.023	12.880 ± 0.130	(1)
2MASS J04345693+2258358	04:34:56.9315	+22:58:35.724	2017-11-09	$23 \times 45 \times 1.0$	2.6	0.74 ± 0.24	9.125 ± 0.023	⋯	⋯
IRAS 04171+2756	04:20:26.0663	+28:04:09.048	2017-12-24	$20 \times 45 \times 1.0$	7.1	⋯	9.476 ± 0.023	⋯	⋯
[HJS91] 4872	04:25:17.6698	+26:17:50.429	2017-12-24	$20 \times 45 \times 1.0$	27.7	⋯	7.925 ± 0.025	13.670 ± 0.090	(1)
[KW97] 20-19	04:59:03.0450	+30:03:00.336	2017-12-24	$14 \times 45 \times 1.0$	8.6	⋯	8.901 ± 0.023	13.790 ± 0.070	(1)
2MASS J04323058+2419572	04:32:30.5784	+24:19:57.359	2017-12-24	$20 \times 45 \times 1.0$	8.5	⋯	7.315 ± 0.035	14.170	(3)
2MASS J04043936+2158186	04:04:39.3720	+21:58:18.557	2017-12-24	$20 \times 45 \times 1.0$	2.3	⋯	9.842 ± 0.026	⋯	⋯
2MASS J04391779+2221034	04:39:17.7911	+22:21:03.390	2017-12-24	$17 \times 60 \times 0.5$	1.4	⋯	7.504 ± 0.028	11.610	(9)
2MASS J04215740+2826355	04:21:57.4092	+28:26:35.555	2017-12-24	$20 \times 45 \times 1.0$	33.3	⋯	4.237 ± 0.088[a]	9.670	(17)
2MASS J04555938+3034015	04:55:59.3866	+30:34:01.499	2017-12-24	$20 \times 60 \times 0.5$	23.4	⋯	5.179 ± 0.184	9.170	(9)
USNO-B1.0 1172-00072216	04:20:39.1896	+27:17:31.778	2017-12-24	$20 \times 45 \times 1.0$	12.6	⋯	9.500 ± 0.024	⋯	⋯
2MASS J04360131+1726120	04:36:01.3134	+17:26:12.091	2018-09-25	$23 \times 45 \times 1.0$	0.1	0.56 ± 0.14	8.679 ± 0.024	⋯	⋯
2MASS J04411681+2840000	04:41:16.8104	+28:40:00.073	2018-09-25	$9 \times 45 \times 1.0$	7.1	0.56 ± 0.14	8.499 ± 0.024	14.590 ± 0.120	(1)
FQ Tau A	04:19:12.8126	+28:29:32.981	2018-09-25	$23 \times 45 \times 1.0$	2.9	0.56 ± 0.14	8.925 ± 0.024	15.000 ± 0.120	(1)
FQ Tau B	⋯	⋯	2018-09-25	$23 \times 45 \times 1.0$	3.5	0.56 ± 0.14	⋯	⋯	⋯
2MASS J04323176+2420029	04:32:31.7627	+24:20:03.056	2018-09-25	$20 \times 45 \times 1.0$	5.4	0.56 ± 0.14	6.150 ± 0.074	15.040	(9)
2MASS J04341099+2251445	04:34:10.9942	+22:51:44.395	2018-09-25	$23 \times 45 \times 1.0$	2.3	0.56 ± 0.14	9.370 ± 0.023	⋯	⋯
2MASS J05074953+3024050	05:07:49.5662	+30:24:05.177	2018-09-25	$18 \times 45 \times 1.0$	20.7	0.56 ± 0.14	6.246 ± 0.093	9.950	(9)
2MASS J04220496+1934483	04:22:04.9620	+19:34:48.392	2018-09-25	$23 \times 45 \times 1.0$	3.9	0.56 ± 0.14	8.475 ± 0.022	⋯	⋯
[XCR2012] TrES J042423+265008	04:24:23.2122	+26:50:08.356	2018-09-28	$28 \times 45 \times 1.0$	20.8	0.48 ± 0.12	9.540 ± 0.022	14.480	(20)
Cl* Melotte 25 LH 19	04:35:13.1712	+17:25:49.761	2018-09-28	$23 \times 45 \times 1.0$	14.9	0.48 ± 0.12	9.926 ± 0.023	⋯	⋯
2MASS J04304425+2601244	04:30:44.2433	+26:01:24.653	2018-09-28	$20 \times 45 \times 1.0$	3.4	0.48 ± 0.12	6.120 ± 0.104	12.080 ± 0.480	(1)

Table 1
(Continued)

Name	$\alpha_{2000.0}$ (hh:mm:ss.ssss)	$\delta_{2000.0}$ ($\pm$ dd:mm:ss.sss)	UT Date	$N \times$ coadds $\times t_{\exp}$ (s)	ΔP.A. (°)	Seeing (arcsec)	$W1$ (mag)	R (mag)	R References
2MASS J04323176+2420029	04:32:31.7627	+24:20:03.056	2018-09-28	$20 \times 45 \times 1.0$	3.8	0.48 ± 0.12	6.150 ± 0.074	15.040	(9)
2MASS J04315056+2424180	04:31:50.5715	+24:24:17.775	2018-09-28	$20 \times 45 \times 1.0$	7.1	0.48 ± 0.12	7.820 ± 0.027	⋯	⋯
2MASS J05074953+3024050	05:07:49.5662	+30:24:05.177	2018-09-28	$20 \times 45 \times 1.0$	3.0	0.48 ± 0.12	6.246 ± 0.093	9.950	(9)
UCAC4 591-011866	04:14:52.3104	+28:05:59.696	2018-09-28	$20 \times 45 \times 1.0$	23.5	0.48 ± 0.12	7.487 ± 0.032	⋯	⋯
2MASS J04335200+2250301	04:33:52.0143	+22:50:30.094	2018-10-21	$132 \times 40 \times 0.75$	161.2	⋯	6.756 ± 0.068	⋯	⋯
2MASS J04335200+2250301	04:33:52.0143	+22:50:30.094	2018-12-23	$87 \times 40 \times 0.75$	182.0	0.79 ± 0.20	6.756 ± 0.068	⋯	⋯
HD 31648	04:58:46.2655	+29:50:36.987	2018-12-23	$80 \times 60 \times 0.5$	132.2	0.79 ± 0.20	4.868 ± 0.184	7.760	(17)
2MASS J04333906+2520382	04:33:39.0767	+25:20:38.101	2019-01-09	$160 \times 30 \times 1.0$	220.3	0.81 ± 0.20	6.938 ± 0.047	11.850	(16)

Notes. The mean and standard deviation of seeing measurements for the night are presented as recorded by the DIMM Seeing Monitor. Seeing measurements quoted without uncertainties correspond to approximate values measured by the CFHT WX Tower Seeing Monitor. $W1$ magnitudes are retrieved from R. M. Cutri et al. (2021) unless otherwise noted next to the measurement. R magnitude uncertainties are not quoted for objects where the corresponding SIMBAD reference does not provide one.

[a] $W1$ magnitude is retrieved from R. M. Cutri (2012).

[b] The Taurus survey targets only serve as reference stars for Super-RDI reductions of the young M-star survey targets. PSF subtraction of the Taurus survey targets will be presented in Bryan et al. (2024, in preparation).

(This table is available in machine-readable form in the online article.)

References. (1) N. Zacharias et al. (2012); (2) A. R. Riedel et al. (2014); (3) A. J. Norton et al. (2007); (4) T. C. Beers et al. (2007); (5) S. Lépine & M. M. Shara (2005); (6) N. Zacharias et al. (2009); (7) C. Koen et al. (2010); (8) A. U. Landolt (2009); (9) N. Zacharias et al. (2003); (10) V. V. Makarov (2007); (11) I. N. Reid et al. (2007); (12) D. G. Monet et al. (2003); (13) L. Casagrande et al. (2008); (14) J. R. Ducati (2002); (15) J. Devor et al. (2008); (16) P. Kundurthy et al. (2006); (17) I. Mendigutía et al. (2012); (18) R. A. Arnold et al. (2020); (19) A. Tannirkulam et al. (2008); (20) L. A. Cieza et al. (2012); (21) A. J. Norton et al. (2007).
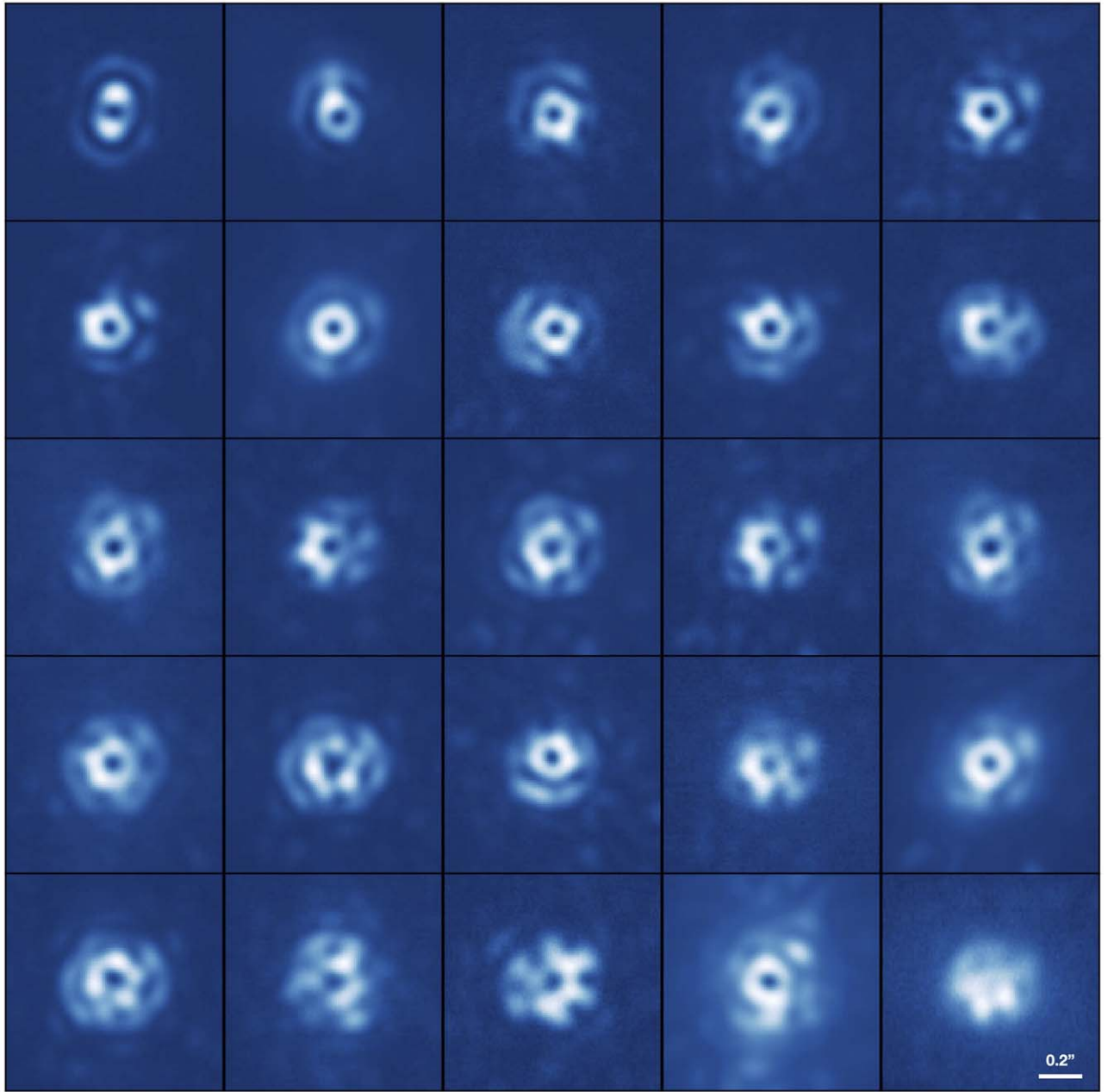
Figure 2. Gallery of 25 example sky-subtracted image cutouts (centered on target) drawn randomly from our NIRC2 vortex coronagraphic observations. The dimensions of each cutout are 101×101 pixels ($1'' \times 1''$). The images are depicted in linear scale in normalized analog to digital units and are ordered left to right, top to bottom in ascending order of raw contrast level at a fixed radial separation ($\sim 10^{-2}$ at $0''15$). The diversity of PSF shapes highlights the importance of using frame selection techniques to achieve optimal performance with the RDI strategy.

achieve optimal PSF subtraction at small angular separations with the RDI strategy. The framework is applicable to direct imaging data with any instrument and is not restricted to Keck/NIRC2 observations. Broadly, the framework encapsulates the following three steps: (1) use of image similarity metrics to rank and select the best matching reference stars uniquely for each target; (2) optimization of free parameters using synthetic companion injection-recovery tests to maximize detection sensitivity; and (3) uniform processing and sensitivity analysis of the data set using the optimized set of reduction parameters. In this work, we will present the reductions and sensitivity curves of targets in the young M-star survey sample (195 observations of 157 unique targets). While the Taurus survey targets have been used as reference stars in subsequent

procedures, their reductions and sensitivity curves will be presented in Bryan et al. (2024, in preparation). We discuss each of the above steps and their application to our sample in the following subsections.

4.1. Image Similarity Metrics

An important factor affecting the performance of RDI is the quality of individual frames (see example gallery of PSFs in Figure 2) in the reference library (G. Ruane et al. 2019; A. Sanghi et al. 2022). Preselecting reference frames is a necessary step to achieve high-contrast ratios at small angular separations. This has been demonstrated in the past by several ground- and space-based high-contrast imaging studies (see

Section [1]). A powerful technique for frame preselection is to use statistical image similarity metrics. Image similarity metrics aid the identification of a set of reference PSFs that are most similar, in structure and intensity distribution, to the science observations. This reduces random speckle noise in post-processed images and enables us to achieve higher sensitivity to potential companions and disks of interest. In this study, we use a set of five image similarity metrics to rank reference frames for each individual target in the sample. Three of the metrics are drawn from the study conducted by G. Ruane et al. ([2019]): MSE, Pearson's correlation coefficient (PCC), and structural similarity index metric (SSIM). The remaining two metrics have been newly developed as part of this work: flux logarithmic standard deviation indicator (FLSI) and contrast logarithmic standard deviation indicator (CLSI).

4.1.1. MSE, PCC, and SSIM

We refer the reader to G. Ruane et al. ([2019]) for a detailed discussion on the MSE, PCC, and SSIM metrics as well as their quantitative definitions. Qualitative interpretations of the three metrics are described below. MSE is a measure of the absolute error between two images. A lower MSE is preferred during reference frame preselection. One drawback of the metric is that its value is dependent on image intensity. Thus, two stars with similar PSF structure and quality but different brightnesses may yield a high MSE value.[14] PCC is a normalized measure of the correlation between two image frames. A higher PCC is preferred during reference frame preselection. SSIM is a perception-based model that considers changes in structural information. Structural information encapsulates the idea that pixels have strong interdependencies when they are spatially close. SSIM consists of a luminance, contrast, and structural term. The luminance and structural terms behave similarly to the MSE and PCC, respectively. Thus, SSIM can be thought of as a mixture between the MSE and PCC metrics. A higher SSIM is preferred during reference frame preselection.

4.1.2. FLSI and CLSI

We present the calculation of two new image similarity metrics that help quantify the similarity in radial flux and raw contrast distributions between two image frames. FLSI is derived as follows. Given a reference frame, we construct 1 FWHM (≈ 8 pixels) diameter apertures at a fixed angular separation from the star center. The pixel intensities in each aperture are integrated and the mean integrated aperture flux value is determined at the given separation for each frame. This procedure is repeated for a range of separations from the center of the star to obtain the mean integrated aperture flux value as a function of separation. We term the above as the mean flux curve F_{ik} for the ith frame of the kth reference star. Mean flux curves are computed for all image frames of all reference stars in the library. Next, the procedure is repeated for all frames of the science target. We average the mean flux curves corresponding to all science target frames to obtain the

representative mean flux curve for the science target (F_M). Finally, FLSI for the ith frame of the kth reference star with respect to the science target is given by the following calculation:

$$\text{FLSI}_{ik} = \text{std}(\log_{10} F_{ik} - \log_{10} F_M), \qquad (1)$$

where the standard deviation of quantity X (with N values and mean $\bar{X}$) is defined as

$$\text{std}(X) = \sqrt{\frac{1}{N-1}\sum_{i=1}^{N}(X_i - \bar{X})^2}. \qquad (2)$$

This metric quantifies image similarity as similarity in radial flux distributions. While the absolute value of the flux (as characterized by mean flux curves) may differ between the science target and the chosen reference frame, a constant logarithmic difference in the mean flux curves across multiple separations would point to a good match. Mathematically, a constant logarithmic difference would be indicated by a low standard deviation in the differences measured as a function of separation (i.e., low FLSI).

We follow a similar procedure to calculate CLSI. The key difference is that instead of calculating the mean integrated aperture flux as a function of separation, we determine the 5σ raw contrast as a function of separation. The 5σ raw contrast is defined as five times the standard deviation of the integrated aperture fluxes at a given separation normalized by the host star flux. If C_{ik} is the raw contrast curve for the ith frame of the kth reference star and C_M is the average of the raw contrast curves of all frames of the science target, then CLSI for the given reference frame is calculated as

$$\text{CLSI}_{ik} = \text{std}(\log_{10} C_{ik} - \log_{10} C_M). \qquad (3)$$

This metric quantifies image similarity as similarity in radial raw contrast distributions. Similar to FLSI, a low CLSI value is preferred during reference frame preselection.

4.1.3. Application to the Sample

Identifying the best reference frames based on image similarity metrics during image post-processing requires us to compute and store the metric values for all frames in the sample against every other frame (note that there are no designated reference stars, all reference stars are also science targets in the data set). The data structure that enables this is a covariance-style three-dimensional matrix of metric values called the metric covariance cube (Figure [3]). Since there are 7060 frames in our library and five image similarity metrics, we build a $7060 \times 7060 \times 5$ matrix of metric values. The first two indices identify the two frames for which the metric is calculated. The third index identifies which metric is calculated. Building this matrix as a whole is computationally expensive. The computation time can be significantly cut down by recognizing that the matrix is symmetric for any given image similarity metric. The order of the frames does not change the computed metric values. To speed up the remaining computations, we make use of the Caltech high-performance computing cluster (HPC) to run parallelized metric computations. The advantage of building a single matrix of metric values is that during PSF subtraction, it is inexpensive to obtain the metric-ordered set of best-matched reference frames for a given target and a given metric. Moreover, it provides the flexibility of either selecting a

---

[14] A possible solution is to weight each reference PSF by a scaling factor that minimizes the residuals with the science PSF before calculating an MSE value. While we did not implement this, the complementarity of other metrics used in this work (such as PCC, which would yield a favorable value in this case) and that the majority of targets in our sample are of the same spectral type (M dwarfs) limit this drawback. Additionally, such a situation has a low probability of occurrence given that the PSF morphology will likely change between stars that differ in brightness due to a difference in AO performance.
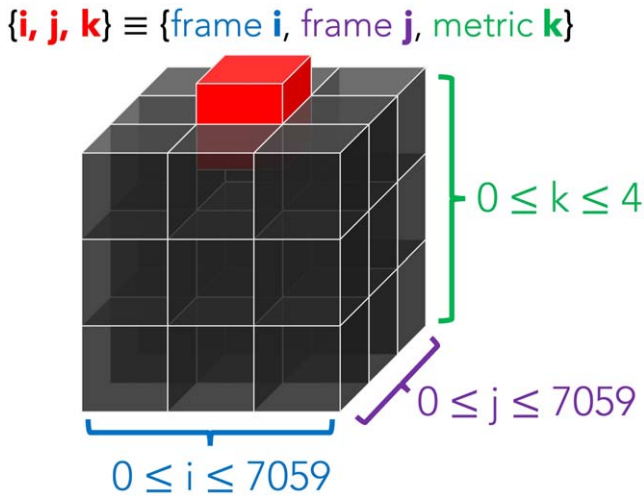
Figure 3. A diagrammatic illustration of the metric covariance cube. This represents the data structure used to store image similarity metric values for each pair of science and reference frames. The red cube is an example location in the matrix where the metric value is stored, as described by three indices. The first two indices of the matrix uniquely identify the pair of frames for which the metric is calculated and the third index identifies the metric whose value is stored.

single metric-ordered reference library for all frames of a given science target star or selecting a different metric-ordered reference library for each science target frame. We note that MSE, PCC, and SSIM are calculated over a frame size of 101×101 pixels ($\approx 1''$ field of view across each axis). Since FLSI and CLSI are specifically designed to probe the intensity distribution in coronagraphic images at close separations, they are derived based on mean flux/raw contrast curves calculated over a fixed range of separations from $0''.05$ to $0''.3$, which encompasses the post-coronagraphic PSF pattern.

4.2. Free Parameter Optimization with Injection-recovery Tests

The application of RDI involves a number of free parameters: (1) image similarity metric by which pre-frame ordering is performed; (2) the number of reference frames (library size) used to construct the principal component (PC) modes; and (3) the number of PCs used to model the stellar PSF for PSF subtraction in the implementation of the Karhunen–Loève Image Processing (KLIP; R. Soummer et al. 2012) algorithm. Computationally, it is impractical to reduce all targets in the sample using every possible combination of image similarity metric, library size, and PCs. To systematically investigate the performance of RDI with varying choice of metrics (m), library size (l), and number of PCs (p), we use synthetic companion injection-recovery tests on a random subset of 50 targets in our sample. The results can provide a good estimate of the optimal set of free parameters that will improve detection sensitivity to point sources for our complete sample. The steps followed are described below.

1. For a given science target, we carry out PSF subtraction using a full-frame PCA-based approach implemented with the `pca_fullfr` function in the VIP (C. A. Gomez Gonzalez et al. 2017; V. Christiaens et al. 2023) package. KLIP subtraction is performed using a fiducial set of parameters ($m_0 =$ PCC, $l_0 = 500$, $p_0 = 10$): the frames in the reference library are arranged in descending

order of their PCC values, the first 500 frames are selected for PSF modeling, and 10 PCs are used for PSF subtraction.

2. The speckle noise is measured as a function of separation (between 2 and 5 λ/D) from the host star in the PSF-subtracted image incorporating small sample corrections as described in D. Mawet et al. (2014). Using the speckle noise measurement, we determine the flux of a point source that would yield a 10σ detection following similar post-processing, as a function of separation.

3. A synthetic companion is injected at a given separation and position angle in the science target frames using VIP's `cube_inject_companions` function. We normalize the unocculted PSF observation for the given science target and use it as a PSF template for injection. We inject point sources for all combinations of four separations (2, 3, 4, and 5 λ/D) and four position angles (0°, 90°, 180°, 270°). This results in a set of 16 point-source-injected science target frames. For each combination, we perform PSF subtraction procedures with the fiducial parameters, yielding a total of 16 PSF-subtracted images.

4. The synthetic companion is recovered in each of the PSF-subtracted images. We measure the synthetic companion's flux in each PSF-subtracted image using aperture photometry (1 FWHM diameter aperture). This enables a calculation of the KLIP algorithm's throughput as the ratio of the recovered flux and injected flux (computed in step 2) for each combination of separation and position angle of injection.

5. A throughput correction is applied to the flux levels determined in step 2 based on the calculations in step 4. The synthetic companions are then re-injected at the same separations and position angles as before in our science target frames. Steps 1–4 ensure that the synthetic companions are injected at a fixed signal-to-noise ratio (S/N) across all separations and position angles. Thus, when we explore the free parameter space in the next step, any changes in the S/N of the injected synthetic companions can be attributed to changes in our choice of free parameters.

6. PSF subtraction is performed on all 16 sets of throughput-corrected synthetic companion-injected target frames over the complete free parameter space (m, l, p; ranges discussed below). The S/N of each recovered synthetic companion is measured to quantify detection significance. This serves as an indicator of the performance of RDI for the tested set of free parameters.

For our data set, we explored the following free parameter ranges: all five metrics (MSE, PCC, SSIM, FLSI, CLSI), 10 equally logarithmically spaced library sizes ranging from 50 to 7000 frames, 10 equally logarithmically spaced PC values ranging from 10 to 7000 PCs. We cannot generate more PCs than the library size. Thus, library size and PC pairs where the number of PCs exceeded the library size were skipped and the S/N was set to a NaN value.

Following step 6, we investigate the S/Ns of the retrieved synthetic companions as a function of free parameters (m, l, p) to identify the optimal set of parameter combinations that maximize the detection significance. We conduct this analysis in two steps. First, we determine the best-performing image similarity metric. This metric will be used to reduce the full
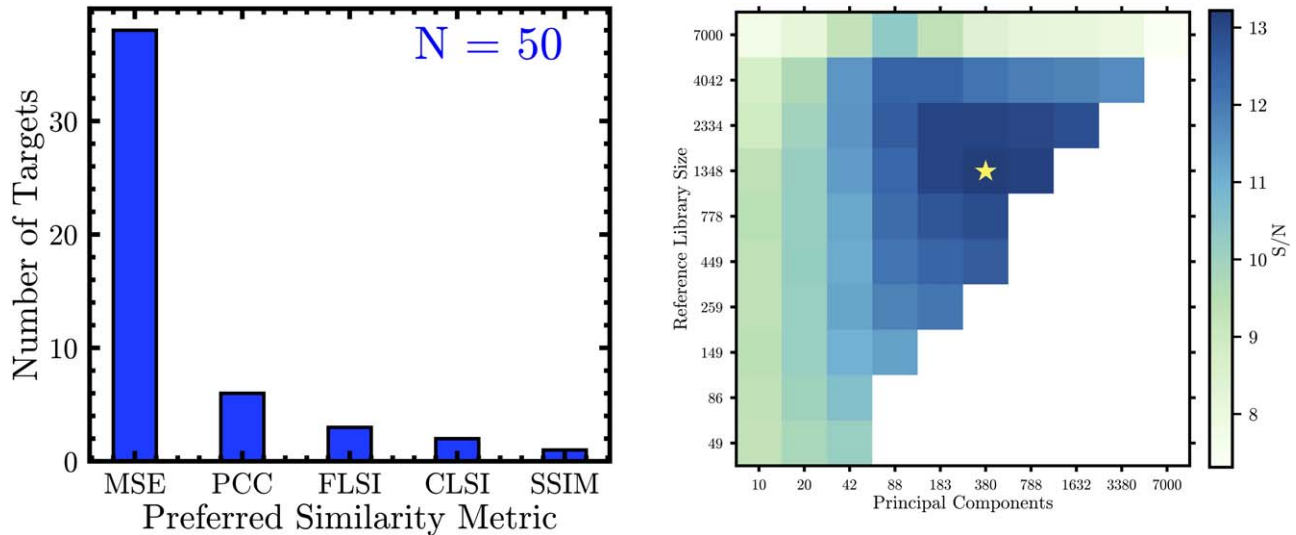
Figure 4. Free parameter optimization results. Left: histogram depicting the number of targets in the injection-recovery subset that yield the highest average S/N for the injected synthetic companion when a given image similarity metric is used for pre-frame ordering. MSE is strongly preferred, accounting for random Poisson uncertainty. Right: S/N map of the injected synthetic companions as a function of library size and PCs. Combinations where the number of PCs exceeds the number of reference frames in the library are set to a NaN value. The yellow star indicates the combination of library size and number of PCs that yields the maximum S/N in our tests.

young M-star survey sample. For a given target, we marginalize across parameters l and p (including separations and position angles of injected sources) by averaging the S/Ns obtained from injection-recovery tests. The metric that then yields the highest average S/N for a given science target is recorded as the preferred similarity metric. This calculation is repeated for all 50 targets in the injection-recovery sample subset and a histogram of metric preferences is generated (left panel, Figure 4). 38 of the 50 targets prefer MSE for pre-frame ordering. If our data set did not statistically favor a particular image similarity metric for pre-frame ordering, the number of targets that prefer MSE in the above experiment for a random sample of 50 stars should follow a binomial distribution (X) with parameters ($n = 50$, $p = 0.2$). For this distribution, the corresponding false alarm probability $P(X \geqslant 38) = 2.5 \times 10^{-17}$ is extremely small. Thus, accounting for random statistics, MSE is strongly preferred by our injection-recovery subset. We can confidently adopt MSE for pre-frame ordering of reference frames for the RDI reduction of the full young M-star survey sample.

Next, given the choice of the MSE metric, we explore the 2D parameter space defined by the reference library size (parameter l) and the number of PCs (parameter p). For given (l, p), we marginalize across all separations of injection, position angles of injection, and 50 targets by averaging the S/Ns obtained from injection-recovery tests only for the MSE metric. This procedure yields a 2D S/N map as a function of l and p and encapsulates the information from all targets in the subset (right panel; Figure 4). Examining the S/N map, we find a local S/N maxima at a library size of 1348 frames and 380 PCs. Our results reflect that small library sizes do not sufficiently capture the PSF structure, whereas very large library sizes include poor matching reference frames, which generate PC modes that add noise to the data. We favor a higher number of PCs since they fit more features in the PSF and enable better subtraction results.

These results allow us to define the set of library sizes and PCs to be adopted for the uniform processing of all targets in

the sample. For this purpose, we select three library sizes: 1000, 1750, and 3000 frames. These are chosen to sample the localized high S/N region (Figure 4) while balancing post-processing computational costs: adding new library size options significantly increases the computing time. In contrast, the addition of new PC options does not significantly increase the computing time. Thus, we only adopt an upper limit of 500 PCs based on the S/N map (Figure 4). Testing a range of PCs is important to understanding the evolution of speckles in the PSF-subtracted images and can enable their differentiation from true astrophysical sources. Additionally, the optimal number of PCs needed for recovery of an astrophysical source can vary with the separation of the source (e.g., T. Meshkat et al. 2014; M. J. Bonse et al. 2024).

It is interesting to note here that if we would have restricted ourselves to using reference frames from the same night as the target, we would have only been able to compile reference libraries of sizes, at maximum, a few hundred frames. This is suboptimal based on our injection-recovery tests. Further, we emphasize that our optimized parameters may not generally apply to data sets other than the one presented in this work. The choice of optimal metric, library size, and PCs is highly sensitive to the quality of reference stars obtained and thus may yield different results for different observational samples. Nevertheless, the Super-RDI framework developed in this work can be universally applied to accurately identify the optimal set of reduction parameters for a given data set.

4.3. Uniform Post-processing and Contrast Curve Determination

The synthetic companion injection-recovery tests enabled the determination of the optimal set of free parameters for the reduction of the full sample. The adopted parameters were: MSE metric for pre-frame ordering, library sizes $l = 1000$, 1750, 3000 frames, and $p = 1$, 5, 10, 20, 50, 100, 200, 300, 400, 500 PCs. Additionally, to efficiently search for close-in and wide-separation companions, we choose three combinations of full-frame (f) and numerical central mask (cm; centered on the host star) sizes for the

PCA-based PSF subtraction procedures: (1) 101×101 pixel frame with a 1 FWHM ($\approx$80 mas) central mask; (2) 201×201 pixel frame with a 2 FWHM central mask; and (3) 551×551 pixel frame with a 5 FWHM central mask. For the 551×551 pixel frame size, we only reduce targets with 1750 reference frames due to the increased computational expense. We uniformly reduce the entire young M-star survey data set (195 observations of 157 unique targets) for all combinations of (l, p, f, cm) using VIP's pca_fullfr function. Simultaneously, after every reduction, we compute the 5σ contrast curve for the final PSF-subtracted image using VIP's contrast_curve function. This function also calibrates the contrast curves for the KLIP algorithm's throughput losses through synthetic companion injection and retrieval. Two data products are generated per science target: 70 PSF-subtracted images and 70 5σ contrast curves (three library sizes $\times$ 10 PCs each for the 101×101 pixel and 201×201 pixel reductions and one library size $\times$ 10 PCs for the 551×551 pixel reductions). Each target was reduced on the HPC and took an average of 4 hr to complete on a single node with 32 processes. We note here that three out of the 195 science observations in the young M-star survey sample were omitted when performing the above reduction procedures either because of data processing errors in the pipeline or the lack of an unocculted PSF: [SLS2012] PYC J00390+1330 (2018 July 30), 2MASS J06135773-2723550 (2017 January 15), and 2MASS J14190331+6451463 (2016 March 25). These omissions do not impact subsequent performance analysis. We provide the Super-RDI reduced images for all targets in the young M-star survey on Zenodo[15] for public access. Finally, we create a single "principal" Super-RDI contrast curve for each target. This is done by combining the contrast curves from all three frame sizes and using the deepest contrast value at each separation across all reductions (where l and p vary). The Super-RDI principal contrast curves cover a separation range of $0\overset{''}{.}1$–$2\overset{''}{.}63$.

5. ADI

We also reduce the full young M-star survey sample with a widely used implementation of ADI-based PSF subtraction and compute the corresponding 5σ contrast curves using VIP for comparison with Super-RDI. Several studies in the past have explored optimizing the performance of ADI similar to our exploration for RDI (e.g., D. Lafrenière et al. 2007b; J. I. Adams Redai et al. 2023). There are three basic PCA-KLIP parameters that influence the contrast achieved by ADI: (1) the fitting area or search zone over which PCA-KLIP is independently applied; (2) a rotation gap criterion which excludes frames with field rotation less than the specified value to reduce the impact of self-subtraction; and (3) number of principal components (PCs) used to construct the PSF model. A complete exploration of the free parameter space above is outside the scope of this work. For our data set, we use the following combination of free parameter settings.

We adopt similar frame size and central mask settings as our Super-RDI optimizations: 101×101 pixels with a 1 FWHM ($\approx$80 mas) mask and 551×551 pixels with a 5 FWHM mask. We did not consider 201×201 pixel reductions with a 2 FWHM mask as they did not improve contrast compared to the above two settings based on tests with a representative sample of our targets. For reductions with a frame size of $101 \times$

101 pixels and a 1 FWHM central mask, we generate contrast curves for both full-frame and annular PCA-KLIP reductions of the sample. For the annular PCA-KLIP contrast curve calculations, we fix the radial size of each annulus to be 1 FWHM and apply a rotation gap criterion of 0 (no frame exclusion), 0.1, 0.5, 1, and 2 FWHM. Due to the low P.A. rotation of our data set, we could apply the 0.1, 0.5, 1, and 2 FWHM rotation gap criterion only for 121, 4, 2, and 1 observations (out of 195), respectively, in our sample without excluding all available frames. For each of the above settings, we generate contrast curves for a variable number of PCs generally ranging from 1 PC to the number of ADI frames in steps of 1 or 2 PCs. Since our primary goal is to compare the performance of ADI with Super-RDI at small angular separations, we only perform full-frame PCA-KLIP reductions for the 551×551 pixel frame size and 5 FWHM central mask setting with a variable number of PCs. We also note that there is a significant computational expense associated with parameter optimization for this frame size. Appendix A provides more information about the outcomes of parameter optimization with the 101×101 pixel reductions in the context of our survey data set.

We note that there are two improvements that can be made to the above widely used implementation of ADI that may affect sensitivity to point sources. First, the zone geometry in annular PCA-KLIP reductions can be further optimized by dividing the annuli into wedge-like sectors (e.g., D. Lafrenière et al. 2007b). This may help by providing a less underdetermined fit to the PSF. We did not experiment with this setup since we find that full-frame ADI generally performs better than annular ADI for our observations (Appendix A). Second, similar to Super-RDI, it is possible to implement correlation-based frame selection in ADI post-processing. It has been previously demonstrated that this can boost contrast performance and the S/N of point sources (C. Marois et al. 2010; T. Currie et al. 2012, 2014; L. Pueyo 2016). However, given the low number of ADI frames available per sequence ($\approx$20) in our data set, excluding additional frames is not likely to provide significant improvements in sensitivity for our observations. We keep as many science frames per target as possible to average temporary alignment errors, AO instability, and sky transmission variations. We only discarded frames with obvious issues (e.g., star not behind the vortex coronagraph).

We create a single "principal" ADI contrast curve for each target. This is done by combining the contrast curves from the two frame sizes and using the deepest contrast value at each separation across all reductions (where the fitting area, rotation gap criterion, and number of PCs vary as described above). The ADI principal contrast curves cover a separation range of $0\overset{''}{.}1$–$2\overset{''}{.}63$. Finally, we also combine the Super-RDI and ADI principal contrast curves for each target by selecting the deepest contrast value at each separation to generate a final "optimal" contrast curve. These are plotted in Figure 5 along with the median optimal contrast curve computed across all targets. A few contrast curves show irregularities due to the presence of point sources or image artifacts. These comprise a negligible percentage of the total sample and do not impact our analyses. The final optimal contrast curves can be used to incorporate our results in future substellar demographic studies. We provide these on Zenodo[16] for public access. Optimal
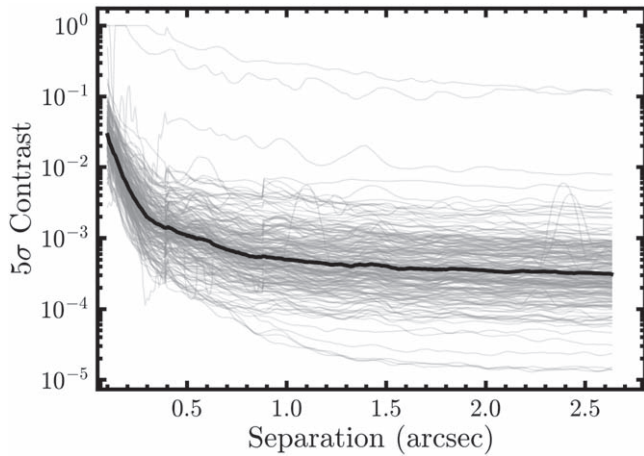

Figure 5. "Optimal" 5σ contrast curves for 192 observations in the young M-star survey (gray curves) constructed by selecting the deepest achieved contrast as a function of separation from the combination of Super-RDI and ADI principal contrast curves. The median optimal contrast curve is plotted in black. A few contrast curves show irregularities due to the presence of point sources or image artifacts.

contrasts at select separations are included in Table B1 in Appendix B.

6. Super-RDI Performance Characterization

To analyze the performance of Super-RDI, we use the 5σ contrast curves computed previously as our primary tool. They are a measure of our sensitivity to companions after PSF subtraction. In this section, we (1) compare the contrast achieved by Super-RDI against ADI; (2) investigate the dependence of the performance of Super-RDI in comparison to ADI on the P.A. rotation of our data set; and (3) examine Super-RDI's sensitivity as a function of host star *W1* and *R* magnitude.[17]

6.1. Super-RDI versus ADI for the Young M-star Survey

6.1.1. Preamble

Here, we use the 5σ Super-RDI and ADI principal contrast curves to determine which strategy performs better as a function of separation from the host star for observations obtained in the young M-star survey. There are certain aspects of our data set that must be considered before interpreting the results in this section.

1. The young M-star survey observations have a median P. A. rotation of $8\overset{\circ}{.}6$ and a mean P.A. rotation of $16.\overset{\circ}{}4$. This corresponds to a physical rotation of 0.38 FWHM and 0.73 FWHM at $0\overset{''}{.}2$ separation and 0.76 FWHM and 1.46 FWHM at $0\overset{''}{.}4$ separation, respectively. Thus, ADI reductions are expected to suffer from self-subtraction effects for a significant number of targets in the sample at small angular separations. The performance comparison of Super-RDI with ADI as a function of P.A. is discussed in detail in the next section.
2. The typical number of exposures for targets in the sample is $\sim$20. For a 1 FWHM width annulus at $0\overset{''}{.}2$ and $0\overset{''}{.}4$

---

separation, there are $\approx$15 and $\approx$30 independent speckle realizations (where a speckle typically has size $\sim$1 FWHM), respectively. Thus, there are cases where PSF fitting with observations in our ADI sequences may be underdetermined even at small angular separations. In contrast, a 101×101 pixel full-frame size includes $\sim$200 independent speckle realizations and our Super-RDI reductions use reference library sizes that are typically much larger (1000–3000 frames) for PSF fitting.

These characteristics of the data set lead us to expect that Super-RDI will perform better than ADI in the speckle-dominated noise regime (small angular separations) for our observations. As discussed in Section 2.2, the above characteristics of our data set are a result of the design of the young M-star survey under the practical considerations of observing a large number of targets with limited availability of telescope time (which determines the number of exposures obtained and P.A. rotation achieved) and scheduling conflicts within a given night (which determines if targets can be observed near transit, where the P.A. rotation is largest).

In this context, the goal of the following analysis is to understand where the performance transition between ADI and Super-RDI occurs for young M-star survey observations in separation space. These results can inform the design of future high-contrast imaging surveys. Such analyses have previously been conducted in literature. For example, G. Ruane et al. (2017) provided the first performance comparison between RDI and ADI with the Keck/NIRC2 vortex coronagraph in imaging observations of a single target, TW Hya, where they achieved $\approx$45° rotation on three separate nights. They found that RDI (using designated reference stars imaged before and after the science target) achieves better contrast than ADI at separations $\lesssim 0\overset{''}{.}25$ when data from all three nights were combined. W. J. Xuan et al. (2018) used a significantly larger Keck/ NIRC2 L' and M_s data set consisting of 359 observations of 304 unique stars, with median and mean P.A. rotations of $11\overset{\circ}{.}1$ and $26.\overset{\circ}{}0$, respectively, and found that RDI performed better than ADI at separations $\lesssim 0\overset{''}{.}25$, averaged across all the targets in their sample. In their work, RDI was performed using designated reference stars or all stars observed on the same night as the science target. We note here that the observations used by W. J. Xuan et al. (2018) in their analyses include all the observations presented in this work as part of the young M-star survey. This allows us to make a more direct comparison between Super-RDI and the implementation of RDI using same-night reference star observations.

6.1.2. Contrast Curve Comparison

First, contrast is converted to units of Δmag. Next, we compute the average and median of the 5σ Super-RDI and ADI principal contrast curves across all targets. Taking the difference of the corresponding Super-RDI and ADI average and median principal contrast curves provides an estimate of the difference in sensitivity achieved between the two techniques as a function of separation. We plot this difference in Figure 6. For the young M-star survey, Super-RDI outperforms a widely used implementation of ADI-based PSF subtraction at separations $\lesssim 0\overset{''}{.}4$ ($\approx 5\lambda/D$), gaining as much as 0.25 mag in contrast at $0\overset{''}{.}25$ and 0.4 mag in contrast at $0\overset{''}{.}15$. The contrast gain achieved by Super-RDI increases as the separation decreases. ADI outperforms Super-RDI for
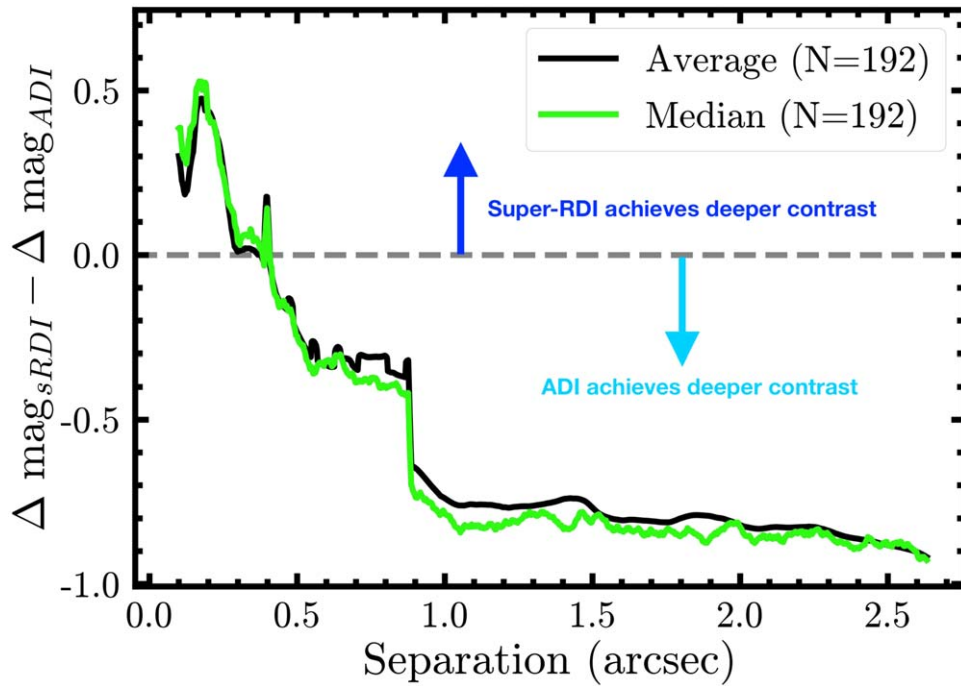

Figure 6. Super-RDI vs. ADI for the young M-star survey: Average (black) and median (green) difference in Super-RDI (sRDI) and ADI contrast (units of Δmag) as a function of separation (units of arcseconds). A gray dashed line marks zero difference and corresponds to both techniques achieving the same sensitivity level. Positive differences indicate better Super-RDI performance and negative differences indicate better ADI performance. For the typical P.A. rotation of the young M-star survey ($\sim$10°), Super-RDI outperforms a widely used implementation of ADI-based PSF subtraction at separations $\lesssim 0\rlap{.}''4$, averaged across all observations.

separations $\gtrsim 0\rlap{.}''4$. The location of the transition separation in contrast performance is determined by the rate of ADI's decline in performance due to self-subtraction effects in comparison to the rate of RDI's decline in performance due to oversubtraction effects. Compared to the implementation of RDI with same-night reference star observations in W. J. Xuan et al. (2018), the Super-RDI framework represents a performance improvement in separation space, from previously achieving deeper contrasts compared to ADI at separations $\lesssim 0\rlap{.}''25$ to now achieving deeper contrasts compared to ADI at separations $\lesssim 0\rlap{.}''4$. Super-RDI reduces speckle noise in the PSF-subtracted images through metric-based frame selection and finds the optimal number of KLIP PCs by maximizing the S/N of synthetic companions in our injection-recovery tests. This helps reduce the impact of oversubtraction and yields improvements in RDI's performance at small angular separations. In Figure 6, we observe a step-like feature at $\approx 0\rlap{.}''9$. This is a consequence of the frame sizes selected in our reduction pipeline. The step-like feature occurs at the contrast calculation boundary of the 201×201 pixel frame reductions. It indicates a transition to contrast values obtained with the 551×551 pixel frame reductions, where the performance of Super-RDI degrades significantly. This is likely because the similarity between reference and science frames is poorer at wide angular separations from the central speckle halo (the region over which the metrics are computed). Excluding the step-like artifact discussed above, we observe that the difference in contrasts achieved by the two techniques remains roughly constant beyond $0\rlap{.}''6$. This marks the transition from the speckle-dominated noise regime to the background-limited noise regime. The above results demonstrate that Super-RDI is the preferred strategy for the detection of companions at small angular separations ($\lesssim 0\rlap{.}''4$) in the context of our survey design, for a data set with a median P.A. rotation of $8\rlap{.}°6$. ADI remains

the preferred strategy for companion searches at wider angular separations.

As we discussed in Section 4.2, it is important to note that the optimal reduction parameters (which directly impact Super-RDI's performance) are specific to the observational sample used in this work. They may change for different data sets. Further, the analysis above is conducted for a group of targets. The performance of Super-RDI may vary between individual targets. In practice, we recommend complementing the application of Super-RDI with dedicated reference star observations to ensure the best performance for science targets.

6.2. Dependence on P.A. Rotation

We investigate the dependence of the performance of Super-RDI in comparison to ADI on the P.A. rotation (ΔP.A.) of our data set. The targets are sorted into four ΔP.A. bins: 0°–5°, 5°–10°, 10°–30°, and 30°–90° (for the young M-star survey data set, the maximum ΔP.A. $= 89\rlap{.}°2$). Similar to Section 6.1, we compute the median Super-RDI and ADI principal contrast curve across all targets in a given ΔP.A. bin and present the difference in contrasts between the two in Figure 7. The analysis in Section 6.1 showed that for our data set, Super-RDI improves upon ADI at separations $\lesssim 0\rlap{.}''4$ (averaged across the entire sample). Here, we find that for targets with ΔP.A. $= 0°$–5°, Super-RDI outperforms ADI up to a much larger separation of $1\rlap{.}''4$ due to the severe self-subtraction effects experienced by ADI. For targets with ΔP.A. $= 5°$–10°, Super-RDI outperforms ADI at separations $\lesssim 0\rlap{.}''4$, consistent with the average in Section 6.1. For targets with ΔP.A. $= 10°$–30°, Super-RDI's advantage in separation space reduces to $\lesssim 0\rlap{.}''25$. ADI achieves deeper contrasts across all separations for targets with ΔP.A. $= 30°$–90°. Note that the results for the smallest and largest ΔP.A. value bins are based on a comparatively small sample of
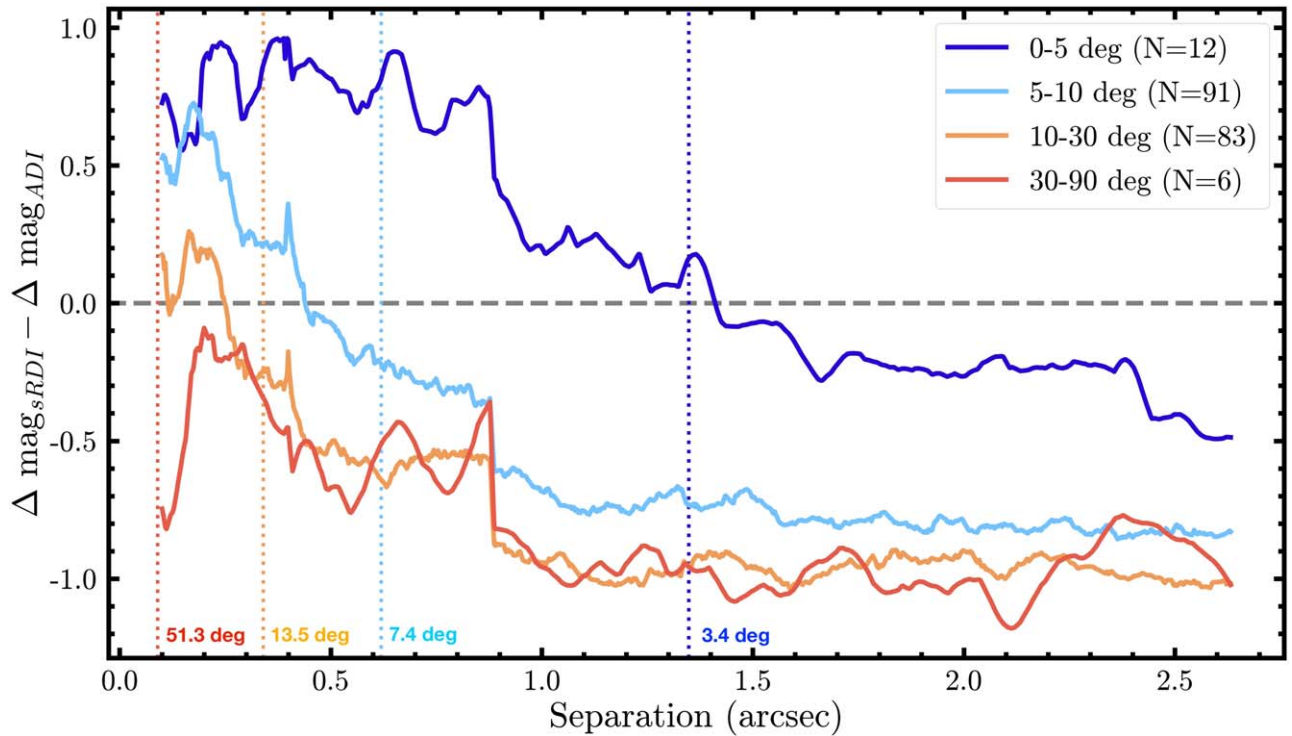
Figure 7. Median difference in Super-RDI (sRDI) and ADI contrast (units of Δmag) as a function of separation (units of arcseconds) for observations sorted into four ΔP.A. bins (units of degrees). A horizontal gray dashed line marks zero difference and corresponds to both techniques achieving the same sensitivity level. Positive differences indicate better Super-RDI performance and negative differences indicate better ADI performance. Vertical dashed lines mark the separations at which 1 FWHM rotation is achieved for the median ΔP.A. value of targets in each bin. The step-like feature at $\approx 0\rlap{.}''9$ is discussed in Section 6.1.

objects and should be interpreted with caution. We also observe visual consistency between the separation at which ADI begins outperforming Super-RDI and the separation corresponding to a 1 FWHM rotation for the median ΔP.A. value of targets in each bin in Figure 7.

Our results indicate that ADI is better suited for companion detection at small angular separations for studies focusing on a limited number of systems where greater scheduling flexibility can allow larger P.A. rotations to be accrued for similar integration times. However, for large surveys, such as the young M-star survey, the necessity to balance the number of targets observed with limited telescope time availability and scheduling constraints may require an RDI-focused design. In such cases, the Super-RDI framework can help improve the sensitivity of RDI at small angular separations by leveraging a large reference PSF library.

6.3. Dependence on Stellar Fluxes

We investigate the performance of Super-RDI as a function of host star flux using the calculated 5σ principal contrast curves. We focus on two bandpasses: (1) the host star's *W1* magnitude ($\lambda_{\mathrm{eff}} = 3.35\,\mu\mathrm{m}$, FWHM $= 0.64\,\mu\mathrm{m}$) as a proxy for the L' band ($\lambda_{\mathrm{eff}} = 3.776\,\mu\mathrm{m}$, FWHM $= 0.70\,\mu\mathrm{m}$) in which observations were made; and (2) the host star's *R* magnitude ($\lambda_{\mathrm{eff}} = 0.64\,\mu\mathrm{m}$, FWHM $= 0.16\,\mu\mathrm{m}$) due to the Keck II AO system wavefront sensor's sensitivity to those wavelengths.

First, the contrast achieved by Super-RDI is plotted as a function of the corresponding host star's *W1* and *R* magnitude for each target in the sample. We choose to plot the contrast achieved at two separations within the range where Super-RDI outperforms ADI (averaged across all targets) for our data set: $0\rlap{.}''2$ and $0\rlap{.}''4$ (left panels; Figure 8). Visual inspection reveals a

trend in the data for both bandpasses and separations which we quantify mathematically by computing slopes using a least squares linear fit (`scipy.optimize.curve_fit`). The uncertainty in the fit is the square root of the variance estimate for the slope parameter. We find negative slopes for all best-fit lines to the data (left panels; Figure 8), indicating that Super-RDI's sensitivity decreases as the host star becomes fainter. This is expected since fainter targets are more susceptible to deviations from the ideal instrument PSF structure due to variability in observing conditions and poorer AO performance. Our results are in agreement with a similar analysis conducted in W. J. Xuan et al. (2018). A closer look at the fits reveals disagreement between the best-fit line and contrast measurements for targets with *W1* magnitudes $\lesssim 6$ mag and *R* magnitudes $\lesssim 9.5$ mag: Super-RDI achieves shallower contrasts than expected from the best-fit line but comparable contrasts to targets with host star magnitudes just greater than the above values. This may indicate that for targets brighter than these host star magnitudes, the Super-RDI's performance plateaus and does not yield additional gains.

Next, the difference in contrast achieved by Super-RDI and ADI is plotted as a function of the corresponding host star's *W1* and *R* magnitude for each target in the sample (right panels, Figure 8). Similar to above, the contrast values at $0\rlap{.}''2$ and $0\rlap{.}''4$ are chosen. Such an analysis enables us to determine if at small angular separations there is a preferred strategy depending on the host star's magnitude. We find that for targets with *W1* magnitudes $\gtrsim 6$ mag and *R* magnitudes $\gtrsim 9.5$ mag in our survey, Super-RDI outperforms ADI in most cases at both separations. Note that the gain for individual targets can be higher than the sample-averaged values presented in Section 6.1. Below these magnitudes, ADI outperforms Super-RDI in most cases at both
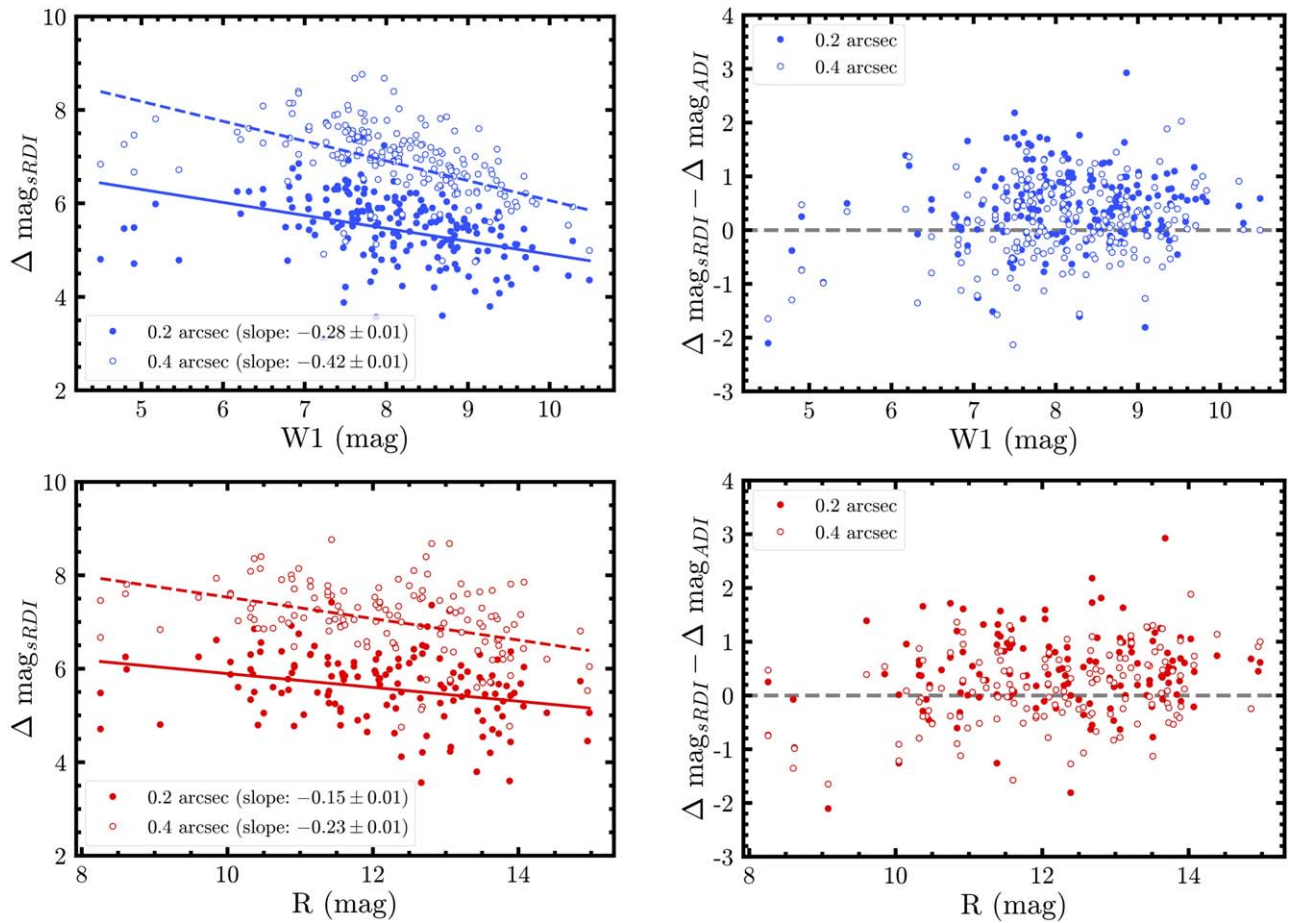
Figure 8. Left column: contrast (in Δmag units) at $0{.}''2$ (solid blue/red circle) and $0{.}''4$ (open blue/red circle) plotted as a function of host star $W1/R$ magnitude for all targets in the sample. The corresponding best-fit lines are plotted as blue/red solid and dashed lines. Negative slopes of the best-fit line indicate decreasing sensitivity for fainter stars. See Section 6.3 for a discussion of the discrepancies in the data with the best-fit line for the brighter targets. Right column: difference in contrast (in Δmag units) at $0{.}''2$ (solid blue/red circle) and $0{.}''4$ (open blue/red circle) achieved by Super-RDI (sRDI) and ADI as a function of host star $W1/R$ magnitude for all targets in the sample. A gray dashed line marks zero difference corresponding to both techniques achieving the same sensitivity level. Super-RDI shows an improvement over ADI for the majority of fainter targets at both separations, while the reverse is true for brighter targets.

separations. This indicates that ADI should be the preferred strategy for bright targets (magnitude ranges above). Super-RDI is the recommended strategy for fainter targets. Note that the data is consistent with zero slope and thus Super-RDI does not offer increasing or decreasing contrast gains as a function of host star magnitude compared to ADI.

7. Point-source Detections

We search for point sources in our uniformly reduced images of the complete young M-star survey data set by visual inspection. To avoid mistaking speckles for companion detections, we consider the evolution of candidate point sources as the number of PCs changes in the image. A speckle is generally variable in nature as the number of PCs changes, whereas a true astrophysical source remains roughly stable in the image. For visually flagged sources, we also compute the S/N to quantify detection significance. The S/N is calculated accounting for small sample statistics as detailed in D. Mawet et al. (2014).

Visual inspection reveals four point-source detections from a total of 157 unique targets. We detect point sources around 2MASS J01225093-2439505, 2MASS J23513366+3127229, 2MASS J06022455-1634494, and LO Peg. Two of the detections are well-characterized substellar companions: 2MASS J01225093-2439505 B (B. P. Bowler et al. 2013) and 2MASS J23513366

+3127229 B (B. P. Bowler et al. 2012). As we will discuss in an upcoming section, the candidate companion around 2MASS J06022455-1634494 is likely a background star based on a common proper motion test. Analysis of the preprocessed coronagraphic images shows that the point source around LO Peg is a speckle. Forward modeling procedures and point-source characteristics are described below.

7.1. Forward Modeling

We perform photometric and astrometric measurements of the point-source detections using negative synthetic companion injection. This technique calibrates measurement biases introduced in the primary subtraction procedures. We apply this method to our observations using VIP's `firstguess` function. First, synthetic companions (normalized unocculted PSF of the target) are injected in a grid near the location of the detection at varying negative-flux values. The reduced χ^2 value, calculated after PSF subtraction of the negative synthetic companion-injected frames, is minimized at the location of injection to obtain a first estimate of the astrometry and photometry of the point source. The estimated parameters are used as inputs to a simplex Nelder–Mead minimization algorithm (J. A. Nelder & R. Mead 1965, implemented with argument `simplex = True`), which provides a more accurate

estimate of the point source's separation, position angle, and flux. We use these values as our forward-modeled parameters. We provide `firstguess` with initial position coordinates for the grid-based minimization step based on visual inspection of the PSF-subtracted image in SAO DS9,[18] choose an annulus width equal to 1.5 FWHM for PCA subtraction, and define the aperture size for flux calculations to be 1 FWHM.

7.2. Uncertainty Analysis

To estimate the uncertainty in our forward-modeled astrometry and photometry, we use synthetic companion injection-recovery tests. First, the point-source detection is removed from the science image cubes by injecting a negative-flux (same as forward-modeled value) synthetic companion at the forward-modeled separation and position angle. This is done to prevent contamination by the point-source detection in subsequent analyses. Next, synthetic companions are injected at the point-source detection's forward-modeled radial separation at eight equally spaced position angles. We forward model each injected synthetic companion following the simplex Nelder–Mead minimization method discussed in Section 7.1. Finally, the error in position angle and separation, and the percentage flux change are recorded for each injected companion. To obtain the total astrometric uncertainty, the standard deviation of the errors is combined with the uncertainties in the distortion solution, centering accuracy of the `QACITS` algorithm (E. Huby et al. 2017), north alignment, and plate scale following K. Franson et al. (2022). To estimate the photometric uncertainty, we combine the speckle noise with the `KLIP` throughput uncertainty. Speckle noise is determined from the standard deviation of the flux integrated within apertures defined in the S/N calculation. The `KLIP` throughput uncertainty is obtained using the standard deviation of the percentage change in injected synthetic companion flux when injection-recovery tests are performed at the separation of the point-source detection at varying position angles.

7.3. Mass Estimates

We can combine the forward-modeled photometry with an age estimate for the host star to obtain the point source's approximate mass (assuming it is a companion) using evolutionary models. Here, we use the COND hot-start evolutionary model grid (I. Baraffe et al. 2003) for our calculations. First, we convert the forward-modeled flux estimate (f_0; optimization is conducted over a 1 FWHM region) of the point source to a contrast value (C) as follows:

$$C = -2.5 \cdot \log_{10}\left(\frac{f_0}{f_{\mathrm{FWHM},\,*}} \cdot \frac{T_{\mathrm{int},\,*} \cdot N_*}{T_{\mathrm{int,\,sci}} \cdot N_{\mathrm{sci}}}\right), \quad (4)$$

where $f_{\mathrm{FWHM},\,*}$ is the aperture-integrated flux of the host star in a 1 FWHM region, $T_{\mathrm{int},\,*}$ is the integration time per coadd, and N_* is the number of coadds, all determined from the host star's unocculted PSF observation. $T_{\mathrm{int,\,sci}}$ is the integration time per coadd and N_{sci} is the number of coadds, both determined from the science observations. Next, we estimate the absolute L' magnitude of the host star ($M_{L',*}$) using its apparent $W1$ magnitude and a parallax measurement. The absolute L' magnitude of the point source (assuming it is at the distance

of the host star) is given by

$$M_{L',\mathrm{PS}} = M_{L',*} + C. \quad (5)$$

Next, we create a 2D linear interpolation function for the COND model grid that maps mass and age inputs to absolute L' magnitude outputs using `scipy.interpolate.interp2d`. We draw an age from the age distribution of the host star and define a set of 10^4 test mass values ranging from $0.0005\,M_\odot$ to $0.1\,M_\odot$. The COND grid is interpolated using the previously calculated function at each test mass for the drawn age to get an absolute L' magnitude ($M_{L',\mathrm{COND}}$). The test mass value at which the squared difference between $M_{L',\mathrm{COND}}$ and $M_{L',\mathrm{PS}}$ is minimized is our estimate for the point source's mass. This complete procedure is repeated for 10^4 different age draws. The mean and standard deviation of the resulting mass estimates provides a range of the possible masses for the point source.

7.4. Known Companions

7.4.1. 2MASS J01225093-2439505

2MASS J01225093-2439505 is an active M3.5V star (B. P. Bowler et al. 2013) with high X-ray luminosity and strong Hα emission (B. Riaz et al. 2006, $\mathrm{EW}_{\mathrm{H}\alpha} = 9.7$ Å). It is a likely AB Doradus young moving group (149^{+51}_{-19} Myr; C. P. M. Bell et al. 2015) member based on a BANYAN-Σ probability of 87.9% (J. Gagné et al. 2018) computed using its parallax, proper motion, and RV (Table 2). B. P. Bowler et al. (2013) discovered an L-type companion 2MASS J01225093-2439505 B ($M_{L'} = 10.4 \pm 0.3$ mag) at a projected separation of $1\farcs452 \pm 0\farcs005$ and position angle (PA) of $216\fdg6 \pm 0\fdg4$ (L' observations with NIRC2 on 2013 January 19). This companion falls in the deuterium burning region of the hot-start evolutionary model grids where tracks overlap, resulting in a dual-valued mass prediction of $12–13\,M_{\mathrm{Jup}}$ or $22–27\,M_{\mathrm{Jup}}$ based on the host star's AB Dor membership.

We observed 2MASS J01225093-2439505 on 2016 October 17 UT and detected the substellar companion (Figure 9) at an S/N of 38. Our astrometric and photometric results for the companion as well as its mass estimate are presented in Table 3. The photometry and mass are consistent with those of B. P. Bowler et al. (2013). We find that the mean separation and PA are discrepant with orbital fits to the compilation of literature astrometry for the companion presented in M. L. Bryan et al. (2020) by ≈8 mas and ≈1°.5, respectively. The magnitude of the discrepancy is consistent with a possible error in star centering behind the vortex coronagraph. This is particularly important to consider for short sequences (such as this observation: 15 minutes on-source integration time) where positional offsets in `QACITS` may not average out as in longer sequences.

To estimate the drift in the star center with respect to the vortex center, we can use the fact that the companion is expected to remain at a fixed position (with random noise) in the individual *derotated* frames. We fit a 2D Gaussian to the companion PSF in each of the sky-subtracted derotated image frames to estimate the source centroid. We find there is an unusually high systematic drift of ≈80 mas along the image x-axis and ≈20 mas along the image y-axis in the position of the companion across the observation sequence. It should be noted that the pointing accuracy and stability provided by `QACITS` are 4.5 mas on average and 2.4 mas rms, respectively (for
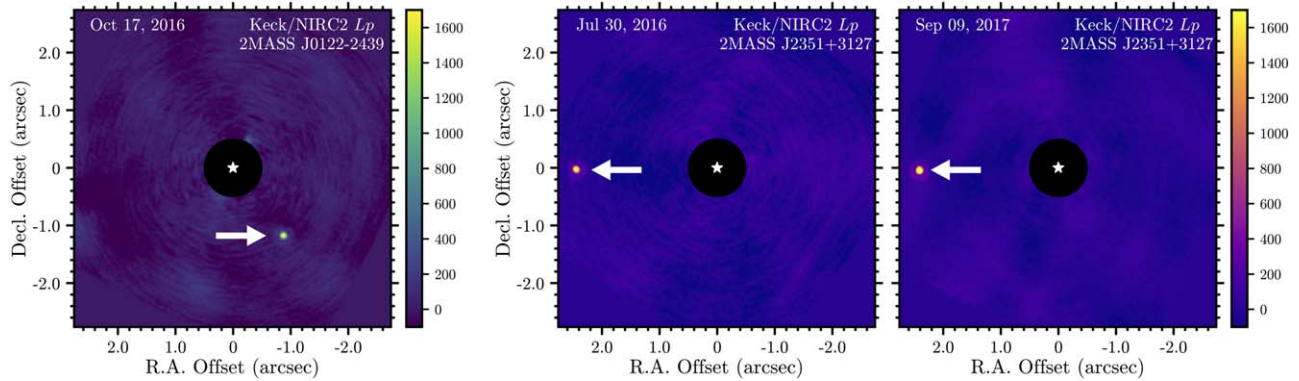
---

[18] https://sites.google.com/cfa.harvard.edu/saoimageds9

Figure 9. Previously known companions detected with Super-RDI in Keck/NIRC2 L' observations. The final PSF-subtracted images of 2MASS J0122-2439 (one epoch; left) and 2MASS J2351+3127 (two epochs; right) are presented above. White arrows point to the detected companions. North is up and east is to the left. All three images and the color bars are depicted in linear scale in analog to digital units and have been smoothed using a Gaussian kernel with a 1.5 pixel standard deviation (40% of the width of the instrumental PSF) to average out high-frequency noise.

Table 2
BANYAN-Σ Inputs for Host Star Membership Analysis

Name	π (mas)	μ_α[a] (mas yr^{-1})	μ_δ (mas yr^{-1})	$v \sin i$ (km s^{-1})	References
2MASS J01225093-2439505	29.6409 ± 0.0273	120.215 ± 0.034	-123.561 ± 0.021	11.4 ± 0.2	(1, 1, 1, 4)
2MASS J23513366+3127229	23.1248 ± 0.0217	106.656 ± 0.021	-87.886 ± 0.016	-13.55 ± 0.07	(1, 1, 1, 2)
2MASS J06022455-1634494	24.8661 ± 0.4167	-8.222 ± 0.368	-67.489 ± 0.365	-8.22 ± 0.04	(1, 1, 1, 2)
LO Peg	41.2912 ± 0.0169	134.654 ± 0.013	-144.889 ± 0.008	-4.44 ± 0.01	(1, 1, 1, 3)

Note.
[a] Proper motion in R.A. includes a factor of cos δ.
References. (1) Gaia Collaboration (2020); (2) P. Fouque et al. (2018); (3) S. Zúñiga-Fernández et al. (2021); (4) L. Malo et al. (2014).

details, refer to E. Huby et al. 2017). The observed drift is thus atypical for vortex observations at Keck and could be due to a combination of relatively poorer seeing ($\approx$0.9) on the night and the target being faint ($R = 13.890$ mag).

We make a conservative estimate of the systematic error in separation and PA by drawing x and y offsets of the star behind the vortex coronagraph from normal distributions with the width equal to the estimated drift and adding them to our forward-modeled values. The standard deviation of the resulting separation and PA distributions provide estimates of the systematic errors. These are added in quadrature with the measurement uncertainty and reported in Table 3.

7.4.2. 2MASS J23513366+3127229

2MASS J23513366+3127229 is a young M2.0V star with a large X-ray flux (B. Riaz et al. 2006; E. Shkolnik et al. 2009). It is an AB Doradus young moving group (149^{+51}_{-19} Myr; C. P. M. Bell et al. 2015) member based on a BANYAN-Σ probability of 99.5% (J. Gagné et al. 2018) computed using its parallax, proper motion, and RV (Table 2). B. P. Bowler et al. (2012) discovered an $\sim$L0 substellar companion 2MASS 23513366+3127229 B at a projected separation of 2386.3 ± 1.5 mas and a PA of $91°.81 \pm 0.°04$ (K' observations with NIRC2 on 2011.871). The companion's mass is $32 \pm 6\ M_{\rm Jup}$ (B. P. Bowler et al. 2012).

We observed 2MASS J23513366+3127229 on 2017 September 9 UT and 2018 July 30 UT and detected the substellar companion (Figure 9) at an S/N of 39 and 47, respectively. Our astrometric and photometric results for the companion as well as its mass estimate are presented in Table 3. The mass is consistent with that presented in

B. P. Bowler et al. (2012). We find that the astrometry of the companion in the 2018 observation epoch is discrepant in separation by $\approx$30 mas with the trend predicted by the compilation of literature astrometry for the companion in B. P. Bowler et al. (2020). Following an identical process to that described in Section 7.4.1, we find a systematic drift of $\approx$50 mas ($\approx$24 mas) along the image x-axis and $\approx$34 mas ($\approx$39 mas) along the image y-axis in the position of the companion across the 2018 (2017) observation sequence. This could be due to the target being faint ($R = 13.105$ mag). The associated systematic errors are added in quadrature with the measurement uncertainty and reported in Table 3.

7.5. New Point-source Detection: 2MASS J06022455-1634494

2MASS J06022455-1634494 is an active M0 star (B. Riaz et al. 2006) with detections of optical and X-ray flares (B. Fuhrmeister & J. H. M. M. Schmitt 2003; W. S. Howard et al. 2019). It is a field object with a BANYAN-Σ probability of 99.9% (J. Gagné et al. 2018) computed using its parallax, proper motion, and RV (Table 2). We observed 2MASS J06022455-1634494 at three difference epochs: 2016.86, 2017.04, and 2017.85. We detect a point source ("CC1") at (145 ± 19 mas, $108°.3 \pm 6°.1$), (179 ± 11 mas, $103°.8 \pm 4°.4$), and (160 ± 18 mas, $91°.3 \pm 3°.9$) at an S/N of $\approx$7 (4σ detection), $\approx$8 (5σ detection), and $\approx$6 (3.9σ detection),[19] respectively, in the Super-RDI reductions (Figure 10) of the three epochs. We followed the procedure

---

[19] The S/N ratio, computed following D. Mawet et al. (2014), is converted to a Gaussian detection significance level for the equivalent false positive probability using the `significance()` function in VIP.

Table 3
Properties of Point-source Detections

Name	UT Date	Angular Separation (ρ) (arcsec)	P.A. (θ) (°)	π (mas)	Physical Separation (au)	Δmag (mag)	M_{Lp} (mag)	Age (Myr)	Inferred Mass ($M_{\rm Jup}$)
2MASS J01225093-2439505 B	2016-10-17	1.458 ± 0.053	217.0 ± 2.7	29.6409 ± 0.0273	49.2 ± 0.4	4.4 ± 0.1	10.8 ± 0.1	149^{+51}_{-19}	18–28
2MASS J23513366+3127229 B	2017-09-09	2.393 ± 0.027	90.6 ± 1.0	23.1248 ± 0.0217	103.5 ± 0.5	4.3 ± 0.1	10.0 ± 0.1	149^{+51}_{-19}	36–42
	2018-07-30	2.427 ± 0.049	90.1 ± 0.9	23.1248 ± 0.0217	105.0 ± 0.5	4.4 ± 0.1	10.0 ± 0.1	149^{+51}_{-19}	36–42
CC1[a]	2016-11-11	0.145 ± 0.019	108.3 ± 6.1	24.8661 ± 0.4167	5.8 ± 0.8	4.8 ± 0.2	9.9 ± 0.2	150–1500[b]	62–86
	2017-01-15	0.179 ± 0.011	103.8 ± 4.4	24.8661 ± 0.4167	7.2 ± 0.4	4.5 ± 0.2	9.5 ± 0.2	150–1500[b]	75–95
	2017-11-06	0.160 ± 0.018	91.3 ± 3.9	24.8661 ± 0.4167	6.4 ± 0.6	4.9 ± 0.2	10.0 ± 0.2	150–1500[b]	60–84

Notes. Parallaxes are obtained from Gaia (Gaia Collaboration 2020). Ages are obtained from C. P. M. Bell et al. (2015) unless noted otherwise.
[a] This point-source detection is a likely background star. In this table, we present the age of the primary star and a mass range for the point source, assuming it is gravitationally bound to 2MASS J06022455-1634494.
[b] 2MASS J06022455-1634494's age is determined based on spectroscopic, activity, and photometric indicators.
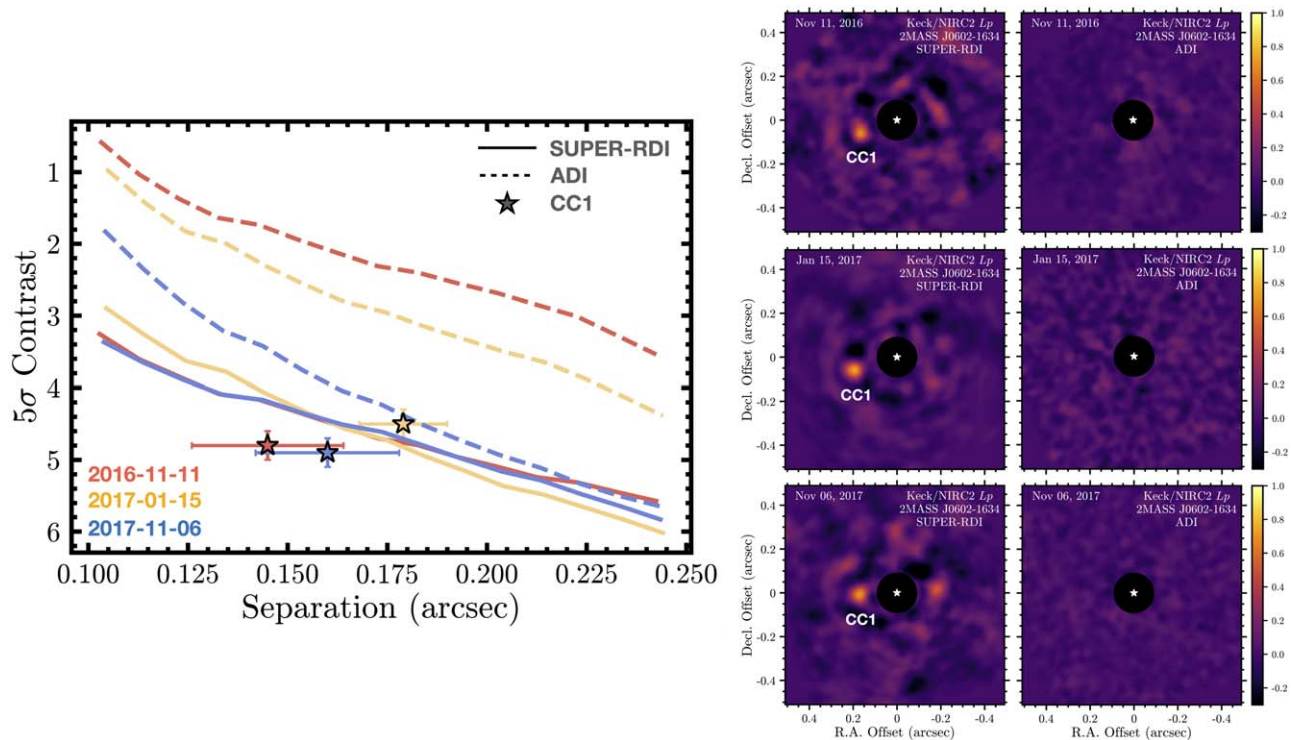
Figure 10. Left: 5σ Super-RDI and ADI contrast curves for 2M0602-1634 for each observation epoch. The point-source detection ("CC1") is marked with a star. Right: final PSF-subtracted images of 2M0602-1634 obtained with Super-RDI and ADI for each observation epoch. North is up and east is to the left. The two images and the color bars are depicted in linear scale in normalized analog to digital units and have been smoothed using a Gaussian kernel with a 1.5 pixel standard deviation (40% of the width of the instrumental PSF) to average out high-frequency noise.

described in Section 7.4.1 to estimate the systematic drift of the star behind the vortex coronagraph, with the difference of performing 2D Gaussian fits to the candidate's PSF in individual derotated KLIP subtracted frames (before temporal averaging) in the sequence. We do not find any significant drift of the star behind the coronagraph ($\lesssim$10 mas). The point source is stable and recovered across all reduction combinations of library size and PCs. This, along with a detection of the candidate across three epochs, significantly reduces the probability of the point source being a speckle. The candidate is detected at contrasts (Δmag) of 4.8 ± 0.2 mag, 4.5 ± 0.2 mag, and 4.9 ± 0.2 mag with an $M_{L'}$ of 9.9 ± 0.2 mag, 9.5 ± 0.2 mag, 10.0 ± 0.2 mag on 2016.86, 2017.04, and 2017.85, respectively. $M_{L'}$ is consistent within uncertainties across the three epochs. The ADI nondetection across all three epochs is not surprising and can be attributed to the small P.A. rotation ($\lesssim$10°) accrued in each of the three data sets. This leads to self-subtraction of the signal.

Host star age analysis: Based on a kinematic analysis with BANYAN-Σ, 2MASS J06022455-1634494 is not associated with any young moving group. We must rely on spectroscopic, activity, and photometric indicators to place constraints on the age of the star.

(1) *Spectroscopic youth indicators:* pre-main-sequence stars undergoing contraction exhibit weaker surface gravity compared to stars on the main sequence. The alkali doublet lines of Na I ($\lambda8183/8195$) and K I ($\lambda7665/7699$) are sensitive to surface gravity and can thus serve as a possible youth indicator for M dwarfs. Similarly, we can use the CaH III molecular absorption band from I. N. Reid et al. (1995) as a spectroscopic youth indicator. E. Gaidos et al. (2014) measure $EW_{K I} =$ 0.970 ± 0.050 Å for 2MASS J06022455-1634494. This suggests an age $\gtrsim$100 Myr (Figure 5; A. R. Riedel et al. 2014) based on the star's $V - K_S = 3.934$ (P. Fouque et al. 2018), though A. R. Riedel et al. (2014) advise caution when interpreting the line at $V - K_s < 5$. B. Riaz et al. (2006) measure a CaH III index $= 0.86$ for 2MASS J06022455-1634494. This index value is slightly smaller (indicating higher surface gravity) than that of M0 dwarfs in the A. A. West et al. (2011) catalog (Figure 14; C. A. Theissen & A. A. West 2014), which largely consists of older field dwarfs.

(2) *Hα emission:* hydrogen emission is a tracer of accretion and magnetic activity and has been associated with stellar age (e.g., O. C. Wilson 1963; A. Skumanich 1972; O. J. Eggen 1990; D. Barrado y Navascués & E. L. Martín 2003). The detection of Hα emission can be used to place an upper limit on the age of a star. Literature measurements of $EW_{H\alpha}$ for 2MASS J06022455-1634494 lie in the range of 1.46–2.2 Å (B. Riaz et al. 2006; E. Gaidos et al. 2014; M. Ansdell et al. 2015). Based on this, the M dwarf Hα age–activity relation of R. Kiman et al. (2021) suggests an age $\lesssim$1.5 Gyr (Figure 6 in the paper). 2MASS J06022455-1634494's $EW_{H\alpha}$ is also similar to those of M0 dwarfs in the Hyades (650 ± 50 Myr; T. D. Brandt & C. X. Huang 2015) and Praesepe (750 ± 100 Myr; S. T. Douglas et al. 2019) open clusters (Figure 5; S. T. Douglas et al. 2014). Thus, the derived upper limit is consistent with the above result as well as the dynamical model-based activity lifetime of 0.8 ± 0.6 Gyr for M0 dwarfs (A. A. West et al. 2008).
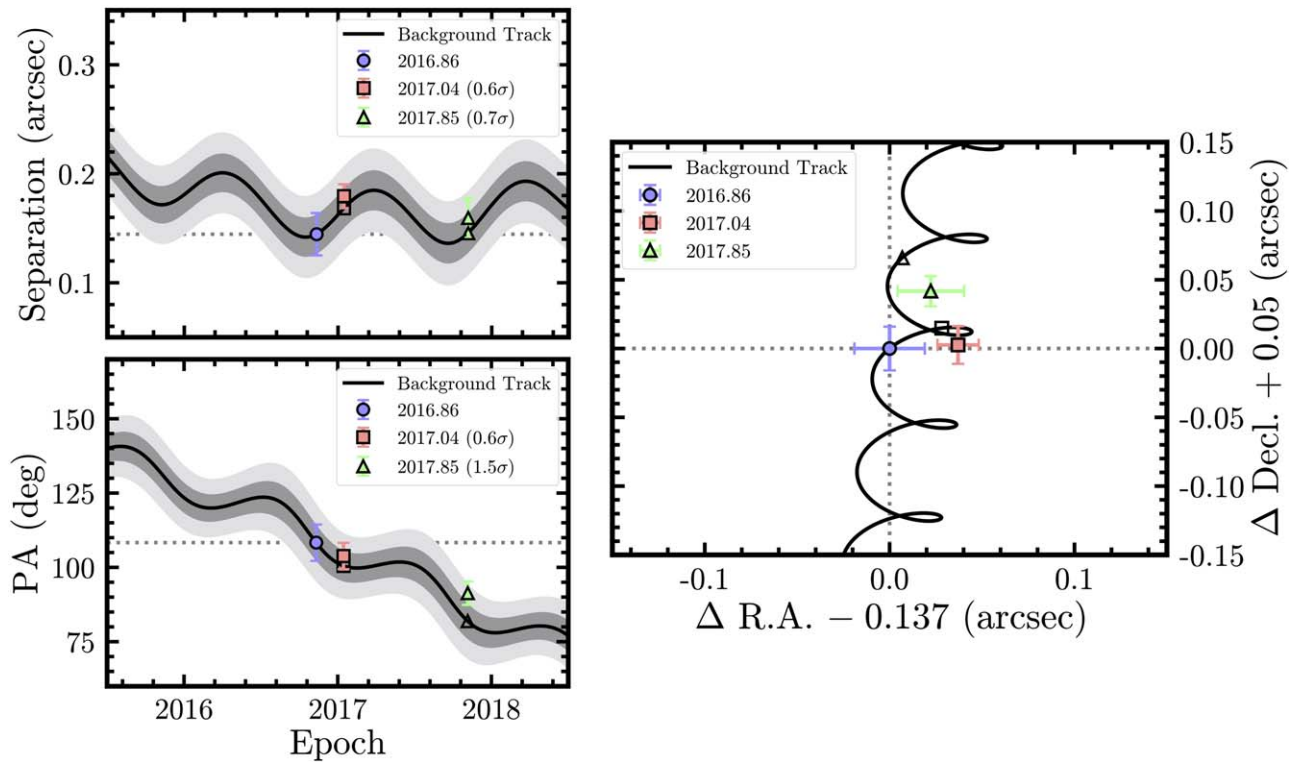
Figure 11. A common proper motion test based on three epochs of relative astrometry between 2MASS J0602-1634 and the candidate companion CC1. The left panels show the predicted relative motion of a stationary background source in separation (top; black solid line) and PA (bottom; black solid line) based on the first epoch of relative astrometry (light purple circles). Gray shaded regions represent 1σ and 2σ uncertainties. The predicted positions at 2017.04 and 2017.85 are plotted as an open square and an open triangle, respectively. The light pink squares and green triangles represent our measurements at the respective epochs. The separation and PA measurements for the 2017.04 and 2017.85 epoch detections are consistent with the predicted background tracks within uncertainties. The right panel shows the same background track comparison but in ΔR.A. and Δdecl. space instead of separation and PA.

(3) *X-ray and UV emission*: B. Riaz et al. (2006) derive the ratio of the X-ray luminosity (from ROSAT) to the bolometric luminosity for 2MASS J06022455-1634494 $\log(L_X/L_{bol}) = -3.28$. Based on Figure 6 in T. Preibisch & E. D. Feigelson (2005), the above value is higher than those measured for Orion (ONC), NGC 2264, and Chamaeleon members in their sample. This would suggest an age $\lesssim 10$ Myr, which contradicts our Hα emission-based analysis. The contradiction is resolved by noting that M. Ansdell et al. (2015) flag 2MASS J06022455-1634494 as a near-ultraviolet (NUV) detection for reasons other than stellar youth. An early M dwarf in a binary system with an unresolved late M dwarf can appear NUV luminous due to the persistent activity of the late M dwarf. The system appears as a single early M dwarf because the early M dwarf dominates the continuum emission. M. Ansdell et al. (2015) test for this configuration by computing the difference between the centroid of the source in a white-light image and in a Hα image. The images are obtained from image cubes collected by M. Ansdell et al. (2015) using the Super-Nova Integral Field Spectrograph (G. Aldering et al. 2002; B. Lantz et al. 2004). If the source is a binary, a shift is expected since the unresolved late M dwarf is the source of stronger Hα emission. A shift was observed for 2MASS J06022455-1634494 and thus implies that the UV and X-ray measurements are unreliable for our age estimation purposes.

(4) *Color–magnitude diagram*: young, pre-main-sequence M dwarfs are still undergoing contraction and should thus have brighter absolute magnitudes than field-age objects. The Gaia DR3 photometry of 2MASS J06022455-1634494 lines up with the main sequence and agrees with members of AB Doradus (≈ 149 Myr) and older groups (Appendix A in R. Kiman et al. 2021). This suggests a host star age $\gtrsim 150$ Myr.

Synthesizing all of the above information, we adopt an age estimate of 0.150–1.500 Gyr for 2MASS J06022455-1634494. Assuming the point source is a gravitationally bound companion, based on the forward-modeled photometry and the adopted age range, we estimate its mass to be in the range 60–95 M_{Jup} (combining the ranges derived across each of the three epochs). The inferred mass range suggests the point source is either a high-mass brown dwarf or a low-mass star. The properties of CC1 are summarized in Table 3.

Common proper motion test: The available data allows us to test whether the point source's astrometry is consistent with a background source or a gravitationally bound companion. Using the host star's parallax, proper motion, and ICRS coordinates (Tables 1 and 2), we plot the predicted motion of the point source with respect to its first epoch astrometry (2016.86), assuming the stationary background source hypothesis. Figure 11 shows the result. Astrometry at the 2017.04 and 2017.85 epochs is consistent with the predicted background track within measurement uncertainties, indicating that CC1 is likely a background object. However, it could be the case that the orbital motion closely mimics the background track and the
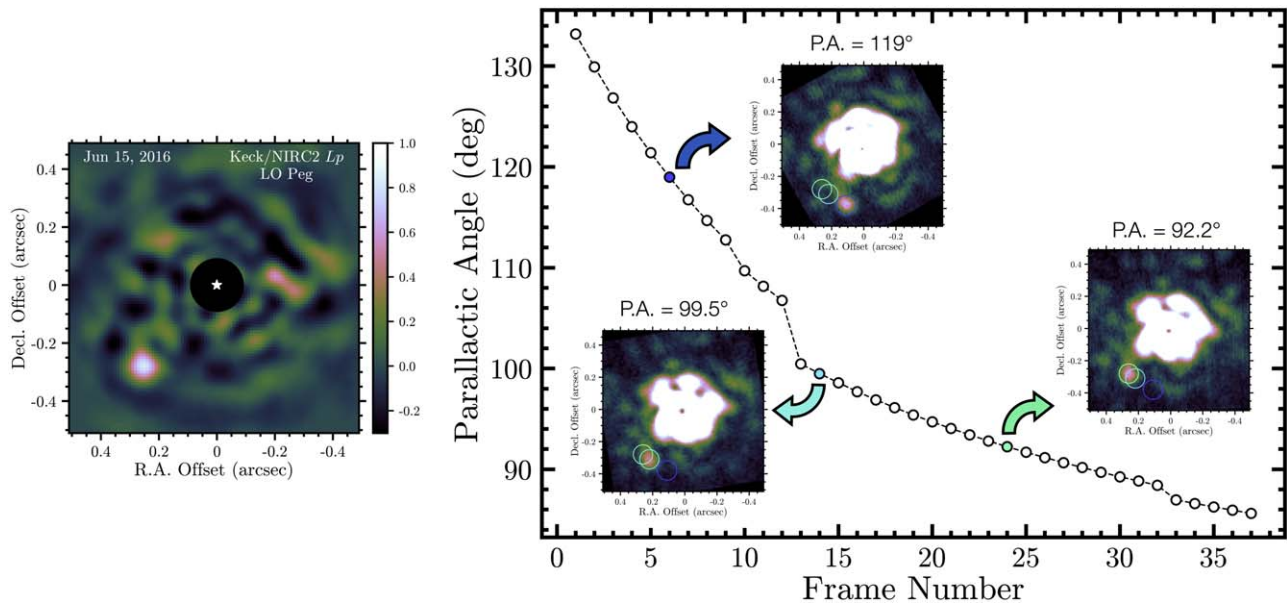
Figure 12. Left: final PSF-subtracted images of LO Peg obtained with Super-RDI. North is up and east is to the left. The image and color bar are depicted in linear scale in normalized analog to digital units and have been smoothed using a Gaussian kernel with a 1.5 pixel standard deviation (40% of the width of the instrumental PSF) to average out high-frequency noise. Right: P.A. of individual frames obtained across the entire observation sequence. Presented as insets are three representative derotated preprocessed frames (north is up and east is to the left) in the sequence showing that the point source in our final PSF-subtracted image rotates across the sequence as expected for a speckle.

differences are of the same order as our astrometric uncertainties. A fourth epoch of astrometry (now with an $\sim$7 yr baseline) can resolve this ambiguity. If bound to the host star, it could potentially explain why the host star appears NUV luminous and exhibits a centroid shift in Hα images for reasons discussed previously.

7.6. Cautionary Case: LO Peg

LO Peg is a young, single (J. R. Barnes et al. 2005; N. Piluso et al. 2008) K3Vke ultrafast rotator (R. O. Gray et al. 2003; S. Karmakar et al. 2016) exhibiting strong flaring activity based on Hα and He I D3 observations (R. D. Jeffries et al. 1994; M. T. Eibe et al. 1999). It is an AB Doradus young moving group (149^{+51}_{-19} Myr; C. P. M. Bell et al. 2015) member (B. Zuckerman & I. Song 2004), with a BANYAN-Σ probability of 99.7% (J. Gagné et al. 2018) computed using its parallax, proper motion, and RV (Table 2).

We observed LO Peg on 2016 June 15 UT and detected a point source at $\approx$362 mas and $\approx$136°.3 at an S/N of $\approx$11 (6.6σ detection) in our Super-RDI reductions (Figure 12, left). The point source is stable and recovered across all reduction combinations of library size and PCs. Based on the PSF-subtracted images, the point source appeared to be a promising substellar candidate (using the forward-modeled photometry and the AB Doradus young moving group age one would find a mass in the range of 13–21 $M_{\rm Jup}$) for follow-up observations.

However, visual inspection of the preprocessed coronagraphic frames revealed a bright source at similar separations. We derotated the preprocessed coronagraphic frames to align them north up based on their P.A.s. True astrophysical sources would remain stationary in the individual derotated frames. We found that the position angle of the bright source changes in the derotated frames across the sequence, providing clear evidence that it is a speckle (Figure 12, right). Typically, we expect the signal of such a speckle to be smeared in the final PSF-

subtracted image due to its changing position angle across the derotated frames. However, this is not seen in our reduced image likely because we acquired a majority of the frames in the second half of the sequence, where the P.A. change was much slower than in the first half (Figure 12, right).

This example shows that even with the availability of a large reference library it can be challenging to fit for and eliminate atypical high spatial frequency speckles in the data. In such cases, there is value in analyzing the preprocessed coronagraphic frames or the individual PSF-subtracted frames before derotation to assess the nature of candidate point sources. The observed lack of smearing of the speckle also suggests that RDI may have a higher false positive rate for vertical angle mode observations when targets are scheduled asymmetrically about transit.

8. Conclusion

This work describes the Super-RDI framework, designed to improve the performance of the RDI strategy when working with large reference libraries. We developed and applied this framework in the context of Keck/NIRC2 high-contrast L' imaging observations with the vortex coronagraph. Our primary results are summarized below:

1. We presented a set of 288 new L' observations (central wavelength of 3.776 μm) of 237 unique targets observed between 2015 December 26 and 2019 January 9. The sample was comprised of targets that were observed independently as part of two survey programs with Keck/NIRC2: the young M-star Survey (195 observations of 157 unique targets) and the Taurus Survey (93 observations of 80 unique targets). The complete set of observations consisted of 7060 image frames.

2. The Super-RDI framework (1) used image similarity metrics to rank and select the best matching reference

stars uniquely for each target; (2) optimized free parameters (metric, library size, number of KLIP PCs) using synthetic companion injection-recovery tests to maximize detection sensitivity; and (3) uniformly processed and conducted a sensitivity analysis of the target sample using the optimized set of reduction parameters.

3. For our data set, synthetic companion injection-recovery tests revealed that frame selection with the MSE metric combined with KLIP-based PSF subtraction using 1000–3000 frames and $\lesssim 500$ PCs yields the highest average S/N for injected synthetic companions.

4. We assembled Super-RDI and ADI principal contrast curves for each target by selecting the deepest 5σ contrast value at each separation across all reduction parameters. The difference between the Super-RDI and ADI contrasts averaged across all targets in our sample (with a typical P. A. rotation of $\sim 10°$) showed that Super-RDI improves upon a widely used implementation of ADI-based PSF subtraction at angular separations $<0.\!''4$. Super-RDI gained as much as 0.25 mag in contrast at $0.\!''25$ and 0.4 mag in contrast at $0.\!''15$. Our results were an improvement over traditional RDI observations with Keck/NIRC2 (W. J. Xuan et al. 2018) in separation space. For best performance with a similar observational design, we recommended complementing Super-RDI with dedicated reference star observations for small angular separation ($\lesssim 0.\!''4$) point-source detection with Keck/NIRC2. These results also showed that ADI is the preferred strategy for wide-separation ($\gtrsim 0.\!''4$) companion searches in the young M-star survey.

5. Based on a comparison of Super-RDI and ADI's performance as a function of P.A. rotation, we found that the separation space over which Super-RDI performs better than ADI shrinks as the P.A. rotation of the observations increases. The results showed that ADI is the preferred strategy at small angular separations for individual observations where larger P.A. rotations (generally $\gtrsim 30°$) can be accumulated.

6. We investigated the performance of Super-RDI as a function of host star $W1$ and R magnitude. Negative slopes are found for best-fit lines to Super-RDI contrast at $0.\!''2$ and $0.\!''4$ as a function of both $W1$ and R magnitude. This indicated decreasing Super-RDI performance for fainter targets in the sample. Additionally, we found that the performance of Super-RDI plateaus for stars brighter than 6 mag in $W1$ and 9.5 mag in R.

7. We analyzed the difference in contrasts (at $0.\!''2$ and $0.\!''4$) achieved by Super-RDI and ADI as a function of host star $W1$ and R magnitude. It was found that Super-RDI shows an improvement over ADI for stars in our sample fainter than 6 mag in $W1$ and 9.5 mag in R at both separations. ADI achieves deeper contrasts at both separations at all other magnitudes.

8. We directly imaged a point source around 2MASS J06022455-1634494 at contrasts of 4.5–5.4 mag (S/N ≈ 5) in three observation epochs at ≈ 163 mas (≈ 6.6 au) and $\approx 101°.4$. 2MASS J06022455-1634494 is a field M0 star with an estimated age of 0.150–1.500 Gyr. A common proper motion test indicated that the point source is likely to be a background object.

9. We provided preprocessed L' coronagraphic frames, associated P.A.s, unocculted PSF frames, Super-RDI reduced images, and detection limits for all observations in the young M-star survey on Zenodo[20] for public access.

Super-RDI is a promising framework for the implementation of RDI with large reference libraries to Keck/NIRC2 high-contrast imaging surveys targeting companions at small angular separations. The technique provides improvements over traditional RDI observations in separation space and mitigates the limitations of ADI such as scheduling difficulty, constrained sky coverage, and self-subtraction at small separations. Combining gains in post-processing with instrumental upgrades in the areas of AO and coronagraphy to improve sensitivity at angular separations $\lesssim 0.\!''5$ will be the key to unlocking new parameter spaces for giant planet demographic studies. The recent direct imaging detections of 8.2 $M_{\rm Jup}$ β Pictoris c at $0.\!''13$ (M. Nowak et al. 2020), 24 $M_{\rm Jup}$ HIP 21152 B at $0.\!''37$ (M. Kuzuhara et al. 2022; K. Franson et al. 2023a), 12.7 $M_{\rm Jup}$ HD 206893 c at $0.\!''11$ (S. Hinkley et al. 2023), 16.1 $M_{\rm Jup}$ HIP 99770 b (T. Currie et al. 2023b) at $0.\!''43$, and 3.2 $M_{\rm Jup}$ AF Lep b at $0.\!''34$ (D. Mesa et al. 2023; K. Franson et al. 2023b; R. J. De Rosa et al. 2023) represent exciting steps in this direction. More broadly, for the nearest and youngest stars, this will facilitate building a larger direct imaging sample of the most typical giant planets at physical separations of 1–10 au for population-level orbital and atmospheric characterization studies.

---

[20] doi:10.5281/zenodo.12747613.

role and reverence that the summit of Maunakea has always had within the indigenous Hawaiian community. We are most fortunate to have the opportunity to conduct observations from this mountain. The computations presented here were conducted in the Resnick High Performance Center, a facility supported by the Resnick Sustainability Institute at the California Institute of Technology. Part of this work was carried out at the Jet Propulsion Laboratory, California Institute of Technology, under contract with NASA. This research has made use of the Keck Observatory Archive (KOA), which is operated by the W. M. Keck Observatory and the NASA Exoplanet Science Institute (NExScI), under contract with the National Aeronautics and Space Administration. This research has made use of the VizieR catalog access tool, CDS, Strasbourg, France (DOI:10.26093/cds/vizier). The original description of the VizieR service was published in F. Ochsenbein et al. (2000). This publication also makes use of data products from the Wide-field Infrared Survey Explorer, which is a joint project of the University of California, Los Angeles, and the Jet Propulsion Laboratory/California Institute of Technology, funded by the National Aeronautics and Space Administration; and the Spanish Virtual Observatory (https://svo.cab.inta-csic.es) project funded by MCIN/AEI/10.13039/501100011033/ through grant PID2020-112949GB-I00.

Facility: Keck II (NIRC2).

Additional Software/Resources: Astropy (Astropy Collaboration et al. 2013, 2018), Matplotlib (J. D. Hunter 2007), NumPy (C. R. Harris et al. 2020), Photutils (L. Bradley et al. 2019), scikit-image (S. van der Walt et al. 2014), VIP (C. A. Gomez Gonzalez et al. 2017; V. Christiaens et al. 2023), and the NASA Astrophysics Data System (ADS).

Appendix A
ADI Optimization for Young M-star Survey Targets

The ADI reduction procedure for our young M-star survey sample is described in Section 5. For the 101×101 pixel frame size reductions with a 1 FWHM central mask (most relevant for our comparisons with Super-RDI), we conducted both full-frame and annular PCA-KLIP reductions for different numbers of PCs. For annular PCA-KLIP reduction, we additionally employed a rotation gap criterion. Due to the low P.A. rotation of our data set, the 0.1, 0.5, 1, and 2 FWHM rotation gap criterion could only be applied for 121, 4, 2, and 1 observations (out of 195), respectively, in our sample without excluding all available frames. It is also important to note that the results presented here are specific to our sample and cannot be broadly generalized to other ADI data sets, for example, those with larger P.A. rotation.

We compare the contrast achieved by annular PCA-KLIP reductions without a rotation gap criterion and those with a rotation gap criterion of 0.1 FWHM (left panel of Figure A1). Contrast curves generated with varying PCs in each case are combined together by selecting the deepest contrast value at each separation to generate a "principal" contrast curve for the two reductions of each target. The reduction strategy that achieves deeper contrast varies significantly between individual targets as well as separation from the host star. Generally, we find that annular PCA-KLIP with a rotation gap criterion of 0.1 FWHM provides better performance at separations $\gtrsim 0\rlap{.}''25$ for our data set. We also compare the contrast achieved by full-frame and annular PCA-KLIP reductions (right panel of Figure A1). Contrast curves generated with varying PCs (for full-frame and annular reductions) and with varying values of rotation gap criteria (for annular reductions) are combined together by selecting the deepest contrast value at each separation to generate a "principal" contrast curve for the full-frame and annular PCA-KLIP reduction of each target. Based on the principal contrast curves, the reduction strategy that achieves deeper contrast depends on the individual target. However, for the majority of targets in our sample, we find that full-frame PCA-KLIP is preferred over annular PCA-KLIP.
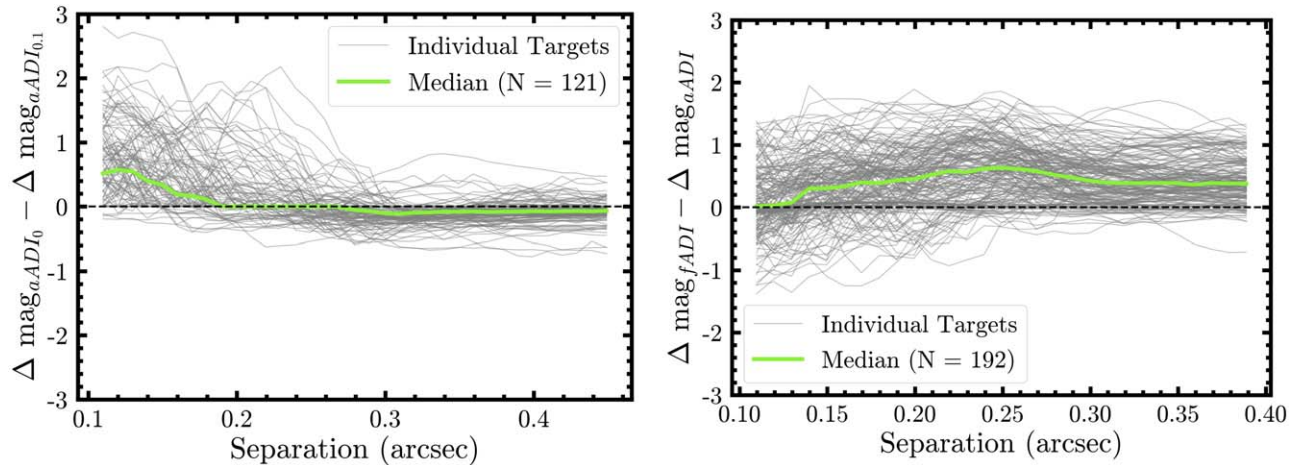
Figure A1. Left: difference in contrast (units of Δmag) achieved between annular ADI with a rotation gap criterion of 0.1 FWHM ($aADI_{0.1}$) and annular ADI with no rotation gap criterion ($aADI_0$) as a function of separation (units of arcseconds). A black dashed line marks zero difference and corresponds to both strategies achieving the same sensitivity level. Gray curves correspond to individual targets in the sample and the green curve corresponds to the median computed across all targets. Right: same as the left panel but presenting the difference in contrast achieved between full-frame ADI ($fADI$) and annular ADI ($aADI$). The best-performing strategy varies depending on the individual target.

Appendix B
Table of Optimal Contrast Curves

We provide optimal contrasts at select separations for targets in the young M-star survey in Table B1.

Table B1
Keck/NIRC2 L' Optimal Contrast for Young M-star Survey Targets at Select Separations

Name	UT Date	0″1 (Δmag)	0″2 (Δmag)	0″3 (Δmag)	0″4 (Δmag)	0″5 (Δmag)	0″6 (Δmag)	0″7 (Δmag)	0″8 (Δmag)	0″9 (Δmag)	1″0 (Δmag)	1″25 (Δmag)	1″5 (Δmag)	1″75 (Δmag)	2″0 (Δmag)	2″25 (Δmag)	2″5 (Δmag)
2MASS J00243202-2522528	2016-07-18	4.14	5.40	6.05	6.77	7.25	7.01	6.90	7.33	7.28	7.49	7.87	7.99	7.93	8.01	8.06	8.08
2MASS J00275023-3233060	2016-11-05	4.50	5.83	7.20	7.29	7.52	7.70	8.05	8.28	8.59	8.60	8.76	8.89	9.08	9.17	9.22	9.22
2MASS J00275023-3233060	2016-09-11	3.49	4.89	6.57	6.77	6.57	6.71	7.49	7.75	7.86	7.67	8.08	8.06	8.32	8.27	8.19	8.57
GJ 2006B	2016-09-12	4.25	5.90	6.77	7.01	7.16	7.41	7.84	7.89	7.81	7.74	7.88	7.99	8.01	8.19	8.20	8.24
2MASS J00551501+3015156	2016-09-23	3.98	5.50	6.64	7.00	6.93	7.28	7.42	7.36	7.40	7.43	7.53	7.53	7.54	7.74	7.81	7.80
2MASS J00551501+3015156	2016-09-11	3.83	5.93	6.19	6.02	6.03	6.37	6.87	6.87	7.06	7.23	7.32	7.43	7.60	7.66	7.68	7.60
2MASS J01123504+1703557	2016-10-17	3.24	4.98	5.98	6.32	6.75	7.12	7.12	7.26	7.35	7.38	7.43	7.46	7.51	7.59	7.66	7.73
2MASS J01220441-3337036	2015-12-27	3.51	5.61	6.84	7.03	7.14	7.39	7.84	8.05	8.37	8.44	8.69	8.80	8.91	8.94	9.02	8.99
2MASS J01225093-2439505	2016-10-17	3.44	5.42	6.03	6.23	6.67	6.69	6.89	7.23	7.33	7.16	7.58	6.93	7.63	7.76	7.70	7.77
2MASS J01225093-2439505	2018-07-30	2.94	4.43	5.42	5.85	5.79	5.89	5.94	5.95	5.96	6.02	6.05	5.81	6.20	6.15	6.13	6.35
2MASS J01351393-0712517	2016-09-12	4.80	7.24	8.21	8.68	8.79	9.12	9.05	8.98	9.00	8.97	9.16	9.22	9.33	9.37	9.40	9.46
2MASS J01354915-0753470	2017-09-09	3.27	5.45	6.45	6.55	6.44	6.89	6.74	7.00	7.06	7.04	7.14	7.21	7.26	7.35	7.35	7.34
2MASS J01365516-0647379	2016-11-05	4.32	6.20	7.10	7.06	7.40	7.60	7.91	8.13	8.16	8.27	8.30	8.27	8.27	8.46	8.56	8.55
2MASS J01365516-0647379	2016-09-11	3.44	5.16	6.38	6.76	6.57	6.69	7.25	7.50	7.63	7.55	7.80	7.59	7.81	7.91	7.78	8.05
2MASS J02001277-0840516	2015-12-27	4.20	6.07	7.31	7.92	8.24	8.42	8.35	8.52	8.72	8.68	8.77	8.93	8.99	9.03	8.94	8.98
[SLS2012] PYC J02017+0117N	2016-09-12	4.36	6.90	8.01	8.02	8.23	8.56	8.63	8.75	8.83	8.84	9.02	9.00	9.14	9.11	9.13	9.12
[SLS2012] PYC J02017+0117S	2016-09-23	3.88	5.52	6.54	7.28	7.66	7.80	8.03	8.34	8.45	8.46	8.57	8.66	8.73	8.84	8.76	8.85
[SLS2012] PYC J02017+0117S	2016-09-11	4.84	5.79	7.14	7.50	7.13	7.19	7.78	8.16	8.08	8.11	8.28	8.20	8.37	8.38	8.35	8.33
2MASS J02070176-4406380	2016-11-05	3.94	4.98	6.24	6.38	6.60	7.13	7.37	7.58	7.70	7.78	8.09	8.27	8.48	8.56	8.54	8.59
2MASS J02070786-1810077	2017-01-15	3.77	5.12	6.24	6.03	6.82	6.87	7.07	7.31	7.33	7.46	7.51	7.57	7.61	7.60	7.60	7.69
2MASS J02175601+1225266	2016-11-05	3.67	5.67	6.60	7.15	7.42	7.61	7.64	7.93	7.86	7.97	8.03	8.02	7.93	8.04	8.14	8.12

Name	UT Date	0″.1 (Δmag)	0″.2 (Δmag)	0″.3 (Δmag)	0″.4 (Δmag)	0″.5 (Δmag)	0″.6 (Δmag)	0″.7 (Δmag)	0″.8 (Δmag)	0″.9 (Δmag)	1″.0 (Δmag)	1″.25 (Δmag)	1″.5 (Δmag)	1″.75 (Δmag)	2″.0 (Δmag)	2″.25 (Δmag)	2″.5 (Δmag)
2MASS J02304623-4343493	2016-09-12	3.80	5.84	7.07	7.05	7.08	7.21	7.90	7.81	8.11	8.09	8.33	8.21	8.50	8.58	8.66	8.66
2MASS J02505959-3409050	2017-09-09	2.82	4.86	5.62	6.23	6.15	6.47	6.74	6.89	7.07	7.12	7.23	7.25	7.41	7.45	7.43	7.60
2MASS J02590322-4232450	2017-01-15	2.82	4.45	5.06	5.53	5.38	5.57	5.74	5.74	6.09	6.13	6.29	6.42	6.61	6.65	6.69	6.80
2MASS J03025156-1911496	2016-11-11	3.12	4.86	5.65	5.98	6.05	6.22	6.31	6.55	6.54	6.72	7.11	7.36	7.39	7.55	7.55	7.72
2MASS J03093877-3014352	2015-12-26	3.03	4.36	4.91	5.00	5.72	5.94	6.12	6.26	6.24	6.52	6.70	6.80	6.95	6.95	6.98	7.01
HIP 14807	2017-11-06	4.30	5.56	7.72	8.13	8.57	8.72	8.99	9.16	9.18	9.29	9.34	9.46	9.48	9.43	9.59	9.62
HIP 14807	2016-11-11	3.11	5.67	7.01	7.55	7.42	7.97	7.99	8.28	8.38	8.46	8.45	8.82	8.90	9.09	9.11	9.13
HIP 14807	2016-09-11	4.16	5.88	7.56	8.00	7.74	8.12	8.67	9.02	8.88	9.01	9.09	9.11	9.27	9.25	9.19	9.24
2MASS J03190864-3507002	2016-11-23	4.14	5.78	6.89	7.49	7.32	7.45	8.00	7.95	8.05	8.15	8.46	8.47	8.72	8.78	8.83	8.88
2MASS J03214689-0640242	2016-09-12	4.78	6.75	8.48	8.75	9.32	9.59	9.93	9.97	9.80	9.90	10.19	10.02	10.29	10.36	10.25	10.43
2MASS J03282609-0537361	2017-01-15	3.97	5.44	6.84	6.84	7.30	7.55	7.68	7.76	7.83	7.93	7.98	7.91	7.98	8.11	8.20	8.26
HD 21845B	2015-12-27	3.23	5.56	6.75	7.38	7.63	7.58	8.06	8.31	8.45	8.47	8.61	8.63	8.67	8.68	8.74	8.81
TYC 1252-798-1	2016-09-12	5.37	7.23	8.08	8.40	8.61	8.82	8.77	8.94	8.77	9.02	9.02	8.99	8.94	9.10	9.00	9.01
HIP 17695	2017-01-15	4.45	6.81	8.61	8.43	9.32	9.54	9.77	9.78	9.98	10.03	10.20	10.21	10.30	10.34	10.46	10.54
WISE J035223.52-282619.6	2017-09-09	2.83	4.59	5.74	6.24	6.46	6.98	7.26	7.34	7.27	7.51	7.78	7.89	7.96	7.87	7.91	8.04
2MASS J04000395-2902280	2015-12-26	4.03	5.88	6.99	7.46	7.46	7.83	8.15	8.39	8.52	8.62	8.91	8.95	9.08	9.02	9.07	9.10
2MASS J04021648-1521297	2015-12-26	4.47	6.47	7.86	7.93	8.48	8.63	8.87	8.95	9.12	9.11	9.21	9.27	9.34	9.42	9.35	9.51
2MASS J04093930-2648489	2017-11-06	4.03	5.92	6.79	7.10	6.95	7.30	8.01	8.10	8.05	8.29	8.38	8.59	8.63	8.74	8.74	8.80
2MASS J04141730-0906544	2017-09-09	2.89	4.20	4.99	5.71	5.94	6.42	6.72	7.07	6.97	6.83	7.04	7.29	7.33	7.45	7.53	7.73
G7-34	2016-11-11	5.06	6.20	7.74	8.04	8.50	8.55	8.58	8.80	8.93	8.93	9.04	9.16	9.18	9.33	9.23	9.23
2MASS J04244260-0647313	2016-09-12	3.93	5.85	7.40	7.66	7.63	7.90	8.09	8.52	8.43	8.50	8.69	8.72	8.77	8.75	8.73	8.82
2MASS J04353618-2527347	2017-11-06	4.01	5.76	7.58	8.09	8.34	8.69	9.01	9.21	9.30	9.35	9.57	9.60	9.66	9.77	9.87	9.92
2MASS J04353618-2527347	2017-01-15	4.59	6.33	7.30	7.72	8.15	8.48	9.13	9.18	9.37	9.47	9.58	9.65	9.84	9.87	9.85	9.88
[WKS96] 42	2016-11-11	4.02	5.90	6.83	6.91	6.90	6.91	7.12	7.13	6.86	6.83	7.02	6.67	6.72	6.65	6.49	6.57
2MASS J04435686+3723033	2015-12-26	4.38	5.90	6.63	7.21	7.56	7.54	7.89	7.96	8.07	8.19	8.23	8.29	8.36	8.41	8.39	8.46
2MASS J04522441-1649219	2016-01-25	3.57	5.49	6.69	7.27	8.17	8.43	8.92	9.13	9.26	9.35	9.63	9.57	9.79	9.84	9.30	9.89
V1005 Ori	2016-11-11	4.41	6.25	7.43	7.53	7.90	8.71	9.30	9.71	9.76	9.75	10.16	10.10	10.16	10.30	10.39	10.31
[SLS2012] PYC J05019+0108	2017-11-06	4.30	6.60	8.23	8.64	8.92	8.99	9.29	9.39	9.51	9.51	9.75	9.73	9.84	9.92	9.85	9.95

31

Table B1
(Continued)

Name	UT Date	0″1 (Δmag)	0″2 (Δmag)	0″3 (Δmag)	0″4 (Δmag)	0″5 (Δmag)	0″6 (Δmag)	0″7 (Δmag)	0″8 (Δmag)	0″9 (Δmag)	1″0 (Δmag)	1″25 (Δmag)	1″5 (Δmag)	1″75 (Δmag)	2″0 (Δmag)	2″25 (Δmag)	2″5 (Δmag)
[SLS2012] PYC J05019+0108	2017-01-15	4.79	6.42	7.98	8.33	8.91	9.10	9.21	9.31	9.37	9.49	9.52	9.66	9.72	9.85	9.77	9.80
2MASS J05195695-1124440	2015-12-26	3.82	5.30	6.09	6.73	6.84	6.94	6.98	7.23	7.30	7.31	7.51	7.56	7.64	7.69	7.72	7.78
2MASS J05234246+0651581	2016-11-11	3.96	5.54	6.18	6.54	6.77	6.75	6.93	7.07	7.22	7.17	7.40	7.37	7.65	7.76	7.64	7.70
2MASS J05241317-2104427	2017-01-15	3.79	5.63	6.70	6.81	6.97	7.05	7.24	7.39	7.61	7.57	7.80	7.98	8.04	7.92	7.96	8.04
WISE J053100.27+231218.3	2016-11-23	1.91	4.27	5.59	5.84	6.10	6.02	6.10	6.09	5.41	5.38	5.53	5.50	5.53	5.67	5.65	5.81
2MASS J05335981-0221325	2016-11-11	4.29	6.20	6.99	7.37	7.74	7.79	8.01	7.92	8.01	8.15	8.73	8.62	8.73	8.76	8.85	8.91
2MASS J05395494-1307598	2016-11-11	3.38	5.12	5.78	5.93	5.90	5.92	5.95	5.96	5.50	5.87	6.46	6.56	6.85	6.89	7.14	7.31
2MASS J05432676-3025129	2017-11-06	3.42	5.08	5.63	6.31	6.31	6.34	6.62	6.98	7.07	7.11	7.23	7.43	7.37	7.57	7.66	7.61
2MASS J06012186-1937547	2017-11-06	3.77	5.20	5.64	5.93	6.45	6.52	6.85	6.93	7.08	7.10	7.30	7.36	7.47	7.52	7.48	7.58
2MASS J06022455-1634494	2017-11-06	3.38	5.15	6.34	6.91	7.12	7.42	7.89	8.07	8.15	8.30	8.50	8.57	8.60	8.74	8.73	8.91
2MASS J06022455-1634494	2016-11-11	3.75	5.08	6.45	6.88	6.78	7.02	7.21	7.37	7.14	6.98	6.80	6.70	7.10	7.22	7.44	7.61
2MASS J06022455-1634494	2017-01-15	3.49	4.82	7.13	7.20	7.57	7.97	8.12	8.41	8.54	8.69	8.80	8.84	8.84	8.79	8.75	8.87
2MASS J06373215-2823125	2016-01-25	3.35	4.84	6.23	6.32	6.99	7.14	7.37	7.37	7.63	7.71	7.74	7.91	7.89	7.93	7.96	7.97
2MASS J06380031-4056011	2015-12-26	3.21	4.27	5.34	6.04	5.77	5.97	6.15	6.07	6.19	6.25	6.62	6.71	6.78	6.79	6.98	7.09
2MASS J06511418-4037510	2015-12-27	2.67	4.63	5.13	5.08	5.52	5.33	5.85	6.32	6.81	6.68	7.31	7.55	7.78	7.86	7.99	8.02
2MASS J07140101-1945332	2016-03-25	2.85	4.61	5.57	5.98	6.13	6.31	6.50	6.70	6.73	6.80	6.90	7.01	7.22	7.20	7.28	7.41
2MASS J07285117-3015527	2016-11-24	2.66	4.54	5.36	5.70	5.69	6.05	5.95	6.06	6.02	6.18	6.25	6.34	6.49	6.40	6.34	6.46
2MASS J07285117-3015527	2017-11-06	4.21	5.67	7.39	8.04	8.18	8.43	8.93	9.12	9.19	9.11	9.28	9.33	9.49	9.55	9.39	9.56
2MASS J07310129+4600266	2015-12-26	3.75	5.63	6.85	7.21	7.54	7.81	7.95	7.97	8.03	7.90	8.12	8.28	8.26	8.38	8.36	8.42
2MASS J07504838-2931126	2015-12-26	4.18	5.63	6.64	6.71	7.06	7.30	7.49	7.75	7.75	7.79	7.97	8.09	8.24	8.23	8.23	8.25
2MASS J09123564-1517033	2017-01-14	4.36	6.14	6.98	7.05	7.34	7.57	7.83	8.10	8.25	8.37	8.50	8.58	8.47	8.52	8.50	8.42
2MASS J09123564-1517033	2015-12-26	3.93	6.05	6.92	7.56	7.84	8.28	8.38	8.60	8.43	8.58	8.83	8.75	9.00	8.95	9.02	9.02
2MASS J09353126-2802552	2017-01-14	4.60	6.32	7.16	7.43	7.66	7.88	8.01	8.33	8.25	8.33	8.67	8.73	8.88	8.99	9.13	9.13

Name	UT Date	$0\rlap{.}''1$ (Δmag)	$0\rlap{.}''2$ (Δmag)	$0\rlap{.}''3$ (Δmag)	$0\rlap{.}''4$ (Δmag)	$0\rlap{.}''5$ (Δmag)	$0\rlap{.}''6$ (Δmag)	$0\rlap{.}''7$ (Δmag)	$0\rlap{.}''8$ (Δmag)	$0\rlap{.}''9$ (Δmag)	$1\rlap{.}''0$ (Δmag)	$1\rlap{.}''25$ (Δmag)	$1\rlap{.}''5$ (Δmag)	$1\rlap{.}''75$ (Δmag)	$2\rlap{.}''0$ (Δmag)	$2\rlap{.}''25$ (Δmag)	$2\rlap{.}''5$ (Δmag)
2MASS J09353126-2802552	2015-12-26	4.10	5.90	6.60	7.28	7.78	7.95	8.30	8.52	8.58	8.68	8.88	8.94	8.96	9.03	9.05	9.12
2MASS J09445422-1220544	2017-01-14	4.33	6.30	7.53	7.64	8.18	8.36	8.78	9.02	9.21	9.15	9.45	9.44	9.49	9.49	9.49	9.48
2MASS J09445422-1220544	2015-12-27	3.89	5.81	6.64	7.00	7.56	7.69	7.89	8.11	8.67	8.87	8.97	8.94	9.11	9.11	9.11	9.20
2MASS J10120908-3124451	2016-11-23	2.56	4.32	5.27	5.67	5.30	5.49	5.49	5.46	5.73	6.05	6.00	7.06	7.36	7.62	7.67	7.85
2MASS J10121768-0344441	2017-01-14	4.31	6.21	8.50	8.23	9.55	9.87	10.29	10.63	11.09	11.28	11.57	11.82	11.95	12.12	12.05	12.05
2MASS J10121768-0344441	2016-11-22	4.01	4.71	5.89	6.66	7.12	7.40	8.48	8.92	9.20	9.65	10.34	10.54	10.90	10.94	11.14	11.25
2MASS J10182870-3150029	2015-12-26	4.22	6.25	7.72	8.22	8.38	8.17	8.31	8.63	8.70	8.78	8.96	9.02	8.96	8.84	9.00	9.03
2MASS J10252092-4241539	2016-03-25	4.03	4.62	6.14	6.52	7.15	7.35	7.42	7.62	7.73	7.58	7.96	7.75	8.15	7.99	8.01	8.15
2MASS J10260210-4105537	2017-01-14	4.09	5.58	6.43	6.96	7.11	7.38	7.65	7.82	7.98	8.06	8.34	8.41	8.56	8.57	8.55	8.64
2MASS J10260210-4105537	2016-11-22	3.77	5.30	6.38	6.89	6.60	6.40	7.12	7.34	7.26	7.11	7.56	7.38	7.62	7.56	7.57	7.75
BD+01 2447	2015-12-27	5.41	6.96	8.05	8.79	9.32	9.53	9.99	10.12	10.44	10.76	11.23	11.37	11.49	11.63	11.55	11.53
2MASS J10423011-3340162	2016-03-25	4.47	6.08	7.62	7.58	8.78	8.94	9.32	9.59	9.63	10.02	10.06	10.17	10.19	10.23	10.21	10.27
TWA 1	2016-01-25	4.67	5.61	6.81	6.86	7.63	7.83	8.15	8.50	8.62	8.75	9.05	9.19	9.25	9.32	9.46	9.40
2MASS J11110358-3134591	2017-05-10	2.63	4.43	5.90	6.50	6.47	6.80	6.91	7.14	7.22	7.42	7.62	7.58	7.67	7.90	7.80	7.92
2MASS J11200609-1029468	2016-05-27	4.18	5.91	7.97	9.04	9.22	9.40	9.69	9.90	10.13	10.21	10.32	10.35	10.29	10.29	10.23	10.39
2MASS J11210549-3845163	2017-01-14	4.33	5.68	6.64	7.13	7.38	7.18	7.80	7.80	8.06	8.21	8.39	8.48	8.55	8.68	8.74	8.90
TWA 8B	2016-03-25	3.56	5.46	6.53	7.13	7.45	7.47	7.87	7.85	8.06	7.99	8.21	8.25	8.34	8.39	8.55	8.52
TWA 8A	2016-03-25	3.93	6.33	7.43	7.88	8.45	8.50	9.01	8.99	9.18	9.29	9.44	9.50	9.60	9.69	9.71	9.72
TWA 33	2017-01-15	4.00	5.73	6.94	7.06	7.80	8.03	8.17	8.31	8.32	8.31	8.40	8.43	8.64	8.64	8.50	8.64
2MASS J11431742+1123126	2017-05-10	3.31	4.98	6.18	6.74	7.02	7.23	7.42	7.48	7.53	7.69	7.70	7.82	7.88	7.85	7.94	8.00
TWA 9A	2017-01-14	3.95	6.04	6.83	7.13	7.20	7.37	7.92	8.03	8.31	8.39	8.70	8.83	8.85	8.87	8.91	8.91
2MASS J12000160-1731308	2017-01-15	4.30	5.94	7.63	7.47	8.37	8.42	8.63	8.75	8.75	8.80	8.88	8.88	8.98	9.01	9.10	9.15
2MASS J12120849+1248050	2016-06-09	2.83	5.22	6.65	7.00	7.29	7.57	7.73	7.66	7.65	7.85	7.86	7.95	8.03	8.07	8.13	8.12
2MASS J12151838-0237283	2016-05-27	4.82	6.31	7.79	8.28	8.58	8.73	8.84	8.91	9.08	9.05	9.17	9.38	9.35	9.38	9.33	9.46
2MASS J12153072-3948426	2016-04-13	4.49	6.07	7.12	7.71	8.18	8.20	8.53	8.80	8.73	9.03	9.15	9.16	9.39	9.43	9.45	9.49
2MASS J12350424-4136385	2016-04-13	4.45	5.58	6.66	7.46	7.57	7.93	8.03	8.14	8.21	8.12	8.42	8.49	8.61	8.64	8.61	8.72
TWA 11C	2017-01-14	3.82	5.41	6.38	6.44	6.92	7.03	7.29	7.51	7.51	7.58	7.70	7.83	7.79	7.82	7.81	7.86

Name	UT Date	0″1 (Δmag)	0″2 (Δmag)	0″3 (Δmag)	0″4 (Δmag)	0″5 (Δmag)	0″6 (Δmag)	0″7 (Δmag)	0″8 (Δmag)	0″9 (Δmag)	1″0 (Δmag)	1″25 (Δmag)	1″5 (Δmag)	1″75 (Δmag)	2″0 (Δmag)	2″25 (Δmag)	2″5 (Δmag)
TWA 11B	2017-05-11	3.62	4.78	6.32	6.72	7.33	7.37	7.74	8.18	8.21	8.34	8.56	8.65	8.68	8.76	8.75	8.81
2MASS J12374082 +3450555	2016-01-25	3.65	5.84	7.12	7.09	7.79	7.76	8.09	8.22	8.15	8.25	8.44	8.45	8.52	8.64	8.67	8.73
2MASS J13213722 -4421518	2017-01-14	4.16	5.22	6.01	6.53	6.38	6.52	6.85	6.76	6.87	6.89	7.22	7.38	7.43	7.71	7.73	7.73
2MASS J13283294 -3654233	2016-03-25	4.52	4.77	5.73	6.19	6.68	6.99	7.18	7.46	7.52	7.63	7.66	7.81	8.04	8.06	8.06	8.17
2MASS J13342523 +6956273	2016-01-25	3.59	5.26	6.47	6.73	7.36	7.56	7.63	7.69	7.85	7.93	8.18	8.01	8.30	8.27	8.38	8.41
2MASS J13343188 -4209305	2016-06-09	3.25	4.87	6.81	7.25	7.62	7.93	8.17	8.25	8.37	8.62	8.73	8.84	8.82	8.96	9.07	9.17
2MASS J13382562 -2516466	2016-05-27	4.27	6.05	7.42	7.49	7.62	7.90	8.37	8.48	8.58	8.59	8.93	8.96	9.14	9.16	9.11	9.22
2MASS J13412668 -4341522	2017-05-10	3.26	4.85	5.92	6.21	6.33	6.47	6.68	6.88	6.92	7.06	7.23	7.39	7.47	7.50	7.49	7.61
2MASS J13412668 -4341522	2017-01-15	−0.00	0.08	0.96	0.88	1.50	1.45	1.88	1.71	1.91	2.11	2.25	2.19	2.36	2.44	2.34	2.28
2MASS J13591045 -1950034	2016-06-09	3.85	5.76	8.32	9.24	9.47	9.67	9.78	9.97	10.05	9.81	10.03	9.75	10.08	10.07	10.02	10.14
2MASS J14190331 +6451463	2017-06-13	2.97	5.49	6.24	6.40	6.82	7.11	7.26	7.52	7.59	7.73	7.85	8.02	8.10	8.18	8.18	8.28
2MASS J14252913 -4113323	2017-05-11	3.28	5.25	6.68	7.06	7.53	7.57	7.92	8.43	8.67	8.52	8.91	8.93	9.10	9.27	9.12	9.38
2MASS J15093920 -1332119	2016-03-25	4.00	6.04	7.23	7.85	7.91	8.09	8.21	8.37	8.37	8.51	8.71	8.83	8.95	9.09	9.10	9.12
2MASS J15202415 -3037317	2016-05-26	3.10	5.02	6.29	7.09	7.62	8.03	8.03	8.26	8.34	8.47	8.63	8.56	8.99	8.81	8.81	8.98
2MASS J15443518 +0423075	2016-03-25	3.73	5.46	6.78	6.75	7.26	7.55	7.52	7.77	7.84	7.86	7.98	8.17	8.23	8.30	8.33	8.31
2MASS J15594951 -3628279	2016-03-25	3.65	5.34	6.60	7.09	7.19	7.29	7.66	7.83	7.88	7.94	8.34	8.34	8.53	8.55	8.69	8.70
2MASS J16082845 -0607345	2016-05-27	3.74	5.70	6.74	7.12	7.39	7.57	7.79	7.70	7.87	7.74	7.93	8.02	8.03	8.07	8.04	8.15
2MASS J16265441 +1457502	2016-05-26	2.69	4.61	5.96	6.73	7.22	7.58	7.56	7.59	7.77	7.87	7.91	8.12	8.04	8.24	8.16	8.25
HIP 81084	2016-03-25	4.36	6.15	7.76	7.89	8.61	8.81	8.86	9.10	9.06	9.15	9.50	9.52	9.55	9.58	9.57	9.57
2MASS J16430128 -1754274	2016-04-13	3.48	5.87	6.86	7.44	7.73	7.86	8.13	8.19	8.26	8.31	8.37	8.39	8.48	8.48	8.55	8.56
2MASS J17111769 +1245408	2016-05-27	3.87	5.81	6.48	6.89	7.12	7.37	7.66	7.61	7.65	7.62	7.76	7.82	7.94	7.98	7.92	7.95
2MASS J17115853 -2530585	2016-06-09	3.45	5.12	6.68	7.33	7.32	7.69	7.79	7.84	7.89	8.02	8.19	8.02	8.20	8.10	8.14	8.19
2MASS J17150219 -3333398	2016-05-27	4.98	6.56	8.04	8.39	8.58	8.76	8.44	9.29	8.91	9.14	9.39	9.57	9.67	9.82	9.89	9.86
2MASS J17261525 -0311308	2016-05-26	4.01	5.43	6.52	7.31	7.53	7.71	7.81	7.94	8.07	7.98	8.16	8.23	8.23	8.11	8.07	8.15

Name	UT Date	0″1 (Δmag)	0″2 (Δmag)	0″3 (Δmag)	0″4 (Δmag)	0″5 (Δmag)	0″6 (Δmag)	0″7 (Δmag)	0″8 (Δmag)	0″9 (Δmag)	1″0 (Δmag)	1″25 (Δmag)	1″5 (Δmag)	1″75 (Δmag)	2″0 (Δmag)	2″25 (Δmag)	2″5 (Δmag)
2MASS J17300060-1840132	2016-07-18	4.17	5.54	6.05	6.68	6.88	7.01	7.10	7.56	7.55	7.61	7.83	7.96	7.97	7.92	7.99	8.12
2MASS J17520173-2357571	2016-07-18	4.36	5.40	6.45	6.88	7.42	7.78	7.86	8.22	8.15	7.67	8.30	8.65	8.66	8.62	8.60	8.66
2MASS J17520294+5636278	2016-03-25	2.69	4.23	5.13	5.76	6.08	6.09	6.62	6.45	6.22	6.67	6.99	7.04	7.17	7.31	7.32	7.52
2MASS J17520294+5636278	2016-04-13	4.29	6.34	7.49	8.06	8.40	8.60	8.76	8.78	9.07	9.07	9.16	9.18	9.18	9.27	9.27	9.33
2MASS J17580616-2222238	2016-07-18	3.10	4.56	5.68	6.44	6.72	6.92	7.17	7.36	7.32	7.64	7.59	7.61	7.65	7.73	7.79	7.91
2MASS J18030566-0337318	2016-07-18	3.15	4.78	6.25	6.82	7.14	7.35	7.59	7.56	7.66	7.71	7.83	7.77	7.88	7.81	7.84	7.93
2MASS J18030566-0337318	2017-06-13	3.50	5.36	6.54	6.34	7.18	7.31	7.35	7.45	7.51	7.55	7.61	7.75	7.75	7.81	7.85	7.88
2MASS J18083702-0426259	2016-05-26	4.58	5.84	8.05	8.58	9.36	9.65	9.98	10.63	10.80	10.89	11.65	11.75	11.95	12.08	12.17	12.09
2MASS J18141047-3247344	2016-04-13	3.78	5.32	6.54	7.25	7.44	7.63	7.77	8.15	8.16	8.42	8.69	8.82	8.96	9.07	9.01	9.10
2MASS J18142207-3246100	2016-07-18	3.46	5.15	6.13	6.49	7.00	7.40	7.59	7.99	8.00	8.12	8.19	8.29	8.44	8.36	8.41	8.53
2MASS J18495543-0134087	2016-07-18	0.78	−0.00	0.00	0.07	0.71	0.83	0.89	1.28	1.26	1.33	1.54	1.89	1.99	2.12	2.27	2.25
2MASS J18495543-0134087	2017-06-13	4.13	5.59	6.93	7.20	7.33	7.71	7.79	8.02	8.17	8.17	8.37	8.50	8.45	8.48	8.54	8.63
2MASS J18504448-3147472	2016-05-26	3.68	5.48	6.54	7.44	7.97	8.42	8.61	8.89	9.05	9.04	9.29	9.37	9.35	9.45	9.52	9.41
2MASS J18504448-3147472	2018-07-30	4.38	6.37	7.38	7.90	8.09	8.11	8.21	8.58	8.67	8.79	9.01	9.08	9.30	9.26	9.34	9.36
2MASS J18553176-1622495	2017-07-04	4.29	5.99	6.67	7.14	7.36	7.55	7.92	8.21	8.34	8.38	8.66	8.72	8.92	8.93	8.93	9.02
2MASS J18580415-2953045	2017-05-10	3.55	5.26	6.30	6.84	7.28	7.80	7.93	8.20	8.35	8.50	8.70	8.79	8.86	9.03	9.02	9.09
2MASS J18580415-2953045	2017-06-13	3.27	5.52	6.56	7.02	7.09	7.24	7.64	7.74	7.95	8.06	8.31	8.37	8.68	8.67	8.70	8.82
2MASS J19243494-3442392	2016-05-26	3.53	5.60	6.41	7.09	7.26	7.42	7.74	7.99	8.10	8.12	8.35	8.47	8.52	8.57	8.57	8.68
2MASS J19312434-2134226	2016-05-27	5.07	7.42	8.16	8.75	8.84	9.11	9.21	9.40	9.09	9.07	9.30	9.48	9.61	9.60	9.60	9.68
2MASS J19312434-2134226	2018-07-30	3.95	5.84	7.01	7.55	7.68	7.92	8.08	8.36	8.44	8.49	8.77	8.71	8.89	8.89	8.93	9.07
2MASS J19420065-2104051	2016-05-27	5.53	7.36	8.16	8.68	8.90	9.00	9.28	9.42	9.23	9.38	9.53	9.55	9.63	9.76	9.75	9.78
2MASS J19435432-0546363	2016-07-18	2.08	3.59	4.13	5.19	5.26	5.58	5.73	5.93	6.06	6.07	6.42	6.53	6.67	6.67	6.65	6.61
2MASS J19560438-3207376	2016-05-27	4.60	6.48	7.15	7.52	8.00	8.22	8.52	8.65	8.88	8.88	9.12	9.20	9.27	9.32	9.42	9.46
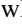
Table B1
(Continued)

Name	UT Date	0″1 (Δmag)	0″2 (Δmag)	0″3 (Δmag)	0″4 (Δmag)	0″5 (Δmag)	0″6 (Δmag)	0″7 (Δmag)	0″8 (Δmag)	0″9 (Δmag)	1″0 (Δmag)	1″25 (Δmag)	1″5 (Δmag)	1″75 (Δmag)	2″0 (Δmag)	2″25 (Δmag)	2″5 (Δmag)
2MASS J20013718-3313139	2017-05-10	3.03	4.64	5.92	6.85	7.35	7.47	7.80	7.95	8.11	8.19	8.35	8.45	8.56	8.67	8.74	8.72
2MASS J20043077-2342018	2016-07-18	3.51	4.76	5.15	5.52	6.43	7.14	7.57	8.06	8.49	8.65	9.04	9.11	9.28	9.44	9.47	9.57
2MASS J20043077-2342018	2018-07-30	4.42	6.50	7.37	7.53	7.93	8.31	8.51	8.80	8.99	8.97	9.26	9.29	9.46	9.42	9.42	9.49
2MASS J20043077-2342018	2017-06-13	3.98	6.32	7.55	7.67	7.53	8.00	8.06	8.37	8.40	8.40	8.80	8.79	8.93	8.96	9.00	9.13
V* V5663 Sgr	2017-05-11	3.74	5.68	6.93	6.96	7.59	7.74	8.05	8.25	8.45	8.50	8.80	8.83	9.00	9.02	9.02	9.06
V* V5663 Sgr	2017-06-13	3.67	5.81	6.92	6.98	7.11	7.02	7.80	7.89	8.03	8.14	8.55	8.70	8.78	8.75	8.83	8.92
2MASS J20333759-2556521	2017-05-11	3.65	5.09	6.23	6.39	6.54	6.39	6.56	6.94	7.05	7.03	7.44	7.48	7.62	7.67	7.73	7.80
2MASS J20395460+0620118	2018-07-30	4.31	6.14	8.01	8.53	8.98	9.28	9.50	9.57	9.67	9.62	9.93	9.80	9.90	9.97	9.94	9.92
2MASS J20395460+0620118	2016-06-15	5.11	7.14	8.14	8.80	9.23	9.32	9.43	9.65	9.72	9.75	9.77	9.83	9.93	9.83	9.94	9.86
AU Mic	2016-10-18	4.68	6.90	7.98	8.49	9.17	9.69	9.98	10.60	10.94	10.99	11.62	11.93	12.05	12.10	12.21	12.18
2MASS J20465795-0259320	2016-05-27	4.05	6.11	7.14	7.37	7.81	8.04	8.40	8.64	8.84	8.82	9.02	8.97	9.11	9.00	9.00	9.04
2MASS J21073678-1304581	2016-10-18	4.36	6.21	7.37	7.92	8.04	8.38	8.74	8.93	9.11	9.15	9.33	9.48	9.55	9.68	9.74	9.81
2MASS J21100535-1919573	2016-08-08	6.41	6.68	9.61	7.57	9.39	9.34	8.30	8.74	8.95	9.29	9.27	9.32	9.46	9.49	9.58	9.70
2MASS J21100535-1919573	2017-06-13	4.39	6.10	7.53	7.63	8.36	8.37	8.88	9.06	9.07	9.19	9.54	9.60	9.76	9.71	9.82	9.92
2MASS J21130526-1729126	2016-07-18	2.51	4.58	6.76	7.49	7.99	8.38	8.54	8.79	8.94	8.99	9.07	9.13	9.20	9.28	9.16	9.26
[SLS2012] PYC J21148+1254	2017-06-13	3.64	5.48	6.82	6.94	7.30	7.52	7.70	7.76	7.84	7.87	7.94	7.94	8.05	8.07	8.21	8.23
LO Peg	2016-06-15	5.58	6.33	7.76	8.96	8.99	9.66	9.95	10.25	10.26	10.52	10.71	10.80	10.71	10.77	10.72	10.77
2MASS J21334415-3453372	2017-07-04	3.02	3.79	4.85	5.60	5.65	5.41	5.79	6.19	5.63	5.63	6.26	6.17	6.29	6.54	6.46	6.40
2MASS J22021626-4210329	2018-07-30	3.43	5.90	6.94	7.56	7.70	7.84	8.03	8.17	8.30	8.35	8.72	8.71	8.79	8.91	8.92	9.07
2MASS J22021626-4210329	2017-06-13	3.45	5.58	6.43	6.51	6.37	6.28	7.18	7.38	7.36	7.47	7.77	7.78	8.05	8.09	8.13	8.21
PM J22088+1144	2017-07-04	3.05	5.05	5.70	6.19	6.16	6.30	6.33	6.31	6.30	6.35	6.60	6.93	7.11	7.20	7.21	7.35
2MASS J22174316-1546452	2017-07-04	3.41	5.06	5.81	6.03	5.93	5.95	6.28	6.44	6.62	6.62	6.90	6.98	7.13	7.21	7.26	7.24
2MASS J22274882-0113527	2016-11-22	4.18	6.07	7.29	7.82	7.92	7.98	8.51	8.57	8.54	8.51	8.69	8.56	8.75	8.86	8.85	8.93
2MASS J22274882-0113527	2016-10-18	3.84	5.82	6.84	7.24	7.31	7.48	7.49	7.46	7.26	6.99	7.43	7.45	7.48	7.71	7.79	7.96
WW PsA	2017-07-04	3.08	4.77	5.92	6.46	6.05	6.19	6.58	6.71	6.79	6.88	7.13	7.38	7.50	7.57	7.57	7.72
TX PsA	2016-11-23	3.69	5.66	6.95	7.40	7.44	7.41	8.36	8.44	8.22	7.97	8.61	8.66	8.93	8.98	9.09	9.23
TX PsA	2018-07-30	3.34	5.79	6.99	7.46	7.85	7.96	8.29	8.55	8.33	8.27	8.62	8.36	8.71	8.63	8.57	8.75
HIP 114066	2016-11-23	4.93	6.85	7.78	8.35	8.31	8.70	9.15	9.32	9.36	9.52	9.79	9.95	10.00	10.06	10.08	10.14

Table B1
(Continued)

Name	UT Date	0″1 (Δmag)	0″2 (Δmag)	0″3 (Δmag)	0″4 (Δmag)	0″5 (Δmag)	0″6 (Δmag)	0″7 (Δmag)	0″8 (Δmag)	0″9 (Δmag)	1″0 (Δmag)	1″25 (Δmag)	1″5 (Δmag)	1″75 (Δmag)	2″0 (Δmag)	2″25 (Δmag)	2″5 (Δmag)
HIP 114066	2016-09-11	3.74	5.79	7.26	7.44	7.58	7.76	8.32	8.53	8.62	8.67	9.00	9.12	9.21	9.35	9.24	9.38
2MASS J23093711-0225551	2016-11-22	4.61	6.61	7.44	7.94	8.23	8.37	8.69	8.93	8.98	8.90	9.02	8.96	9.09	9.13	9.15	9.25
2MASS J23282251+0028395	2016-10-17	3.87	6.22	7.14	7.46	7.76	7.87	8.07	8.23	8.19	8.35	8.39	8.45	8.55	8.72	8.70	8.74
2MASS J23301341-2023271	2017-07-04	5.61	5.78	6.96	7.35	7.55	7.19	7.82	8.46	8.67	8.63	9.37	9.89	10.15	10.27	10.40	10.56
2MASS J23314492-0244395	2017-07-05	3.45	5.50	6.94	7.58	7.59	8.03	8.20	8.30	8.47	8.68	8.70	8.85	8.95	8.95	8.95	9.08
2MASS J23320018-3917368	2016-11-22	3.51	4.20	5.25	5.13	5.22	4.70	5.79	5.84	5.90	5.88	6.26	6.28	6.43	6.54	6.62	6.71
2MASS J23323085-1215513	2017-07-05	5.44	5.99	7.04	7.41	7.98	8.05	8.43	8.92	9.39	9.68	10.09	10.05	10.31	10.34	10.18	10.40
2MASS J23323085-1215513	2018-07-30	5.27	6.30	7.97	8.88	9.26	9.79	9.83	10.02	10.15	10.07	10.30	10.35	10.41	10.46	10.45	10.58
2MASS J23331860+2714219	2016-07-18	3.61	6.04	7.13	7.81	8.06	8.28	8.27	8.43	8.61	8.60	8.59	8.70	8.66	8.64	8.67	8.64
2MASS J23433386-1928024	2016-11-23	3.96	6.22	7.21	7.34	7.59	7.73	7.92	7.91	7.82	7.97	8.15	8.39	8.45	8.58	8.64	8.66
2MASS J23433386-1928024	2017-09-09	3.89	5.10	6.48	7.18	7.07	7.13	7.57	7.82	8.01	8.07	8.28	8.45	8.61	8.62	8.55	8.64
2MASS J23433386-1928024	2016-09-11	−0.00	2.38	5.77	3.48	3.37	3.68	3.91	3.91	4.29	4.08	4.76	4.87	4.99	4.99	5.21	5.22
2MASS J23500639+2659519	2017-09-09	3.69	5.94	7.16	7.58	7.74	7.83	8.06	8.21	8.32	8.36	8.43	8.40	8.47	8.47	8.51	8.48
2MASS J23512227+2344207	2016-11-05	4.39	6.47	7.64	8.01	8.04	8.24	8.19	8.48	8.41	8.54	8.47	8.58	8.46	8.43	8.29	8.30
2MASS J23513366+3127229	2017-09-09	3.42	5.91	6.90	7.55	7.61	7.73	8.00	7.96	8.02	8.01	8.07	8.11	8.29	8.28	8.29	8.18
2MASS J23513366+3127229	2018-07-30	3.28	5.32	6.35	6.61	7.02	7.16	7.29	7.35	7.42	7.49	7.55	7.59	7.76	7.83	7.71	6.97
2MASS J23514340+3127045	2017-09-09	3.35	5.68	6.71	7.14	7.09	7.07	7.30	7.37	6.89	6.86	7.03	7.32	7.47	7.62	7.61	7.69
GJ 4379	2016-09-12	4.60	6.47	8.04	8.39	8.55	8.76	8.71	8.78	8.92	8.89	9.10	9.01	9.20	9.15	9.08	9.26

ORCID iDs

Aniket Sanghi ⬤ https://orcid.org/0000-0002-1838-4757
Jerry W. Xuan ⬤ https://orcid.org/0000-0002-6618-1137
Jason J. Wang ⬤ https://orcid.org/0000-0003-0774-6502
Dimitri Mawet ⬤ https://orcid.org/0000-0002-8895-4735
Brendan P. Bowler ⬤ https://orcid.org/0000-0003-2649-2288
Henry Ngo ⬤ https://orcid.org/0000-0001-5172-4859
Marta L. Bryan ⬤ https://orcid.org/0000-0002-6076-5967
Garreth Ruane ⬤ https://orcid.org/0000-0003-4769-1665
Olivier Absil ⬤ https://orcid.org/0000-0002-4006-6237
Elsa Huby ⬤ https://orcid.org/0000-0002-1342-2822

References

Absil, O., & Mawet, D. 2010, A&ARv, 18, 317
Adams Redai, J. I., Follette, K. B., Wang, J., et al. 2023, AJ, 165, 57
Aldering, G., Adam, G., Antilogus, P., et al. 2002, Proc. SPIE, 4836, 61
Allen, P. R., & Reid, I. N. 2008, AJ, 135, 2024
Ansdell, M., Gaidos, E., Mann, A. W., et al. 2015, ApJ, 798, 41
Arnold, R. A., McSwain, M. V., Pepper, J., et al. 2020, ApJS, 247, 44
Astropy Collaboration, Robitaille, T. P., Tollerud, E. J., et al. 2013, A&A, 558, A33
Astropy Collaboration, Price-Whelan, A. M., Sipőcz, B. M., et al. 2018, AJ, 156, 123
Bailey, V. P., Poyneer, L. A., Macintosh, B. A., et al. 2016, Proc. SPIE, 9909, 99090V
Baraffe, I., Chabrier, G., Barman, T. S., Allard, F., & Hauschildt, P. H. 2003, A&A, 402, 701
Barnes, J. R., Collier Cameron, A., Lister, T. A., Pointer, G. R., & Still, M. D. 2005, MNRAS, 356, 1501
Barrado y Navascués, D., & Martín, E. L. 2003, AJ, 126, 2997
Beers, T. C., Flynn, C., Rossi, S., et al. 2007, ApJS, 168, 128
Bell, C. P. M., Mamajek, E. E., & Naylor, T. 2015, MNRAS, 454, 593
Bonse, M. J., Gebhard, T. D., Dannert, F. A., et al. 2024, arXiv:2406.01809
Boss, A. P. 1997, Sci, 276, 1836
Bowler, B. P. 2016, PASP, 128, 102001
Bowler, B. P., Blunt, S. C., & Nielsen, E. L. 2020, AJ, 159, 63
Bowler, B. P., Hinkley, S., Ziegler, C., et al. 2019, ApJ, 877, 60
Bowler, B. P., Liu, M. C., Mawet, D., et al. 2017, AJ, 153, 18
Bowler, B. P., Liu, M. C., Shkolnik, E. L., & Dupuy, T. J. 2013, ApJ, 774, 55
Bowler, B. P., Liu, M. C., Shkolnik, E. L., & Tamura, M. 2015a, ApJS, 216, 7
Bowler, B. P., Liu, M. C., Shkolnik, E. L., et al. 2012, ApJ, 753, 142
Bowler, B. P., Shkolnik, E. L., Liu, M. C., et al. 2015b, ApJ, 806, 62
Bradley, L., Sipőcz, B., Robitaille, T., et al. 2019, astropy/photutils: v0.7.2, Zenodo, doi:10.5281/zenodo.3568247
Brandt, T. D., & Huang, C. X. 2015, ApJ, 807, 24
Bryan, M. L., Chiang, E., Bowler, B. P., et al. 2020, AJ, 159, 181
Carter, A. L., Hinkley, S., Kammerer, J., et al. 2023, ApJL, 951, L20
Casagrande, L., Flynn, C., & Bessell, M. 2008, MNRAS, 389, 585
Chabrier, G., Johansen, A., Janson, M., & Rafikov, R. 2014, in Protostars and Planets VI, ed. H. Beuther et al. (Tucson, AZ: Univ. Arizona Press), 619
Choquet, É., Perrin, M. D., Chen, C. H., et al. 2016, ApJL, 817, L2
Christiaens, V., Gonzalez, C. A. G., Farkas, R., et al. 2023, JOSS, 8, 4774
Cieza, L. A., Schreiber, M. R., Romero, G. A., et al. 2012, ApJ, 750, 157
Currie, T., Biller, B., Lagrange, A., et al. 2023a, in ASP Conf. Ser. 534, Protostars and Planets VII, ed. S. Inutsuka et al. (San Francisco, CA: ASP), 799
Currie, T., Brandt, G. M., Brandt, T. D., et al. 2023b, Sci, 380, 198
Currie, T., Burrows, A., Girard, J. H., et al. 2014, ApJ, 795, 133
Currie, T., Fukagawa, M., Thalmann, C., Matsumura, S., & Plavchan, P. 2012, ApJL, 755, L34
Cutri, R. M., et al. 2012, yCat, II/311
Cutri, R. M., Wright, E. L., Conrow, T., et al. 2021, yCat, II/328
Daemgen, S., Bonavita, M., Jayawardhana, R., Lafrenière, D., & Janson, M. 2015, ApJ, 799, 155
Daemgen, S., Siegler, N., Reid, I. N., & Close, L. M. 2007, ApJ, 654, 558
De Rosa, R. J., Nielsen, E. L., Wahhaj, Z., et al. 2023, A&A, 672, A94
Debes, J. H., Ren, B., & Schneider, G. 2019, JATIS, 5, 035003
Delorme, P., Lagrange, A. M., Chauvin, G., et al. 2012, A&A, 539, A72
Desidera, S., Chauvin, G., Bonavita, M., et al. 2021, A&A, 651, A70
Devor, J., Charbonneau, D., O'Donovan, F. T., Mandushev, G., & Torres, G. 2008, AJ, 135, 850
Douglas, S. T., Agüeros, M. A., Covey, K. R., et al. 2014, ApJ, 795, 161

Douglas, S. T., Curtis, J. L., Agüeros, M. A., et al. 2019, ApJ, 879, 100
Ducati, J. R. 2002, yCat, 2237
Duchêne, G., Rice, M., Hom, J., et al. 2020, AJ, 159, 251
Eggen, O. J. 1990, PASP, 102, 166
Eibe, M. T., Byrne, P. B., Jeffries, R. D., & Gunn, A. G. 1999, A&A, 341, 527
Elliott, P., Bayo, A., Melo, C. H. F., et al. 2016, A&A, 590, A13
Esplin, T. L., Luhman, K. L., & Mamajek, E. E. 2014, ApJ, 784, 126
Fernandes, R. B., Mulders, G. D., Pascucci, I., Mordasini, C., & Emsenhuber, A. 2019, ApJ, 874, 81
Foo, G., Palacios, D. M., & Swartzlander, G. A. J. 2005, OptL, 30, 3308
Fouque, P., Moutou, C., Malo, L., et al. 2018, MNRAS, 475, 1960
Franson, K., Bowler, B. P., Bonavita, M., et al. 2023a, AJ, 165, 39
Franson, K., Bowler, B. P., Brandt, T. D., et al. 2022, AJ, 163, 50
Franson, K., Bowler, B. P., Zhou, Y., et al. 2023b, ApJL, 950, L19
Fuhrmeister, B., & Schmitt, J. H. M. M. 2003, A&A, 403, 247
Fulton, B. J., Rosenthal, L. J., Hirsch, L. A., et al. 2021, ApJS, 255, 14
Gagné, J., Faherty, J. K., Cruz, K. L., et al. 2015, ApJS, 219, 33
Gagné, J., Mamajek, E. E., Malo, L., et al. 2018, ApJ, 856, 23
Gaia Collaboration 2020, yCat, I/350
Gaidos, E., Mann, A. W., Lepine, S., et al. 2014, MNRAS, 443, 2561
Gerard, B. L., & Marois, C. 2016, Proc. SPIE, 9909, 990958
Gomez Gonzalez, C. A., Wertz, O., Absil, O., et al. 2017, AJ, 154, 7
Gray, R. O., Corbally, C. J., Garrison, R. F., McFadden, M. T., & Robinson, P. E. 2003, AJ, 126, 2048
Greenbaum, A. Z., Llop-Sayson, J., Lew, B. W. P., et al. 2023, ApJ, 945, 126
Guyon, O., Pluzhnik, E. A., Kuchner, M. J., Collins, B., & Ridgway, S. T. 2006, ApJS, 167, 81
Harris, C. R., Millman, K. J., van der Walt, S. J., et al. 2020, Natur, 585, 357
Helled, R., Bodenheimer, P., Podolak, M., et al. 2014, in Protostars and Planets VI, ed. H. Beuther et al. (Tucson, AZ: Univ. Arizona Press), 643
Helling, C., Woitke, P., Rimmer, P. B., et al. 2014, Life, 4, 142
Hinkley, S., Lacour, S., Marleau, G. D., et al. 2023, A&A, 671, L5
Howard, W. S., Corbett, H., Law, N. M., et al. 2019, ApJ, 881, 9
Huby, E., Baudoz, P., Mawet, D., & Absil, O. 2015, A&A, 584, A74
Huby, E., Bottom, M., Femenia, B., et al. 2017, A&A, 600, A46
Hunter, J. D. 2007, CSE, 9, 90
Jeffries, R. D., Byrne, P. B., Doyle, J. G., et al. 1994, MNRAS, 270, 153
Karmakar, S., Pandey, J. C., Savanov, I. S., et al. 2016, MNRAS, 459, 3112
Kiman, R., Faherty, J. K., Cruz, K. L., et al. 2021, AJ, 161, 277
Koen, C., Kilkenny, D., van Wyk, F., & Marang, F. 2010, MNRAS, 403, 1949
Kratter, K., & Lodato, G. 2016, ARA&A, 54, 271
Kraus, A. L., Herczeg, G. J., Rizzuto, A. C., et al. 2017, ApJ, 838, 150
Kraus, A. L., Ireland, M. J., Martinache, F., & Hillenbrand, L. A. 2011, ApJ, 731, 8
Kraus, A. L., Shkolnik, E. L., Allers, K. N., & Liu, M. C. 2014, AJ, 147, 146
Kundurthy, P., Meyer, M. R., Robberto, M., Beckwith, S. V. W., & Herbst, T. 2006, AJ, 132, 2469
Kuzuhara, M., Currie, T., Takarada, T., et al. 2022, ApJL, 934, L18
Lafreniere, D., Marois, C., Doyon, R., & Barman, T. 2009, ApJ, 694, L148
Lafrenière, D., Doyon, R., Marois, C., et al. 2007a, ApJ, 670, 1367
Lafrenière, D., Marois, C., Doyon, R., Nadeau, D., & Artigau, É. 2007b, ApJ, 660, 770
Lagrange, A.-M., Bonnefoy, M., Chauvin, G., et al. 2010, Sci, 329, 57
Lagrange, A. M., Gratadour, D., Chauvin, G., et al. 2009, A&A, 493, L21
Landolt, A. U. 2009, AJ, 137, 4186
Lannier, J., Delorme, P., Lagrange, A. M., et al. 2016, A&A, 596, A83
Lantz, B., Aldering, G., Antilogus, P., et al. 2004, Proc. SPIE, 5249, 146
Lépine, S., & Shara, M. M. 2005, AJ, 129, 1483
Ligi, R., Vigan, A., Gratton, R., et al. 2018, MNRAS, 473, 1774
Liu, M. C. 2004, Sci, 305, 1442
Liu, M. C., Wahhaj, Z., Biller, B. A., et al. 2010, Proc. SPIE, 7736, 77361K
Luhman, K. L., Whitney, B. A., Meade, M. R., et al. 2006, ApJ, 647, 1180
Macintosh, B., Graham, J. R., Barman, T., et al. 2015, Sci, 350, 64
Macintosh, B., Chilcote, J. K., Bailey, V. P., et al. 2018, Proc. SPIE, 10703, 107030K
Makarov, V. V. 2007, ApJ, 658, 480
Malo, L., Artigau, É., Doyon, R., et al. 2014, ApJ, 788, 81
Malo, L., Doyon, R., Lafrenière, D., et al. 2013, ApJ, 762, 88
Marois, C., Lafrenière, D., Doyon, R., Macintosh, B., & Nadeau, D. 2006, ApJ, 641, 556
Marois, C., Macintosh, B., & Véran, J.-P. 2010, Proc. SPIE, 7736, 77361J
Mawet, D., Milli, J., Wahhaj, Z., et al. 2014, ApJ, 792, 97
Mawet, D., Pueyo, L., Lawson, P., et al. 2012, Proc. SPIE, 8442, 844204
Mawet, D., Riaud, P., Absil, O., & Surdej, J. 2005, ApJ, 633, 1191
Mendigutía, I., Mora, A., Montesinos, B., et al. 2012, A&A, 543, A59
Mesa, D., Gratton, R., Kervella, P., et al. 2023, A&A, 672, A93

Meshkat, T., Kenworthy, M. A., Quanz, S. P., & Amara, A. 2014, ApJ, 780, 17
Monet, D. G., Levine, S. E., Canzian, B., et al. 2003, AJ, 125, 984
Morzinski, K. M., Macintosh, B. A., Close, L. M., et al. 2012, Proc. SPIE, 8447, 84470O
Naud, M.-E., Artigau, É., Doyon, R., et al. 2017, AJ, 154, 129
Nelder, J. A., & Mead, R. 1965, Comput. J., 7, 308
Nielsen, E. L., De Rosa, R. J., Macintosh, B., et al. 2019, AJ, 158, 13
Norton, A. J., Wheatley, P. J., West, R. G., et al. 2007, A&A, 467, 785
Nowak, M., Lacour, S., Lagrange, A. M., et al. 2020, A&A, 642, L2
Ochsenbein, F., Bauer, P., & Marcout, J. 2000, A&AS, 143, 23
Oppenheimer, B. R., & Hinkley, S. 2009, ARA&A, 47, 253
Pearce, L. A., Males, J. R., Weinberger, A. J., et al. 2022, MNRAS, 515, 4487
Piluso, N., Lanza, A. F., Pagano, I., Lanzafame, A. C., & Donati, J.-F. 2008, MNRAS, 387, 237
Preibisch, T., & Feigelson, E. D. 2005, ApJS, 160, 390
Pueyo, L. 2016, ApJ, 824, 117
Reid, I. N., Cruz, K. L., & Allen, P. R. 2007, AJ, 133, 2825
Reid, I. N., Hawley, S. L., & Gizis, J. E. 1995, AJ, 110, 1838
Riaz, B., Gizis, J. E., & Harvin, J. 2006, AJ, 132, 866
Riedel, A. R., Finch, C. T., Henry, T. J., et al. 2014, AJ, 147, 85
Rodigas, T. J., Weinberger, A., Mamajek, E. E., et al. 2015, ApJ, 811, 157
Ruane, G., Mawet, D., Kastner, J., et al. 2017, AJ, 154, 73
Ruane, G., Ngo, H., Mawet, D., et al. 2019, AJ, 157, 118
Sanghi, A., Zhou, Y., & Bowler, B. P. 2022, AJ, 163, 119
Schlieder, J. E., Lépine, S., & Simon, M. 2012, AJ, 143, 80
Schneider, G., Grady, C. A., Hines, D. C., et al. 2014, AJ, 148, 59
Serabyn, E., Huby, E., Matthews, K., et al. 2017, AJ, 153, 43
Service, M., Lu, J. R., Campbell, R., et al. 2016, PASP, 128, 095004
Shkolnik, E., Liu, M. C., & Reid, I. N. 2009, ApJ, 699, 649
Shkolnik, E. L., Anglada-Escudé, G., Liu, M. C., et al. 2012, ApJ, 758, 56
Skemer, A. J., Hinz, P., Esposito, S., et al. 2014, Proc. SPIE, 9148, 91480L

Skumanich, A. 1972, ApJ, 171, 565
Smith, B. A., & Terrile, R. J. 1984, Sci, 226, 1421
Soummer, R., Perrin, M. D., Pueyo, L., et al. 2014, ApJL, 786, L23
Soummer, R., Pueyo, L., & Larkin, J. 2012, ApJL, 755, L28
Stone, J. M., Skemer, A. J., Hinz, P. M., et al. 2018, AJ, 156, 286
Tamura, M. 2009, in AIP Conf. Ser. 1158, Exoplanets and Disks: Their Formation and Diversity, ed. T. Usuda, M. Tamura, & M. Ishii (AIP) (Melville, NY: AIP), 11
Tamura, M. 2016, PJAB, 92, 45
Tannirkulam, A., Monnier, J. D., Harries, T. J., et al. 2008, ApJ, 689, 513
Theissen, C. A., & West, A. A. 2014, ApJ, 794, 146
Torres, C. A. O., Quast, G. R., Melo, C. H. F., & Sterzik, M. F. 2008, in Handbook of Star Forming Regions (Vol. II) ed. B. Reipurth, Vol. 5 (San Francisco, CA: ASP), 757
van der Walt, S., Schönberger, J. L., Nunez-Iglesias, J., et al. 2014, arXiv:1407.6245
Vigan, A., Fontanive, C., Meyer, M., et al. 2021, A&A, 651, A72
Vigan, A., Patience, J., Marois, C., et al. 2012, A&A, 544, A9
Wahhaj, Z., Milli, J., Romero, C., et al. 2021, A&A, 648, A26
Walker, S., Millar-Blanchaer, M. A., Ren, B., Kalas, P., & Carpenter, J. 2021, MNRAS, 504, 3074
West, A. A., Hawley, S. L., Bochanski, J. J., et al. 2008, AJ, 135, 785
West, A. A., Morgan, D. P., Bochanski, J. J., et al. 2011, AJ, 141, 97
Wilson, O. C. 1963, ApJ, 138, 832
Xie, C., Choquet, E., Vigan, A., et al. 2022, A&A, 666, A32
Xuan, W. J., Mawet, D., Ngo, H., et al. 2018, AJ, 156, 156
Zacharias, N., Finch, C., Girard, T., et al. 2009, yCat, I/315
Zacharias, N., Finch, C. T., Girard, T. M., et al. 2012, yCat, I/322A
Zacharias, N., Urban, S. E., Zacharias, M. I., et al. 2003, yCat, I/289
Zúñiga-Fernández, S., Bayo, A., Elliott, P., et al. 2021, A&A, 645, A30
Zuckerman, B., & Song, I. 2004, ARA&A, 42, 685